

## Harmonized-Multinational qEEG norms (HarMNqEEG)

Min Li<sup>a</sup>, Ying Wang<sup>a</sup>, Carlos Lopez-Naranjo<sup>a</sup>, Shiang Hu<sup>a,ae</sup>, Ronaldo César García Reyes<sup>b</sup>, Deirel Paz-Linares<sup>a,b</sup>, Ariosky Areces-Gonzalez<sup>a,j</sup>, Aini Ismafairus Abd Hamid<sup>d,e,f</sup>, Alan C. Evans<sup>c</sup>, Alexander N. Savostyanov<sup>g,h,i</sup>, Ana Calzada-Reyes<sup>b</sup>, Arno Villringer<sup>k,l,m</sup>, Carlos A. Tobon-Quintero<sup>n,o</sup>, Daysi Garcia-Agustin<sup>b,p</sup>, Dezhong Yao<sup>a,q,r</sup>, Li Dong<sup>a,q,s</sup>, Eduardo Aubert-Vazquez<sup>b</sup>, Faruque Reza<sup>d,e,f</sup>, Fuleah Abdul Razzaq<sup>a</sup>, Hazim Omar<sup>d,e,f</sup>, Jafri Malin Abdullah<sup>d,e,f</sup>, Janina R. Galler<sup>t</sup>, John F. Ochoa-Gomez<sup>n,u</sup>, Leslie S. Prichep<sup>v,w</sup>, Lidice Galan-Garcia<sup>b</sup>, Lilia Morales-Chacon<sup>x</sup>, Mitchell J. Valdes-Sosa<sup>b</sup>, Marius Tröndle<sup>y,z,aa</sup>, Mohd Faizal Mohd Zulkifly<sup>d,e,f</sup>, Muhammad Riddha Bin Abdul Rahman<sup>d,e,ab</sup>, Natalya S. Milakhina<sup>h,i</sup>, Nicolas Langer<sup>y,z,aa</sup>, Pavel Rudych<sup>h,ac,ad</sup>, Thomas Koenig<sup>af</sup>, Trinidad A. Virues-Alba<sup>b</sup>, Xu Lei<sup>ag</sup>, Maria L. Bringas-Vega<sup>a,b,\*</sup>, Jorge F. Bosch-Bayard<sup>a,b,c,\*</sup>, Pedro Antonio Valdes-Sosa<sup>a,b,\*</sup>

<sup>a</sup> The Clinical Hospital of Chengdu Brain Science Institute, MOE Key Lab for Neuroinformatics, School of Life Science and Technology, University of Electronic Science and Technology of China, Chengdu, China

<sup>b</sup> Cuban Center for Neuroscience, La Habana, Cuba

<sup>c</sup> McGill Centre for Integrative Neuroscience, Ludmer Centre for Neuroinformatics and Mental Health, Montreal Neurological Institute, Canada

<sup>d</sup> Department of Neurosciences, School of Medical Sciences, Universiti Sains Malaysia, Universiti Sains Malaysia Health Campus, Kota Bharu, Kelantan 16150, Malaysia

<sup>e</sup> Brain and Behaviour Cluster, School of Medical Sciences, Universiti Sains Malaysia, Health Campus, Kota Bharu, Kelantan 16150, Malaysia

<sup>f</sup> Hospital Universiti Sains Malaysia, Universiti Sains Malaysia, Health Campus, Kota Bharu, Kelantan 16150, Malaysia

<sup>g</sup> Humanitarian Institute, Novosibirsk State University, Novosibirsk 630090, Russia

<sup>h</sup> Laboratory of Psychophysiology of Individual Differences, Federal State Budgetary Scientific Institution Scientific Research Institute of Neurosciences and Medicine, Novosibirsk 630117, Russia

<sup>i</sup> Laboratory of Psychological Genetics at the Institute of Cytology and Genetics Siberian Branch of the Russian Academy of Sciences, Novosibirsk 630090, Russia

<sup>j</sup> University of Pinar del Río "Hermanos Saiz Montes de Oca", Pinar del Río, Cuba

<sup>k</sup> Department of Neurology, Max Planck Institute for Human Cognitive and Brain Sciences, Leipzig, Germany

<sup>l</sup> Department of Cognitive Neurology, University Hospital Leipzig, Leipzig, Germany

<sup>m</sup> Center for Stroke Research, Charité-Universitätsmedizin Berlin, Berlin, Germany

<sup>n</sup> Grupo Neuropsicología y Conducta - GRUNECO, Faculty of Medicine, Universidad de Antioquia, Colombia

<sup>o</sup> Research Department, Institución Prestadora de Servicios de Salud IPS Universitaria, Colombia

<sup>p</sup> The Cuban center aging longevity and health, Havana Cuba

<sup>q</sup> Research Unit of Neuroinformatics, Chinese Academy of Medical Sciences, Chengdu 2019RU035, China

<sup>r</sup> School of Electrical Engineering, Zhengzhou University, Zhengzhou 450001, China

<sup>s</sup> Sichuan Institute for Brain Science and Brain-Inspired Intelligence, Chengdu 611731, China

<sup>t</sup> Division of Pediatric Gastroenterology and Nutrition, Massachusetts General Hospital for Children, Boston, MA, United States Massachusetts General Hospital for Children, Boston, MA, United States

<sup>u</sup> Grupo de Neurociencias de Antioquia, Universidad de Antioquia, School of Medicine. Medellín, Colombia

<sup>v</sup> Research & Development, BrainScope Company, Inc. Bethesda, MD, United States

<sup>w</sup> Department of Psychiatry (Ret.), Brain Research Laboratories, NYU School of Medicine, New York, NY, United States

<sup>x</sup> Department of Clinical Neurophysiology, International Center for Neurological Restoration, Playa, Havana 11300, Cuba

<sup>y</sup> Department of Methods of Plasticity Research, Institute of Psychology, University of Zurich, Zurich, Switzerland

<sup>z</sup> University Research Priority Program "Dynamic of Healthy Aging", University of Zurich, Zurich, Switzerland

<sup>aa</sup> Neuroscience Center Zurich (ZNZ), Zurich, Switzerland

<sup>ab</sup> School of Medical Imaging, Faculty of Health Sciences, Universiti Sultan Zainal Abidin, Kuala Nerus 21300, Malaysia

<sup>ac</sup> Department of Information Technologies Novosibirsk State University, Novosibirsk 630090, Russia

\* Corresponding authors at: The Clinical Hospital of Chengdu Brain Science Institute, MOE Key Lab for Neuroinformatics, School of Life Science and Technology, University of Electronic Science and Technology of China, Chengdu, China.

E-mail addresses: [maria.bringas@neuroinformatics-collaboratory.org](mailto:maria.bringas@neuroinformatics-collaboratory.org) (M.L. Bringas-Vega), [oldgandalf@gmail.com](mailto:oldgandalf@gmail.com) (J.F. Bosch-Bayard), [pedro.valdes@neuroinformatics-collaboratory.org](mailto:pedro.valdes@neuroinformatics-collaboratory.org) (P.A. Valdes-Sosa).

<https://doi.org/10.1016/j.neuroimage.2022.119190>.

Received 12 January 2022; Received in revised form 23 March 2022; Accepted 5 April 2022

Available online 7 April 2022.

1053-8119/© 2022 The Authors. Published by Elsevier Inc. This is an open access article under the CC BY-NC-ND license

(<http://creativecommons.org/licenses/by-nc-nd/4.0/>)

<sup>ad</sup> Federal Research Center for Information and Computational Technologies, Biomedical Data Processing Lab, Novosibirsk 630090, Russia

<sup>ae</sup> Anhui Provincial Key Laboratory of Multimodal Cognitive Computation, Key Laboratory of Intelligent Computing & Signal Processing of Ministry of Education, School of Computer Science and Technology, Anhui University, Hefei 230601, China

<sup>af</sup> University Hospital of Psychiatry and Psychotherapy, University of Bern, Bern, Switzerland

<sup>ag</sup> Sleep and Neuroimaging Center, Faculty of Psychology, Southwest University, Chongqing 400715, China

## ARTICLE INFO

### Keywords:

Quantitative EEG  
EEG cross-spectrum  
Riemannian geometry  
Batch effects  
Z-score  
Harmonization  
Malnutrition  
Covid induced brain dysfunction  
Developmental Brain Chart

## ABSTRACT

This paper extends frequency domain quantitative electroencephalography (qEEG) methods pursuing higher sensitivity to detect Brain Developmental Disorders. Prior qEEG work lacked integration of cross-spectral information omitting important functional connectivity descriptors. Lack of geographical diversity precluded accounting for site-specific variance, increasing qEEG nuisance variance. We ameliorate these weaknesses. (i) Create lifespan Riemannian multinational qEEG norms for cross-spectral tensors. These norms result from the HarMNqEEG project fostered by the Global Brain Consortium. We calculate the norms with data from 9 countries, 12 devices, and 14 studies, including 1564 subjects. Instead of raw data, only anonymized metadata and EEG cross-spectral tensors were shared. After visual and automatic quality control, developmental equations for the mean and standard deviation of qEEG traditional and Riemannian DPs were calculated using additive mixed-effects models. We demonstrate qEEG “batch effects” and provide methods to calculate harmonized z-scores. (ii) We also show that harmonized Riemannian norms produce z-scores with increased diagnostic accuracy predicting brain dysfunction produced by malnutrition in the first year of life and detecting COVID induced brain dysfunction. (iii) We offer open code and data to calculate different individual z-scores from the HarMNqEEG dataset. These results contribute to developing bias-free, low-cost neuroimaging technologies applicable in various health settings.

## 1. Introduction

Characterizing the age-dependent developmental trajectories of the brains of healthy and diseased individuals is essential for precision medicine. [Verdi et al. \(2021\)](#) recently emphasized that we must move beyond the “average patient” when using neuroimaging. Instead, we must understand individual differences in brain aging processes to allow early detection of functional deterioration and neurodegenerative disease. Quantifying these individual developmental trajectories hinges on choosing the proper “Descriptive Parameters” (DPs) that summarize brain anatomy or physiology features and distinguishing their normal or abnormal evolution during the lifespan. These DPs depend strongly on age ([Matoušek and Petersén, 1973](#)).

Central to the definition of healthy developmental brain trajectories is the creation of age-dependent developmental “norms” (“charts” or “atlases”) comprising both measures of central population tendency as well as dispersion. The norms enable quantifying the age-adjusted statistical distance of a subject’s DP from the healthy population. Examples of such distances are the z-score or Mahalanobis distance. Armed with these age-dependent statistical distances, we can quantify Brain Developmental Deviation (BDD) and even use them to cluster and stage disease progressions ([Harmony, 1984](#)).

Large multinational projects to develop norms are now underway. These projects aim to increase genotypic and phenotypic diversity and, significantly, achieve sample sizes to provide adequate statistical power ([Bethlehem et al., 2022](#)). These endeavors have a fundamental limitation due to the costly nature and sparse geographical distribution of the technologies used to probe the brain. Large parts of the world population, even in high-income countries, are difficult or impossible to sample. Thus, issues of fairness and racial bias cannot be ignored.

In contrast with other neurotechnologies, electroencephalography (EEG) is affordable, portable, and deployable in all health system levels—whatever the economic setting. Thus EEG is a potential tool for detecting BDD in a Global Health context ([Valdés-Sosa et al., 2021](#)). Quantitative EEG (qEEG) facilitates this use by using EEG-based DPs to compare individuals with qEEG norms. The most common embodiment of qEEG uses the EEG log-power spectrum as DPs. The seminal work of [Matoušek and Petersén \(1973\)](#) pioneered this work 50 years ago, with the visionary introduction of the “age-dependent EEG quotients” to measure brain age—antedating by 4 decades current interest in this topic! This line of

work [John et al. \(1977\)](#), [Harmony et al. \(1988\)](#), [Bosch-Bayard et al., \(2001\)](#), [Bosch-Bayard et al. \(2020\)](#), [Hernandez-Gonzalez et al. \(2011\)](#) subsequently systematized this initiative. Consequently, developmental norms were constructed in several countries ([Gordon et al., 2005](#); [Lorensen and Dickson, 2003](#); [Thatcher et al., 2003](#)). Other projects recently vigorously launched are being repurposed for normative work ([Pavlov et al., 2021](#)).

An instance of norm construction and evaluation of BDD in a lower or middle-income country (LMIC) has been the Cuban Human Brain Mapping Project (CHBMP). Its first wave provided norms (means and standard deviations (SDs)) for the narrow band (NB) log-spectral DP based on 211 subjects from age 5 to 97. Despite being based on a single country database, CHBMP norms describe BDD consistently in other countries ([Bosch-Bayard et al., 2001](#); [Bringas Vega et al., 2019](#); [Taboada-Crispi et al., 2018](#)). Nevertheless, the small sample sizes make country comparisons relatively underpowered compared to neuroimaging efforts such as ENIGMA ([Thompson et al., 2014](#)).

The lack of global inclusiveness and small sample sizes in qEEG norms is a situation that this paper attempts to ameliorate by constructing a multinational norm based on 1564 EEGs from 9 countries and 14 EEG devices. We used the novel collaboration strategy described in [Gazula et al., \(2020\)](#) to facilitate data-sharing. Each site did not share raw data but rather processed it with standardized software. The only information shared for collaboration was anonymized data and the EEG cross-spectrum of each subject.

The diversity of countries and sites brought the problem of harmonization to the forefront. Harmonization is the elimination of “batch effects”. A batch effect is a nuisance variance due to cross-site equipment differences, changes over time of parameters of experiments that purport to measure the same underlying biological mechanisms, and different preprocessing of raw data. Genomics was the first to identify and minimize batch effects with statistical techniques. One such well-known technique is COMBAT, described in ([Johnson et al., 2007](#)). Subsequently, MRI multisite studies identified a similar problem where batch effects may be due to different acquisition systems, or variations in protocols. Recent efforts to address batch effects have gained traction in neuroimaging ([Fortin et al., 2018](#); [Pomponio et al., 2020](#); [Rutherford et al., 2021](#)).

A multinational EEG norm faces an even greater need for harmonization than MRI, because of the variability of recording systems from different vendors compounded by the lack of standards. Different ampli-

fier transfer functions, electrode placement systems, preprocessing protocols beg the question of EEG batch effects. Despite the apparent need for harmonization, to the best of our knowledge, there are no statistical studies of batch effects in qEEG. Therefore, we propose new statistical techniques adapted to the nature of EEG spectra for this purpose and try to identify what variables effectively define qEEG batches, testing their effect on the resulting harmonized norms and the final practical impact on measuring BDD.

We shall also remedy a current difficulty with qEEG norms. As mentioned before, these are predominantly either for broad band (BB) sensor space log-spectra DPs (Ahn et al., 1980; John et al., 1988) or their narrow band version (Szava et al., 1994; Valdés et al., 1992). This preference for log-spectra ignores that all second-order (linear) properties of quasi-stationary EEGs are encoded in the full cross-spectrum, a tensor or multi-dimensional array, Hermitian frequency-dependent matrices. The diagonal of each matrix contains the spectra for that frequency. Using only that information for qEEG ignores the off-diagonal elements, which are the cross-spectra.

To explain the intrinsic geometric relation of spectra and cross-spectra, we remind the reader that this type of data belongs to a Riemannian manifold. The related theory provides the unified framework to deal with the cross-spectrum in a principled way. Proper distances between samples are not Euclidean as in usual multivariate statistics cross-spectrum, but related concepts appropriate for Riemannian manifold (Pennec, 1999; Bhatia, 2007; Congedo et al., 2017; Sabbagh et al., 2020).

Cross-spectra are positive-definite Hermitian (HPD) matrices that lie in a nonlinear manifold, a positive-definite cone (Bhatia, 2007). Previous efforts of the PAVS lab to construct qEEG norms used the logarithm as a transformation towards Gaussianity and then followed up with ordinary univariate statistics cross-spectrum to construct norms (Bosch-Bayard et al., 2001; Bringas Vega et al., 2019; Szava et al., 1994; Taboada-Crispi et al., 2018). In the Riemannian framework, the matrix logarithm transforms the whole cross-spectral matrix towards multivariate Gaussianity (Riemannian vectorization (Pennec et al., 2006; Barachant et al., 2012; Sabbagh et al., 2020)). The approximate multivariate gaussian distribution of log matrix covariance matrices has a long history (Leonard and Hsu, 1992) but has not yet been employed in qEEG.

Riemannian geometry has become popular in the Brain-Computer Interface (BCI) literature, with significant advantages for classification precision (Barachant et al., 2013; Congedo et al., 2017; Yger et al., 2017). Sabbagh et al., (2020) recently showed that Riemannian methods improve brain age estimation with MEG. However, to our knowledge, the construction of Riemannian geometry-based developmental norms for EEG or MEG has not been attempted. We remedy this situation in this paper, constructing harmonized norms for the Riemannian vectorized cross-spectra and investigating the existence of batch effects for this type of multinational data. We also gauge the practical effect of these technical refinements on discriminant equations between out-of-sample controls and pathological subjects.

We alert the reader that our previous norms comprised scalp and source space log spectra (Bosch-Bayard et al., 2001). The excessive computational complexity of a Riemannian source cross-spectral analysis is out of the present paper's scope we postpone this development to future work.

This paper is organized as follows: the methods section contains (1) the theoretical basis of traditional and Riemannian qEEG DPs; (2) Gathering data and preprocessing for the multinational qEEG norm project; (3) Construction of the harmonized norms. In the section of results, we present (1) the quality control of the project; (2) the effect of centering on the cross-spectrum. (3) the detection of the batch effect; (4) a presentation of harmonized norms; and finally, we describe the validation of the norms for detecting BDD.

Table 1 collects the basic mathematical symbols used in this paper. The notation for several indices is summarized in Table A1

## 2. Methods

### 2.1. Traditional and Riemannian DPs based on EEG cross-spectrum

Quantitative electroencephalography (qEEG) studies DPs obtained from the electroencephalogram (EEG). These DPs encode physiologically relevant information. Here we explain the frequency domain DPs defined with the EEG cross-spectrum. Nonlinear frequency-domain (Billings and Tsang, 1989a, 1989b), time-domain (Koenig et al., 2002), or time/frequency domain (Makeig et al., 2004) DPs are also essential. In later stages of the multinational qEEG normative project, we will include these types of DPs. Table 2 summarizes EEG frequency domain DPs, which we now describe formally.

With (discrete) Fourier transform, the EEG signal  $v_{i,e,c}(t)$  (for the subject  $i$ ,  $i = 1, \dots, Ni$ , at the channel  $c$ ,  $c = 1, \dots, Nc$  and epoch  $e$ ,  $e = 1, \dots, Ne$ ) can be transformed to the frequency domain,  $v_{i,e,c}(\omega)$  (frequency  $\omega = \Delta\omega, \dots, N\omega\Delta\omega$  where  $\Delta\omega$  is the frequency resolution) which is the complex-value coefficients. The covariance matrix across all epochs  $v_{i,e,c}(\omega)$  is the cross-spectral matrix  $S_i(\omega)$  at frequency  $\omega$ .  $S_i(\omega)$  is Hermitian with elements  $s_{i,c,c'}(\omega)$ . Note that the set of all  $S_i(\omega)$  for all frequencies  $\omega = \Delta\omega, \dots, N\omega\Delta\omega$  for a given subject  $i$  is a 3-mode multi-dimensional array with dimensions  $Nc \times Nc \times N\omega$ . We remind the reader that this multi-dimensional array is also known as a **tensor**, which we denote by  $\mathcal{S}_i$  (Fig. 1-a). This concept generalizes that of a matrix. An intuitive way to think of the cross-spectral tensor  $\mathcal{S}_i$  is to consider it a "slide box" in which each "slide" is a cross-spectral matrix (Fig. 1-a). We defer a more formal discussion about cross-spectra as tensors to Appendix A for the interested reader. The set  $s_{i,c,c'}(\cdot)$  for all frequencies is known as a tube (Fig. 1-b).

For example, in this paper, the channel number  $c = 9$  corresponds to the recording at the left occipital channel in the 10–20 system O1.

#### 2.1.1. Traditional qEEG DPs

The most traditional DPs are the log-spectra which are obtained by applying the logarithm to the diagonal elements of cross-spectral matrices  $S_i(\omega) \in \mathbb{P}_{Nc}$  and stacking them as a vector:

$$\begin{aligned} \lambda(\omega) &= [\lambda_{i,c,c}(\omega)], \\ \lambda_{i,c,c}(\omega) &= \log(s_{i,c,c}(\omega)), \\ c &= 1, \dots, Nc \end{aligned}$$

The complete set of log spectral DPs is then  $\mathbf{y}_i^\lambda \in \mathbb{R}^{NcN\omega}$  (Fig. 1-c), where

$$\mathbf{y}_i^\lambda = [\lambda_i(\Delta\omega)^T, \dots, \lambda_i(N\omega\Delta\omega)^T]^T \quad (1)$$

This vector is unconstrained, and therefore the assumption that the  $\mathbf{y}_i^\lambda$  is sampled from a multivariate Gaussian distribution is reasonable, providing a natural link to quantify BDD using standard univariate and multivariate statistical distances.

These are the "traditional DPs" with which the PAVS lab developed qEEG norms calling the narrowband developmental equations "Developmental surfaces" (Szava et al., 1994) since they are bivariate functions of frequency and age. Developmental Surfaces describe EEG scalp channels and sources (Bosch-Bayard et al., 2001). These norms are now extensively used, with open-source data and code (Bosch-Bayard et al., 2020; Valdes-Sosa et al., 2021).

However, the log spectra DPs  $\mathbf{y}_i^\lambda$  are measures limited to separate channels. The relations between channels must be assessed to study the vital aspect of functional connectivity. To do this, we must consider the off-diagonal part of cross-spectral matrices<sup>1</sup>. A popular measure is

<sup>1</sup> For some calculations, using the complex value of an off-diagonal element  $s_{i,c,c'}(\omega)$  is inconvenient, and instead, we decompose these quantities into their real and imaginary parts (or absolute values and phases). We use the obvious notation, for example,  $\text{Real}(s_{i,c,c'}(\omega))$ ,  $\text{Imag}(s_{i,c,c'}(\omega))$  in the case of the cross-spectrum.

**Table 1**  
Basic mathematical symbols.

$a \in \mathbb{C}$	Scalar (lower-case font)
$\mathbf{a} \in \mathbb{C}^d$	Vector of size $d$ (bold lower-case font), with $\mathbf{a} = [a_1, \dots, a_d]^T$
$\mathbf{A} \in \mathbb{C}^{d1 \times d2}$	Matrix with size $d1 \times d2$ (bold-uppercase font) $\mathbf{A} = [a_{i,j}   i = 1, \dots, d1, j = 1, \dots, d2]$
$\mathcal{A} \in (\mathbb{C})^{d1 \times d2 \times \dots \times dn}$	Tensor of size $d1 \times d2 \times \dots \times dn$ (bold gothic font) $\mathcal{A} = [a_{i_1, i_2, \dots, i_n}   i_1 = 1, \dots, d1, \dots, i_n = 1, \dots, dn]$
$\mathcal{A} \in (\mathbb{C})^{d1 \times d2 \times d3}$ (3-d tensor)	Slices: frontal $\mathcal{A}_{:, :, k}$ ; lateral $\mathcal{A}_{:, j, :}$ ; horizontal $\mathcal{A}_{i, :, :}$ ; Fibers: column $\mathcal{A}_{:, j, k}$ ; row $\mathcal{A}_{i, :, k}$ ; tube $\mathcal{A}_{i, j, :}$ . The colon “:” denotes all elements in that dimension
$\mathbf{1}_n \in \mathbb{R}^{n \times 1}$	The vector with size $n \times 1$ whose elements are equal to 1
$\mathbf{I}_n \in \mathbb{R}^{n \times n}$	$n \times n$ Identity matrix
$\ \mathbf{a}\ $	Euclidean norm of a vector, $\ \mathbf{a}\  \triangleq \sqrt{\sum  a_i ^2}$
$\ \mathbf{A}\ _F$	Frobenius norm of a matrix $\ \mathbf{A}\ _F \triangleq \sqrt{\text{Tr}(\mathbf{A}\mathbf{A}^H)} = \sqrt{\sum  a_{i,j} ^2}$ . $[\cdot]^H$ is the conjugate transpose of a complex number vector or matrix.
Tr	Trace of a matrix. $\text{Tr}(\mathbf{A}) = \sum_{i=1}^d a_{i,i} + \dots + a_{i,i} + \dots + a_{d,d}$
vech	Half matrix vectorization, $\mathbb{H}_n \rightarrow \mathbb{C}^m$ , $m = n(n+1)/2$ . Stacks the matrix's lower triangle part, including the diagonal and column-wise into a vector
vech <sup>-1</sup>	The inverse operator of vech, $\mathbb{C}^m \rightarrow \mathbb{H}_n$ . Reassembles the vector to a matrix that the vector is lower-part including the diagonal of the matrix with column-wise
$\odot$	Hadamard or elementwise matrix product
$A \cup B$	Union of the sets $A$ and $B$
$U \setminus A$	Set difference of $U$ and $A$ , the set of all elements of $U$ are not the member of $A$
$\mathcal{H}$	The $n$ -dimensional Hilbert space $\mathbb{C}^n$ which inner product between vectors $\mathbf{a}$ and $\mathbf{b}$ is written as $\langle \mathbf{a}, \mathbf{b} \rangle$ or $\mathbf{a}^H \mathbf{b}$
$\mathbb{M}_n$	The $n \times n$ complex matrix space, with the inner product for square matrices $\mathbf{A}$ and $\mathbf{B}$ , $\langle \mathbf{A}, \mathbf{B} \rangle = \text{tr}(\mathbf{A}^H \mathbf{B})$ . The associated norm is $\ \mathbf{A}\ _F = \sqrt{\text{Tr}(\mathbf{A}^H \mathbf{A})}$
$\mathbb{H}_n$	Hermitian matrix space with size $n \times n$ in $\mathbb{M}_n$ , such that $\mathbb{H}_n = \{\mathbf{A} \in \mathbb{M}_n, \mathbf{A}^H = \mathbf{A}\}$
$\mathbb{P}_n$	Positive-definite matrix space. Open subset in $\mathbb{H}_n$ , $\mathbb{P}_n = \{\mathbf{A} \in \mathbb{H}_n, \langle \mathbf{x}, \mathbf{A} \mathbf{x} \rangle > 0, \forall \mathbf{x} \neq \mathbf{0}\}$
$T_{\mathbf{A}} \mathbb{P}_n$	The tangent space to $\mathbb{P}_n$ at point $\mathbf{A}$ , $\mathbf{A} \in \mathbb{P}_n$ , which can be written as $T_{\mathbf{A}} \mathbb{P}_n = \{\mathbf{A}\} \times \mathbb{H}_n$

**Table 2**  
EEG frequency domain DPs.

DP	Name	Definition
Basic statistics		
$v_{i,c,e}(t) \in \mathbb{R}$	EEG potential vector and its	EEG potential of the individual $i$ , electrode $c$ of $e$ -th epoch at a time $t$ or frequency $\omega$ for the Fourier
$v_{i,c,e}(\omega) \in \mathbb{C}$	Fourier transform	transform
$\mathbf{S}_i(\omega) \in \mathbb{P}_{N_c}$	Cross-spectral matrix	The covariance matrix of $v_{i,c,e}(\omega)$ across all epochs for an individual $i$ at the frequency $\omega$ which has been
$\mathcal{S}_i \in (\mathbb{C})^{N_c \times N_c \times N_{\omega}}$	Cross-spectral tensor	positive definite regularized $\mathcal{S}_{i, :, :, \omega} = \mathbf{S}_i(\omega)$
Traditional DPs		
$\mathbf{y}_i^\lambda \in (\mathbb{R})^{N_c N_{\omega}}$	Log-spectrum DPs	$\mathbf{y}_i^\lambda = [\lambda_i(\Delta\omega)^T, \dots, \lambda_i(N\omega\Delta\omega)^T]^T$ , $\lambda_i(\omega) \in (\mathbb{R})^{N_c}$
$\mathbf{y}_i^r \in \mathbb{R}^{N_m N_{\omega}}$	Coherence DPs	$\mathbf{y}_i^r = [\mathbf{r}_i(\Delta\omega)^T, \dots, \mathbf{r}_i(N\omega\Delta\omega)^T]^T$ $\mathbf{r}_i(\omega) \in (\mathbb{R})^{N_m}$ , $N_m = N_c(N_c + 1)/2$
$\mathbf{y}_i^\Psi \in (\mathbb{R})^{N_m N_{\omega}}$	Phase DPs	$\mathbf{y}_i^\Psi = [\Psi_i(\Delta\omega)^T, \dots, \Psi_i(N\omega\Delta\omega)^T]^T$ $\Psi_i(\omega) \in (\mathbb{R})^{N_m}$ , $N_m = N_c(N_c + 1)/2$
Riemannian DPs		
$\mathbf{y}_i^\theta \in (\mathbb{C})^{N_m N_{\omega}}$	Riemannian DPs	$\mathbf{y}_i^\theta = [\theta_i(\Delta\omega)^T, \dots, \theta_i(N\omega\Delta\omega)^T]^T$ $\theta_i(\omega) \in (\mathbb{R})^{N_m}$ , $N_m = N_c(N_c + 1)/2$

coherence, the absolute magnitude of the complex correlation coefficients:

$$\mathbf{r}_i(\omega) = \text{vech}[r_{i,c,c'}(\omega)],$$

$$r_{i,c,c'}(\omega) = \left| \frac{s_{i,c,c'}(\omega)}{\sqrt{s_{i,c,c}(\omega) \times s_{i,c',c'}(\omega)}} \right|,$$

$$c', c = 1, \dots, N_c$$

Also widely used is the phase:

$$\Psi_i(\omega) = \text{vech}[\psi_{i,c,c'}(\omega)],$$

$$\psi_{i,c,c'}(\omega) = \arctang \left[ \frac{\text{Real}(s_{i,c,c'}(\omega))}{\text{Imag}(s_{i,c,c'}(\omega))} \right],$$

$$c, c' = 1, \dots, N_c$$

The coherence and phase DPs for the whole tensor  $\mathcal{S}_i$  are:

$$\mathbf{y}_i^r = [\mathbf{r}_i(\Delta\omega)^T, \dots, \mathbf{r}_i(N\omega\Delta\omega)^T]^T$$

$$\mathbf{y}_i^\Psi = [\Psi_i(\Delta\omega)^T, \dots, \Psi_i(N\omega\Delta\omega)^T]^T$$

The  $\mathbf{y}_i^r$  and  $\mathbf{y}_i^\Psi$  DPs have been widely used in connectivity research. Unfortunately, when bundled as a set with log-spectral DPs, these “traditional DPs” are not jointly multivariate Gaussian<sup>2</sup>, even when applying any of the usual data transformations separately to each measure.

### 2.1.2. Riemannian qEEG DPs

The difficulties of traditional DPs mentioned above can be remedied with the concept of Riemannian geometry. Since the cross-spectral tensor  $\mathcal{S}_i$  comprises frontal slices  $\mathbf{S}_i(\omega)$ , we consider these first.

**2.1.2.1. Riemann geometry of the cross-spectra at a single frequency.** The  $\mathbf{S}_i(\omega)$  are well-known mathematical objects that we already identified as Hermitian positive definite (HPD) matrices with unique properties, as discussed in depth in Bhatia (2007). In particular, these elements of these matrices do not distribute freely in Euclidean space but instead live on the manifold of positive definite (PD) matrices  $\mathbb{P}_{N_c}$  and are restricted

<sup>2</sup> Empirical multivariate transformations can achieve this objective (Biscay Lirio et al., 1989), but they are time-consuming and not natural.

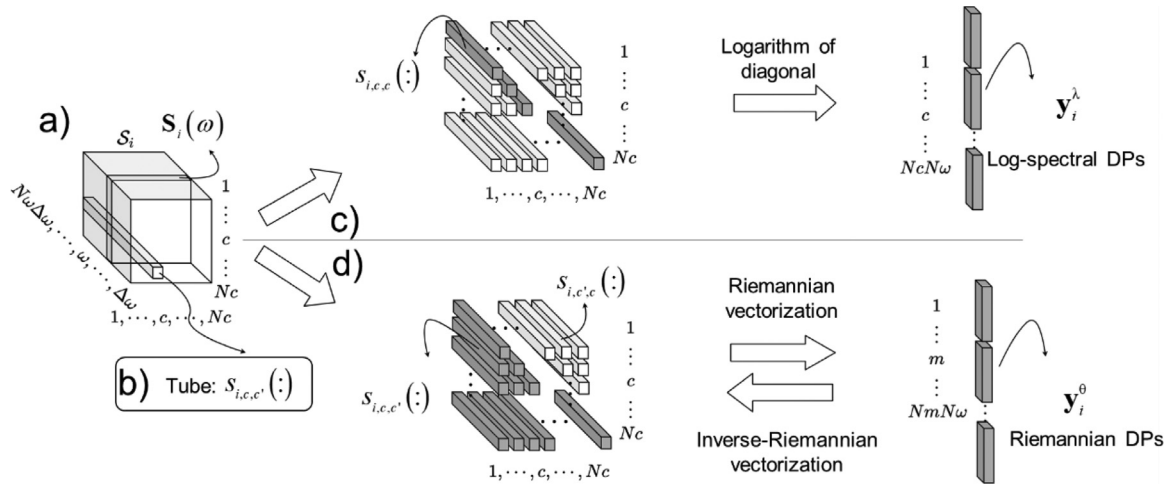


**Fig. 1.** The generation of traditional and Riemannian DPs. (a) The cross-spectral matrix  $S_i(\omega)$  is the frontal slices of the tensor  $\mathcal{S}_i$ ; (b) Fixing a channel and collecting all frequencies creates tubes  $s_{i,c,c'}(\cdot)$ . (c) Vertically stacking the diagonal tubes' logarithm generates the traditional log-spectral DPs vector  $\mathbf{y}_i^\lambda \in (\mathbb{R})^{N_c N \omega}$  for fixed channels. (d) Riemannian DPs result from the half-vectorization of the matrix logarithm of the geometrically centered  $S_i(\omega)$ , producing the vectors  $\mathbf{y}_i^\theta \in (\mathbb{R})^{NmN\omega}$ . The inverse process is labeled as  $\theta^{-1}$  which recovers  $\mathcal{S}_i$ .

to a hyper-dimensional cone (Pennec et al., 2006; Barachant et al., 2012). This property induces dependencies among the elements of each matrix, hence the nonlinear nature of the underlying manifold. The curved nature of this manifold precludes the use of simple Euclidean distances to quantify distances between cross-spectra, impeding the calculation of the usual norms and distances of previously involved in normative qEEG. Fortunately,  $\mathbb{P}_{N_c}$  endowed with the affine invariant metric, is a complete differentiable Riemannian manifold (Bhatia, 2007; Congedo et al., 2017).

In more detail, each point  $S_i(\omega)$  on the  $\mathbb{P}_{N_c}$  is associated with a local Euclidean vector space, known as the tangent space, denoted as  $T_{S_i(\omega)}\mathbb{P}_{N_c}$ . Each tangent space has a smoothly varying inner product, which defines the Riemannian metric locally (Pennec et al., 2006; Barachant et al., 2012; Congedo et al., 2017). We use two operators to pass from the manifold to the tangent space and back. The logarithmic mapping projects the  $S_i(\omega)$  to the tangent space  $T_C\mathbb{P}_{N_c}$  with respect to a reference (centering) matrix  $C$  (Pennec et al., 2006),

$$\begin{aligned} \text{Log}_C(S_i(\omega)) &= \mathbf{Q}_i(\omega) \\ &= C^{1/2} \text{logm}(C^{-1/2} S_i(\omega) C^{-1/2}) C^{1/2} \end{aligned}$$

where  $\text{logm}$  denotes matrix logarithm<sup>3</sup>. Furthermore, the inverse operator of logarithm mapping projects the tangent vector to the  $\mathbb{P}_{N_c}$  manifold with the exponential mapping,

$$\begin{aligned} \text{Exp}_C(\mathbf{Q}_i(\omega)) &= S_i(\omega) \\ &= C^{1/2} \text{expm}(C^{-1/2} \mathbf{Q}_i(\omega) C^{-1/2}) C^{1/2} \end{aligned}$$

where  $\text{expm}$  is the matrix exponential.

Thus, we can apply Euclidean calculations by transforming the original curved  $\mathbb{P}_{N_c}$  manifold to the tangent space where we assume that locally Gaussianity holds (Pennec, 1999). We achieve this transformation by the ‘‘Riemannian vectorization’’ operator (Pennec et al., 2006; Congedo et al., 2017; Sabbagh et al., 2020) on cross-spectral matrices, which produce the vector  $\theta_i(\omega)$  with the transformation of the space  $\mathbb{P}_{N_c} \rightarrow \mathbb{C}^{Nm}$ .

$$\theta_i(\omega) = \text{vech}[\text{logm}(C^{-1/2} S_i(\omega) C^{-1/2})] \quad (4)$$

which is known as a parallel transport on the  $\mathbb{P}_{N_c}$  manifold. Selection of the matrix  $C$  is crucial, and a typical choice is to select it

to whiten a given  $S_i(\omega)$ , that is, to minimize  $\|S_i(\omega) - I_{N_c}\|_F^2$ . For several  $S_i(\omega)$ , we need to center the whole sample with a single  $C$ , so that statistical calculations are carried out in a common tangent space (Arsigny et al., 2005; Barachant et al., 2013; Ng et al., 2016a). This objective is best achieved when  $C$  is closest in some sense to all the  $S_i(\omega)$  (Hauberg et al., 2013; Ng et al., 2016a). If we have reason to believe that  $S_i(\omega)$  are already whitened, then  $C = I_{N_c}$ , which is precisely the Log-Euclidean approach to Eq. (4) (Barachant et al., 2013; Ng et al., 2016b). Nevertheless, there is consensus that the optimal mean is  $C = G(s_1(\omega), \dots, s_{N_i}(\omega))$  where the function  $G$  is the Karcher mean (Bhatia and Holbrook, 2006; Karcher, 1977), also known as the Riemannian or geometric mean (Moakher, 2005; Bhatia and Holbrook, 2006). Also see (Tuzel et al., 2008; Barachant et al., 2012; Congedo et al., 2017). The estimation of the Karcher mean is highly nonlinear and must be calculated using iterative methods. In particular, we use the software implemented by Bini and Iannazzo (2013) (<http://bezout.dm.unipi.it/software/mmttoolbox/>) based on the Richardson-like iteration. Further details about the Riemannian geometric mean calculation are in Appendix B.1. We emphasize that though the calculation of the matrix  $C$  is highly nonlinear, the application of the centering operation  $C^{-1/2} S_i(\omega) C^{-1/2}$  is easily shown to be linear.

**2.1.2.2. Riemannian geometry of the tensors  $\mathcal{S}_i$ .** Our objects of study are the  $\mathcal{S}_i$  tensors which are HPD tensors, not matrices. Fortunately, we can leverage much work on specific third-order tensors (Braman, 2010; Kilmer et al., 2013; Lund, 2020). These third-order tensors have time or frequency as the third dimension, and an extensive theory associated with the ‘‘t-product’’ has been developed, which the PAVS lab has previously used to study time series (Karahan et al., 2015). Properties of  $\mathcal{S}_i$  follow from those of the matrix  $S_i^B = \text{blockdiag}(S_i(\Delta\omega), \dots, S_i(N\omega\Delta\omega))$ , which belongs to  $\mathbb{P}_{N_c N \omega}$  thus inheriting all the properties described in the previous section<sup>4</sup>. The centering operation in this new space is  $C^{B-1/2} S_i^B C^{B-1/2}$ , with  $C^B = \text{blockdiag}(C(\Delta\omega), \dots, C(N\omega\Delta\omega))$ . When we assume the same centering matrix for all frequencies, then  $C = \text{fold}(\text{blockdiag}^{-1}(I_{N_c \omega} \otimes C))$ . Thus, as with the single frequency case, estimating the centering matrix is a nonlinear operation, while applying tensor centering  $C^{B-1/2} S_i^B C^{B-1/2}$  is linear. We examine the most appropriate centering strategy for our data in Section 3.2.

<sup>3</sup> For matrix  $A \in \mathbb{P}_n$ , if the eigen decomposition of  $A$  is  $A = ULU^H$ ,  $\text{logm}(A) = \text{Udiag}(\log(l_1), \dots, \log(l_n))U^H$  and  $\text{expm}(A) = \text{Udiag}(\exp(l_1), \dots, \exp(l_n))U^H$ .

<sup>4</sup>  $S_i^B$  and  $\mathcal{S}_i$  are isomorphic, see Appendix B.2.

The application of Riemannian vectorization to the cross-spectral tensor produces the DP  $\mathbf{y}_i^0 \in \mathbb{C}^{NmN\omega}$  (Fig. 1-d),

$$\mathbf{y}_i^0 = [\boldsymbol{\theta}_i(\Delta\omega)^T, \dots, \boldsymbol{\theta}_i(N\omega\Delta\omega)^T]^T \quad (5)$$

This transformation guarantees that the  $\mathbf{y}_i^0(\omega)$  more closely satisfy the Multivariate Gaussianity assumption (Pennec, 1999). Note that we scale the off-diagonal  $\mathbf{y}_i^0(\omega)$  by  $\sqrt{2}$  preserving the equality of norms  $\|\mathbf{C}^{-1/2}\mathbf{S}_i(\omega)\mathbf{C}^{-1/2}\|_F = \|\mathbf{y}_i^0(\omega)\|_2$ .

The inverse operation of Riemannian vectorization returns the vectors from space of  $\mathbb{C}^{Nm}$  back to manifold  $\mathbb{P}_{Nc}$  (equation 8 of Sabbagh et al., 2020):

$$\mathbf{S}_i(\omega) = \expm(\mathbf{C}^{-1/2}(\text{vech}^{-1}(\mathbf{y}_i^0(\omega)))\mathbf{C}^{-1/2}) \quad (6)$$

## 2.2. The definition of qEEG norms

DPs are highly dependent on age and other covariates. For this reason, and considering for the moment only age, they have been adjusted by the “z transform” (John et al., 1977) to provide age-independent measures of BDD. Formally, the z-score is based on the following model, defined for any type of frequency domain DP

$$\mathbf{y}_i(\omega) = \boldsymbol{\mu}(\omega, a) + \boldsymbol{\sigma}(\omega, a) \odot \mathbf{e}_i, \quad \mathbf{e}_i \sim \mathcal{N}(\mathbf{0}, \mathbf{I}) \quad (7)$$

for any frequency  $\omega$  and age  $a$ .

Thus, the z score for any DP  $y_{i,c,c'}(\omega)$  of an individual, for electrode pairs  $(c, c')$  and frequency  $\omega$  is expressed in scalar form as:

$$z_{i,c,c'}(\omega) = \frac{y_{i,c,c'}(\omega) - \hat{\mu}_{c,c'}(\omega, a)}{\hat{\sigma}_{c,c'}(\omega, a)} \quad (8)$$

where  $\mu_{c,c'}(\omega, a)$  and  $\sigma_{c,c'}(\omega, a)$  are the frequency and age-dependent mean and SD, respectively. The functions  $\mu_{c,c'}(\omega, a)$  are known as “EEG Development Equations” (Ahn et al., 1980; John et al., 1977; Matoušek and Petersén, 1973) or “qEEG norms”. This concept of age-dependent norms also generalizes to include dependence on other independent variables such as sex, or as in the case of this paper country/device/study (batches). We shall call the new equations described in this paper “HarMNqEEG norm”.

The z-score is a probabilistic measure of the individual’s deviation from the normative population perhaps due to a BDD. Probabilistic statements about a z-score are most straightforward when the distribution of the DP for the normative sample is approximately Gaussian. Thus, it is convenient to transform DPs with a function that ensures this Gaussianity—a step carried out before calculating regression equations and z-scores.

## 2.3. The harmonized multinational qEEG project

### 2.3.1. Data acquisition

The HarMNqEEG collaboration is creating multinational norms for the cross-spectral tensors  $\mathcal{S}_i$ . The collaboration had two main components:

- Preparation of the data by the collaborators at each site for sharing information (Fig. 2-b)
- Processing of the shared data to achieve harmonized norms (Fig. 2-a).

We now summarize the workflow, explaining details separately in the subsequent sections.

The project was launched by an open international call for participation via the Global Brain Consortium (<https://globalbrainconsortium.org/>). The collaborative model only shared processed data, EEG cross-spectral tensors  $\mathcal{S}_i$  and anonymized metadata. This data was

obtained using the within-site software data\_gatherer MATLAB program, as shown in Fig. 2-b.

A prerequisite for any site to join the study was to have ethical approval by the corresponding authorities to share processed data (EEG cross-spectra tensors  $\mathcal{S}_i$ ) and anonymized metadata. The inclusion/exclusion criteria for the normal subjects have been described respectively in the reference, the last column of Appendix Table C1. These criteria are sufficiently and equally stringent to guarantee a sample of functionally healthy subjects.

Each site submitted a “batch” of samples. A sample contains a cross-spectral tensor  $\mathcal{S}_i$  and the metadata: sex,  $s_i$  age  $a_i$  and batch  $b_i$ . Here  $i$  tags each individual. See the dimensions of  $\mathcal{S}_i$  in the last block of Fig. 2-b.

To be accepted into the study, the batch had to fulfill the following requirements:

- It had to be part of a normative study or control group with explicit inclusion and exclusion criteria (see below).
- The  $\mathcal{S}_i$  had to be obtained with the MATLAB script (data\_gatherer) from at least one minute of artifact-free, eyes closed, quasi-stationary, resting-state EEG epochs  $\mathbf{v}_{i,e}(t)$ .
- Finally, the batch had to pass numerical quality control with partial or total rejection of the batch or samples being possible (detail see Section 3.1).

We explain some design decisions of this project, which were necessary given the significant difference in recording protocols for the different batches. We homogenized a minimalistic set of specifications applicable to all sites and devices:

- Recordings were from the 19 channels  $Nc = 19$  of the 10/20 International Electrodes Positioning System: Fp1, Fp2, F3, F4, C3, C4, P3, P4, O1, O2, F7, F8, T3/T7, T4/T8, T5/P7, T6/P8, Fz, Cz, Pz) (Standards and Best Practices organization for open and FAIR neuroscience | INCF).
- We started this effort from a legacy dataset, that of the first wave of the Cuban Human Brain Mapping data. The data of 211 subjects were stored as cross-spectral matrices sampled from 1.17 to 19.14 Hz, with a 0.39 Hz resolution. Since this data set has been well studied, we restricted the final analysis to the same range.
- For the rest of the datasets, we required that the amplifiers used to record all EEG data had at least a frequency response range from 0.5 to 35 Hz, even though subsequent processing reduced it to the restrict range mentioned.
- Each EEG was organized as a sequence of artifact-free 2.56 s (The segment length of EEG data was  $\lceil (1/2.56) \times (\text{SampleRate}) \rceil^5$ ). This format allows a frequency resolution of  $\Delta\omega = 0.39$  Hz (Bosch-Bayard et al., 2022).
- The scalp EEG cross-spectrum was calculated using Bartlett’s method (Møller, 1986) by averaging the periodograms of more than 20 consecutive and non-overlapping segments. While the uniform window of Bartlett’s method does not have the optimal statistical properties, extensive comparisons with multi-taper spectrum estimation showed little difference in the calculation of norms or machine learning classification.
- We provided the instruction of artifact cleaning work for each site, and the one-site artifact rejection did not include the use of ICA techniques.
- Following the principles of open science but respecting the researchers’ rights to retain control of their raw data, all these functionalities were encapsulated in a script programmed in MATLAB and distributed among the researchers in each recording site. (GitHub location of the script: [https://github.com/CCC-members/BC-V\\_group\\_stat/blob/master/data\\_gatherer.m](https://github.com/CCC-members/BC-V_group_stat/blob/master/data_gatherer.m)). Each site ran the script on their

<sup>5</sup>  $\lceil \cdot \rceil$ , round up to an integer.

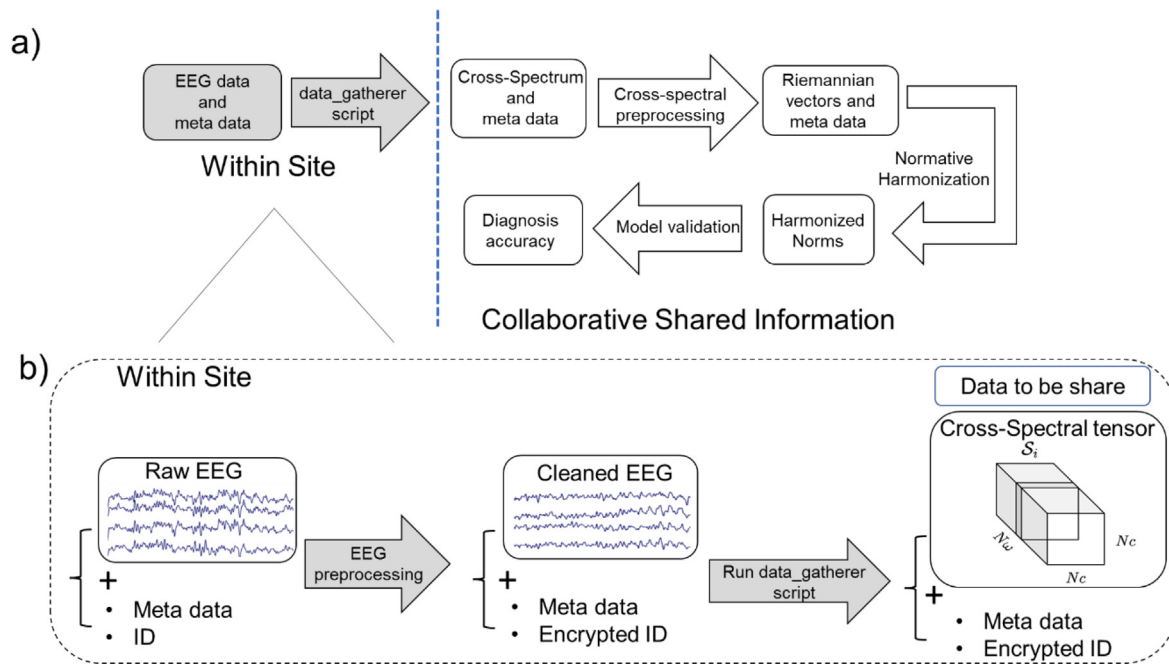


**Fig. 2.** Dataflow of the collaboration for the Harmonized qEEG norms. (a) General overview. Each collaborative site collected resting-state EEGs from healthy control subjects in the eyes closed condition (obtained from a normative study). After within-site quality control and artifact rejection, the MATLAB “data\_gatherer” script was used to obtain the EEG cross-spectrum for each participant, which, together with anonymized meta-data, constituted a “sample”. These samples were shared with the central processing site and, after further calculations, yielded qEEG DPs, traditional and Riemannian. In turn, these DPs were used to construct the harmonized qEEG norms. An independent data set of healthy subjects and those with Brain Developmental Disorders allowed the comparison of the diagnostic accuracy of different DPs. Boxes shaded in gray indicate data and process private to each collaborative site; (b) Further details of within-site processing. Each site carried out initial quality control of raw EEG recordings and metadata (sample), using procedures for artifact rejection. Samples with cleaned EEG and encrypted ID were processed to cross-spectrum and the encrypted meta data for further sharing.

data and only shared the processing results without sharing their raw data. Thus, they only shared the EEG cross-spectra, basic subjects’ information as an anonymized code, age, and sex, as well as technical parameters like recording conditions, montage, recording reference, EEG device used, laboratory, and country.

We define the term “batch” as a specific combination of country, device, and year of recordings (Table D1). Three different definitions of batches reflect different hypotheses, namely:

- (Country) Batches are the countries from which data comes.
- (Device) Batches are the specific type of equipment from which data come.
- (Study) Batches are the specific projects which generate a dataset, a combination of country, device, and the year of data recorded.

We tested whether batches, defined in various ways, need to be accounted for when calculating qEEG normative equations. If there are systematic differences between the normative equations of each batch, one must add a batch-specific additive correction to these equations.

The multinational call for the multinational qEEG norms and subsequent batch selection produced 1792 samples. After quality control, samples diminished to 1564, with 783 females and 781 males. A further breakdown of the samples by country, device, study, and age range is in Table C1.

**Fig. 3.** The dataset was collected from 9 countries, including Barbados, China, Colombia, Cuba, Germany, Malaysia, Russia, Switzerland, and the USA. The ages of samples for multinational EEG norms cover the whole life span (5–95 years). Sampling is skewed towards younger participants, reflecting sampling of normative projects involved.

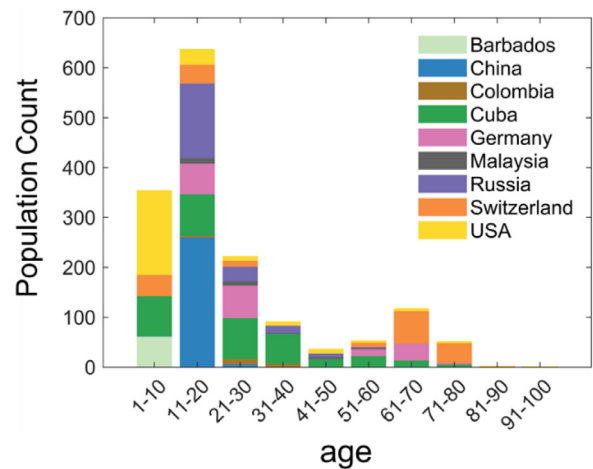


**Fig. 3.** Gives an overview of the age range of the samples is 5–97 years. The Age distribution of the Multinational qEEG norms sample is skewed towards younger ages, with relatively fewer samples older than 65 years. In addition, there is an almost balanced gender distribution for all the samples.

### 2.3.2. Preprocessing procedures and transformation of DPs towards Gaussianity

To be able to pool all cross-spectrum under the same framework, at the same time controlling for irrelevant nuisance variables, we implemented the following preprocessing steps:

**2.3.2.1. Average reference.** We carried additional centering of all cross-spectrum matrices  $\mathbf{S}_i(\omega)$  from their original recording montages to the average reference (Hu et al., 2019):

$$\tilde{\mathbf{S}}_i(\omega) = [\mathbf{H}\mathbf{S}_i(\omega)\mathbf{H}^T]_{1:(Nc-1),1:(Nc-1)}$$

with the operator  $\mathbf{H} = \mathbf{I}_{Nc} - \mathbf{1}_{Nc}\mathbf{1}_{Nc}^T/Nc$ . This type of centering should not be confused with the centering described in the section on Riemannian DPs.

The average reference operation introduces an exact linear dependence between electrodes, a property common to all unipolar references (Hu et al., 2019). We deemed it expedient to eliminate one of the redundant electrodes, for which we chose the electrode (Pz). Note that the number of electrodes  $Nc$  changes from 19 to 18.

**2.3.2.2. Regularization of symmetric semi-positive definite matrices.** We regularized sample cross-spectrum matrices to ensure them to be of full rank. We used the Maximum likelihood shrinkage factor described in (Schneider-Luftman and Walden, 2016). The  $\tilde{\mathbf{S}}_i(\omega)$  are Hermitian matrices, and frequently are rank reduced. To guarantee subsequent Riemannian operations (especially the matrix logarithm operator), we regularized  $\tilde{\mathbf{S}}_i(\omega)$  to ensure positive definiteness. Regularization was achieved with Hilbert-Schmidt (HS) loss,

$$\begin{aligned} \mathcal{L}_{\text{HS}} &\triangleq E \left\{ \text{Tr} \left\{ \left( \widehat{\mathbf{S}}_i(\omega; \rho_i) - \tilde{\mathbf{S}}_i(\omega) \right)^2 \right\} \right\} \\ &= E \left\{ \left\| \widehat{\mathbf{S}}_i(\omega; \rho_i) - \tilde{\mathbf{S}}_i(\omega) \right\|_F^2 \right\} \end{aligned}$$

For the ill-conditioned case, take the shrinkage coefficient as Walden and Schneider-Luftman (2015),

$$\rho_i(\omega) = \left[ 1 - \frac{Ne}{Nc} + Ne \frac{\alpha}{\text{Tr}^2(\tilde{\mathbf{S}}_i(\omega))} \right]^{-1}$$

The estimation is,

$$\widehat{\mathbf{S}}_i(\omega) = (1 - \rho_i(\omega))\tilde{\mathbf{S}}_i(\omega) + \rho_i(\omega) \frac{\text{Tr}(\tilde{\mathbf{S}}_i(\omega))}{Nc} \mathbf{I}_{Nc}$$

where  $\alpha = \text{Tr}\{(\tilde{\mathbf{S}}_i(\omega))^2\} - (1/Ne)\text{Tr}^2(\tilde{\mathbf{S}}_i(\omega))$ ,  $Ne$  is the number of EEG epochs here.

**2.3.2.3. Global-scale factor correction.** Though two EEG recordings may show a similar appearance, they may differ significantly in overall amplitude. This observation is modeled as a general gain factor which is randomly varying for similar EEG data. These sources of variance arise from different EEG devices, recording conditions, amplifiers, and other subject characteristics (skull thickness, hair thickness, skin impedance, and other non-physiological factors). A solution to this nuisance source of variability is to rescale the cross-spectra by a random general scale factor (GSF) as described in Hernández et al., (1994). These authors showed that the maximum likelihood estimate of the GSF for an individual is the geometric average of all log power values across all derivations.

For the sake of completeness, we summarized the GSF method here. Suppose for an individual  $i$ , the EEG potential recorded at the electrode  $c$  is  $v_{i,e,c}(t) = \gamma_i \beta_{i,e,c}(t)$ , the global scale factor  $\gamma_i$  is independent of epoch and electrode and the constant  $\beta_{i,e,c}(t)$  is the GSF-independent EEG scale.

Taking the Eigen-decomposition  $\widehat{\mathbf{S}}_i(\omega) = \mathbf{\Gamma}_i(\omega)\mathbf{D}_i(\omega)\mathbf{\Gamma}_i^H(\omega)$ , where  $\mathbf{\Gamma}_i(\omega)$  is the eigenvector matrix and  $\mathbf{D}_i(\omega)$  is the diagonal matrix of eigenvalues.

Rescaling the  $\widehat{\mathbf{S}}_i(\omega)$  we have:

$$\begin{aligned} \log \frac{\widehat{\mathbf{S}}_i(\omega)}{\gamma_i^2} &= \mathbf{\Gamma}_i(\omega) \log \frac{\mathbf{D}_i(\omega)}{\gamma_i^2} \mathbf{\Gamma}_i^H(\omega) \\ &= \mathbf{\Gamma}_i(\omega) (\log \mathbf{D}_i(\omega) - \kappa_i \mathbf{I}) \mathbf{\Gamma}_i^H(\omega) \end{aligned}$$

$$\begin{aligned} &= \mathbf{\Gamma}_i(\omega) \log \mathbf{D}_i(\omega) \mathbf{\Gamma}_i^H(\omega) - \kappa_i \mathbf{I} \\ &= \log \widehat{\mathbf{S}}_i(\omega) - \kappa_i \mathbf{I} \end{aligned} \quad (9)$$

Thus, the GSF affects the diagonal of the cross-spectrum (the log spectra). The estimator of  $\kappa_i$  is the geometric mean of power spectrum,  $\kappa_i = 2 \log(\gamma_i)$ ,

$$\hat{\kappa}_i = \frac{1}{N\omega Nc} \sum_{\omega=3\Delta\omega}^{N\omega} \sum_{c=1}^{Nc} \log \left( \widehat{s}_{i,c,c}(\omega) \right) \quad (10)$$

Then the GSF-corrected cross-spectrum can be represented as,

$$\widetilde{\mathbf{S}}_i(\omega) = \widehat{\mathbf{S}}_i(\omega) / \exp(\hat{\kappa}_i) \quad (11)$$

**2.3.2.4. The logarithm of spectra and Riemannian vectorization of cross-spectra.** The final step is to transform the DPs towards gaussianity:

For the traditional log-spectrum DPs, get  $\mathbf{y}_i^{\lambda}$  with diagonal logarithm operator as in the Eq. (1). To obtain  $\mathbf{y}_i^{\lambda}$ , we only apply steps 2.3.2.1 and 2.3.2.3 for preprocessing.

For the Riemannian DPs, we transform  $\mathbf{S}_i(\omega)$  to the Euclidean tangent space,  $\mathbf{y}_i^{\theta}$  employing the Riemannian vectorization operator as in the Eq. (5).

## 2.4. Construction of multinational harmonized qEEG norms

### 2.4.1. Possible normative models

Here, for the HarMNqEEG modeling, we work on the two types of DPs,  $\mathbf{y}_{i,c,c'}^m(\omega)$ ,  $m = \lambda$  or  $\theta$ , where  $m$  are types of DPs shown in Table 3, which we assume satisfy the gaussian distribution. In Table 3, we summarize normative equations and related z-scores.

Each  $\mathbf{y}_{i,c,c'}^m(\omega)$  can be expressed as a general linear model (GLM):

$$\mathbf{y}_{i,c,c'}^m(\omega) = \mu_{c,c'}^m(\omega, a_i, s_i, b_i) + \sigma_{c,c'}^m(\omega, a_i, s_i, b_i) \epsilon_{i,c,c'}^m(\omega), \epsilon_{i,c,c'}^m(\omega) \sim \mathcal{N}(0, 1) \quad (12)$$

where  $\mu_{c,c'}^m(\omega, a, s, b)$  and  $\sigma_{c,c'}^m(\omega, a, s, b)$  are the population means and SD, respectively. Henceforth, the value of a variable for an individual is denoted with a subscript, e.g.  $a_i$ . Also, the symbol "." instead of a variable indicates that it is pooled over all individuals. These conventions for indices are summarized in Appendix Table A.1.

Unfortunately, the general HarMNqEEG model (12) is very "data greedy", being too complex. For that reason, we explore more parsimonious additive models, each depending on a smaller subset of variables. Instead of the general  $\mu_{c,c'}^m(\omega, a, s, b)$ , we consider the additive models described in Table 4. The most trivial model assumes that  $\mu_{c,c'}^m(\omega, a, s, b)$  is a constant  $\mu_{c,c'}^m(\cdot, \cdot, \cdot, \cdot)$ . Given PAVS lab prior work, we chose as fixed effects only frequency and age, with possible models  $\mu_{c,c'}^m(\omega, \cdot, \cdot, \cdot)$ ,  $\mu_{c,c'}^m(\cdot, a, \cdot, \cdot)$ , and  $\mu_{c,c'}^m(\omega, a, \cdot, \cdot)$ . We then consider additional constant additive random effects that depend on batch,  $\mu_{c,c'}^m(\omega, a, \cdot, \cdot) + \mu_{b,c,c'}^m(\cdot, \cdot, b, \cdot)$ , sex,  $\mu_{c,c'}^m(\omega, a, \cdot, \cdot) + \mu_{s,c,c'}^m(\cdot, \cdot, s, \cdot)$  or batch and sex  $\mu_{c,c'}^m(\omega, a, \cdot, \cdot) + \mu_{s,c,c'}^m(\cdot, \cdot, s, \cdot) + \mu_{b,c,c'}^m(\cdot, \cdot, b, \cdot)$ . We finally look at the last level of complexity for the population mean: the additive random effects (for example, the random effect is a batch effect), instead of being constant, are now functions of frequency and age,  $\mu_{b,c,c'}^m(\omega, \cdot, \cdot, b)$ ,  $\mu_{b,c,c'}^m(\cdot, a, \cdot, b)$ , and  $\mu_{b,c,c'}^m(\omega, a, \cdot, b)$ .

Similarly to the mean, we model the standard deviation (SD) as shown in Table 5 with fixed effects, for example,  $\log \sigma_{c,c'}^m(\cdot, \cdot, \cdot, \cdot)$  or  $\log \sigma_{c,c'}^m(\omega, a, \cdot, \cdot)$ . Additive batch random effects considered were either constant  $\log \sigma_{b,c,c'}^m(\cdot, \cdot, \cdot, b)$  or functions  $\log \sigma_{b,c,c'}^m(\omega, \cdot, \cdot, b)$  and  $\log \sigma_{b,c,c'}^m(\cdot, a, \cdot, b)$  dependent on frequency and age, respectively. To refer to any specific normative model we combine the labels for the mean and SD contained in Table 4 and Table 5. For example the norm with fixed mean and SD is termed 0-A.

When fitting these models, we follow a sequential strategy, fitting first the fixed effects and then, based on the residuals or z score of

**Table 3**  
Normative equations and related z-scores.

Variable	Name	Definition
$y_{i,c,c'}^m(\omega)$	DPs of type $m$	For the subject $i$ , electrode pairs $(c, c')$ , at frequency $\omega$ . $m$ is any of the DPs types $m = \{\lambda, \theta, r, \psi\}$ , and the definition of DPs types is in Table II.
$\mu_{c,c'}^m(\omega, a, s, b)$	The Normative mean of $y_{i,c,c'}^m(\omega)$	$\mathbb{E}[y_{i,c,c'}^m(\omega)]$
$\sigma_{c,c'}^m(\omega, a, s, b)$	The normative standard deviation of $y_{i,c,c'}^m(\omega)$	$\mathbb{E}[(y_{i,c,c'}^m(\omega) - \hat{\mu}_{c,c'}^m(\omega, a_1, s_1, b_1))^2]$
$z_{i,c,c'}^m(\omega)$	Global z-score	$z_{i,c,c'}^m(\omega) = \frac{y_{i,c,c'}^m(\omega) - \hat{\mu}_{c,c'}^m(\omega, a_1, \cdot, \cdot)}{\hat{\sigma}_{c,c'}^m(\omega, a_1, \cdot, \cdot)}$
$\mu_{s/b,c,c'}^m(\omega, a, s, b)$	Sex/batch-corrected mean of $y_{i,c,c'}^m(\omega)$	$\mathbb{E}[z_{i,c,c'}^m(\omega)]$
$\sigma_{s/b,c,c'}^m(\omega, a, s, b)$	Sex/batch-corrected standard deviation of $y_{i,c,c'}^m(\omega)$	$\mathbb{E}[(z_{i,c,c'}^m(\omega) - \hat{\mu}_{s/b,c,c'}^m(\omega, a_1, s_1, b_1))^2]$
$z_{i,c,c'}^{ms}(\omega)$	Sex/batch-corrected z-score of $y_{i,c,c'}^m(\omega)$	$z_{i,c,c'}^{ms}(\omega) = \frac{z_{i,c,c'}^m(\omega) - \hat{\mu}_{s/b,c,c'}^m(\omega, a_1, s_1, b_1)}{\hat{\sigma}_{s/b,c,c'}^m(\omega, a_1, s_1, b_1)}$
$z_{i,c,c'}^{ms}(\omega)$	Sex/batch-corrected z-score of $y_{i,c,c'}^m(\omega)$	$\hat{\mu}_{s/b,c,c'}^m(\omega, a_1, s_1, b_1) = \frac{\hat{\mu}_{s/b,c,c'}^m(\omega, a_1, s_1, b_1)}{\hat{\sigma}_{c,c'}^m(\omega, a_1, \cdot, \cdot)}$ $\hat{\sigma}_{s/b,c,c'}^m(\omega, a_1, s_1, b_1) = \frac{\hat{\sigma}_{s/b,c,c'}^m(\omega, a_1, s_1, b_1)}{\hat{\sigma}_{c,c'}^m(\omega, a_1, \cdot, \cdot)}$
$y_{i,c,c'}^{ms}(\omega)$	Harmonized $y_{i,c,c'}^m(\omega)$	$y_{i,c,c'}^{ms}(\omega) = z_{i,c,c'}^{ms}(\omega) \times \hat{\sigma}_{c,c'}^m(\omega, a_1, \cdot, \cdot) + \hat{\mu}_{c,c'}^m(\omega, a_1, \cdot, \cdot)$
$\mu_{c,c'}^{ms}(\omega, a, \cdot, \cdot)$	The harmonized normative mean of $y_{i,c,c'}^m(\omega)$	$\mathbb{E}[y_{i,c,c'}^{ms}(\omega)]$

**Table 4**  
Extended bayesian information criterion of models for DPs.

Model component type	Label	Population mean functions	nBIC $\gamma_{i,c,c'}^\lambda(\omega)$	nEBIC $\gamma_{i,c,c'}^\theta(\omega)$
I: Fixed effects	0	$\mu_{c,c'}^m(\cdot, \cdot, \cdot, \cdot)$	1.000	0.995
	1	$\mu_{c,c'}^m(\omega, \cdot, \cdot, \cdot)$	0.995	0.715
	2	$\mu_{c,c'}^m(\cdot, a, \cdot, \cdot)$	0.321	1.000
	3	$\mu_{c,c'}^m(\omega, a, \cdot, \cdot)$	0.164	0.711
II: Constant random effects	4	$\mu_{c,c'}^m(\omega, a, \cdot, \cdot) + \mu_{b,c,c'}^m(\cdot, \cdot, b, \cdot)$	0.154	0.285
	5	$\mu_{c,c'}^m(\omega, a, \cdot, \cdot) + \mu_{s,c,c'}^m(\cdot, \cdot, s, \cdot)^*$	0.164	0.710
	6	$\mu_{c,c'}^m(\omega, a, \cdot, \cdot) + \mu_{s,c,c'}^m(\cdot, \cdot, s, \cdot) + \mu_{b,c,c'}^m(\cdot, \cdot, b, \cdot)^*$	0.155	0.287
III: Functional random effects	7	$\mu_{c,c'}^m(\omega, a, \cdot, \cdot) + \mu_{b,c,c'}^m(\omega, \cdot, \cdot, b)$	0.111	0.315
	8	$\mu_{c,c'}^m(\omega, a, \cdot, \cdot) + \mu_{b,c,c'}^m(\cdot, a, \cdot, b)$	0.153	0.211
	9	$\mu_{c,c'}^m(\omega, a, \cdot, \cdot) + \mu_{b,c,c'}^m(\omega, a, \cdot, b)$	0.127	0.631

**Table 5**  
Models for the population logarithm SD.

Label	Population logarithm SD functions	nBIC $\gamma_{i,c,c'}^\lambda(\omega)$	nEBIC $\gamma_{i,c,c'}^\theta(\omega)$
A	$\log \sigma_{c,c'}^m(\cdot, \cdot, \cdot, \cdot)$	0.111	0.211
B	$\log \sigma_{c,c'}^m(\cdot, \cdot, \cdot, \cdot) + \log \sigma_{b,c,c'}^m(\cdot, \cdot, \cdot, b)$	0.104	0.041
C	$\log \sigma_{c,c'}^m(\omega, a, \cdot, \cdot)$	0.014	0.107
D	$\log \sigma_{c,c'}^m(\omega, a, \cdot, \cdot) + \log \sigma_{b,c,c'}^m(\cdot, \cdot, \cdot, b)$	0.008	0.008
E	$\log \sigma_{c,c}^\lambda(\omega, a, \cdot, \cdot) + \log \sigma_{b,c,c}^\lambda(\omega, \cdot, \cdot, b)$	0	-
	$\log \sigma_{c,c'}^\theta(\omega, a, \cdot, \cdot) + \log \sigma_{b,c,c'}^\theta(\cdot, a, \cdot, b)$	-	0

this fit, we fit the random effects if required. A concrete example of this is deferred to Section 3.3. All estimates of the mean function and SD functions (including fixed and random effects) are obtained with the Nadaraya-Watson (NW) kernel regression (Nadaraya, 1964). This nonparametric smoothing method depends on the bandwidth hyperparameter and the more smoothed the data, the less complex the model. The complexity of the model is reflected in the “equivalent” degrees of freedom (Fisher, 1922). Special consideration was given to estimating the population variance as it does not have a Gaussian distribution as assumed by NW regression. Instead, for the variance, we used the modified NW regression to estimate the variance function for heavy-tailed innovation (Chen et al., al.,2009).

To stabilize sub-sample (batch or sex) estimators, we fixed their smooths to the same bandwidth as the global smooth, thus using the bandwidths obtained with all the data for the smaller samples. The shared bandwidth chosen for each model is optimal for a given DP set  $\{y_{i,c,c'}^m(\omega), c' \leq c = 1, \dots, Nc\}$  for the model  $\mu_{c,c'}^m(\omega, a, \cdot, \cdot)$  and

$\sigma_{c,c'}^m(\omega, a, \cdot, \cdot)$ . In this paper, the bandwidths for the mean smooth were 0.4 and 0.48 for frequency and age, respectively. The corresponding bandwidths for the variance smooth are 0.6 and 0.72.

Due to the large amount of computation needed for our models, instead of applying ordinary NW regression, we used an in-house procedure Fast multivariate kernel regression with nufft (FKreg). Our FKreg is a nonparametric multiple multivariate kernel regression based on a fast binning algorithm (Wand, 1994) which executes in  $O(n + m \log m)$  operations instead of  $O(nm)$ , and usually, the gridding points  $m$  are less than the number of samples  $n$ . About the FKreg in-house code, we mention that it includes the capability for complex-valued DPs regression (The paper of FKreg is under preparation). We, therefore, use the FKreg algorithm to estimate real and imaginary smooths of DPs simultaneously with a common variance. To our knowledge, this is the first instance of complex-valued qEEG harmonized norms. We also used a fast bandwidth selection for multiple multivariate smooth. The speed-up was possible by the use of the randomized generalized-cross-validation (rGCV)

to approximate the best range of degrees of freedom (df) (Girard, 1989). Subsequently, we fine-tune the df with the more accurate (but less time-consuming) method than Turlach and Wand (1996).

The COMBAT model (Johnson et al., 2007) is our model 4-B for  $y_{i,c,c'}^m(\omega)$ , GAMLSS (Rigby and Stasinopoulos, 2005) is our model 7-E and 8-E for  $y_{i,c,c'}^\lambda(\omega)$  and  $y_{i,c,c'}^\theta(\omega)$  separately. For Gaussian noise, both these models are just particular instances of our formulations.

#### 2.4.2. Normative model selection

As mentioned in Section 2.4.1, the Eq. (12) can have different specifications. To find the optimal HarMNqEEG model, we minimize information-theoretic measures that are a tradeoff between model fit and model complexity. For standard statistical scenarios, examples of these criteria are Akaike's information criterion (AIC) (Akaike, 1973), cross-validation (CV) (Stone, 1974), generalized cross-validation (GCV) (Craven and Wahba, 1978). The Bayes information criterion (BIC) (Schwarz, 1978) is of particular interest due to its good properties and adopted in this paper.

Unfortunately, for the Riemannian DPs, the number of DPs is large compared to the samples. This excess of variables is the "small-n-large-P" problem, common in bioinformatics and neuroimaging, making most model comparison criteria (including BIC) perform poorly. BIC performs too "liberally," usually picking excessively complex models. Chen and Chen (2008) proposed a correction for BIC in the "small n large p" scenario. They diagnosed that the uniform prior on the model space is the cause of BIC's liberality in the small-n-large-P setting. They correct this problem with a family of Extended Bayes information criteria (EBIC) (Chen and Chen, 2012). The EBIC value for a model is,

$$\text{EBIC} = -2 \ln(\mathcal{L}) + K \log n + 2K\eta \log P \quad (13)$$

where  $K$  is the model's degree of freedom,  $\mathcal{L}$  is the model likelihood, and  $P$  is the number of DPs variables where the relation with sample number is  $P = O(n^k)$ . The selection of  $\eta$  should be  $\eta > 1 - 1/2k$ . Here, for Riemannian DPs,  $P = 15288 (N\omega Nc^2)$ ,  $n = 1564$ , we set  $\eta = 0.7$ . The calculations of EBIC are independent for all possible models. To better compare the EBIC values, we use the normalized EBIC (nEBIC), scaled to [0,1] for model selection. For traditional DPs, since  $P < n$ ,  $P = 846(N\omega Nc)$ , we used normalized BIC (nBIC) values for model selection.

Table 4 and Table 5 show the nBIC and nEBIC values for the sequence of tested models, containing results for both  $y_{i,c,c'}^\lambda(\omega)$  and  $y_{i,c,c'}^\theta(\omega)$  separately. We thus ranked models based on the nBIC/nEBIC criterion and selected the optimal HarMNqEEG model with the lowest nBIC/nEBIC. The model selection list here are the results for "batch" defined by study that we did the parallel model selections with other batch definitions (country and device mentioned in Section 2.3.1) and selected the best batch definition with lowest nBIC/nEBIC value Table E1.

We first examined the optimal structure for the mean function in the equation, assuming a homoscedastic variance model that  $y_{i,c,c'}^m(\omega)$  was a constant. The trivial model  $\mu_{c,c'}^m(\cdot, \cdot, \cdot, \cdot)$ , labeled as "0" in Table 4, assumes no dependence on any covariates and is only included as a baseline null model. Models with frequency and age fixed effects, labeled 1–3 in Table 4, were checked next. Note that a model depending on frequency alone did not noticeably lower the nBIC/nEBIC. On the other hand, modeling age substantially decreased the criterion. The combination of age and frequency achieved the minimum (marked with light gray in the level I). Thus  $\mu_{c,c'}^m(\omega, a, \cdot, \cdot)$  was kept as a fixed effect for all subsequent models tested.

Next, we turned attention to the models that add constant random effects related to sex or batch, labeled 4 to 6. One can see that the best model depends only on the batch effect for  $y_{i,c,c'}^m(\omega)$  (marked with light gray in the level II). Surprisingly, including gender as a covariate does not improve the criterion. Gender also deteriorates model performance when batch effects are included (models with an asterisk). We, therefore, discounted gender from further exploration. Finally, we focused on functional random additive effects for the homoscedastic

model family where batch interacts with age and frequency (models 7 to 8). For  $y_{i,c,c'}^\lambda(\omega)$ , the optimal model includes both variables  $\mu_{c,c'}^\lambda(\omega, a, \cdot, \cdot) + \mu_{b,c,c'}^\lambda(\omega, \cdot, \cdot, b)$ . Contrary to our initial expectations, the random functional effect chosen for  $y_{i,c,c'}^\theta(\omega)$  was  $\mu_{c,c'}^\theta(\omega, a, \cdot, \cdot) + \mu_{b,c,c'}^\theta(\cdot, a, \cdot, b)$ , which depended on age but not frequency.

At this stage, an inspection of the models' residuals suggested that the homoscedastic assumption is not realistic. We, therefore, searched for the best model for the SD, as we show in Table 5. All heteroscedastic models improved substantially on the homoscedastic one (model 7-A and 8-A for  $y_{i,c,c'}^\lambda(\omega)$  and  $y_{i,c,c'}^\theta(\omega)$ ). Note that we assumed that the model for the SD should have a similar form as for the mean. This choice is plausible, reducing the number of models to examine. The model with overall lower nBIC/nEBIC is  $\log \sigma_{c,c'}^\lambda(\omega, a, \cdot, \cdot) + \log \sigma_{b,c,c'}^\lambda(\omega, \cdot, \cdot, b)$  for  $y_{i,c,c'}^\lambda(\omega)$ , and  $\log \sigma_{c,c'}^\theta(\omega, a, \cdot, \cdot) + \log \sigma_{b,c,c'}^\theta(\cdot, a, \cdot, b)$  for  $y_{i,c,c'}^\theta(\omega)$ .

To summarize, the optimal normative model selected for  $y_{i,c,c'}^\lambda(\omega)$  was,

$$\begin{aligned} \mu_{c,c'}^\lambda(\omega, a, s, b) &= \mu_{c,c'}^\lambda(\omega, a, \cdot, \cdot) + \mu_{b,c,c'}^\lambda(\omega, \cdot, \cdot, b) \\ \log \sigma_{c,c'}^\lambda(\omega, a, s, b) &= \log \sigma_{c,c'}^\lambda(\omega, a, \cdot, \cdot) + \log \sigma_{b,c,c'}^\lambda(\omega, \cdot, \cdot, b) \end{aligned} \quad (14)$$

The optimal model for  $y_{i,c,c'}^\theta(\omega)$  was:

$$\begin{aligned} \mu_{c,c'}^\theta(\omega, a, s, b) &= \mu_{c,c'}^\theta(\omega, a, \cdot, \cdot) + \mu_{b,c,c'}^\theta(\cdot, a, \cdot, b) \\ \log \sigma_{c,c'}^\theta(\omega, a, s, b) &= \log \sigma_{c,c'}^\theta(\omega, a, \cdot, \cdot) + \log \sigma_{b,c,c'}^\theta(\cdot, a, \cdot, b) \end{aligned} \quad (15)$$

#### 2.4.3. Optimal normative model

The HarMNqEEG norms are data and procedures that calculate global and harmonized z-scores. It does this by using the model (14) for the  $y_{i,c,c'}^\lambda(\omega)$  and the model (15) for the  $y_{i,c,c'}^\theta(\omega)$ . The norms thus contain information for calculating the global developmental surface of means and SDs, with additional batch corrections for the models described in Section 2.4.2. For the  $y_{i,c,c'}^m(\omega)$ ,  $m = \lambda$  or  $\theta$ , the basic model is:

$$\begin{aligned} y_{i,c,c'}^m(\omega) &= \mu_{c,c'}^m(\omega, a_i, \cdot, \cdot) + \mu_{c,c'}^m(\omega, a_i, \cdot, b_i) + \sigma_{b,c,c'}^m(\omega, a_i, \cdot, b_i) \varepsilon_{i,c,c'}^m(\omega) \\ \varepsilon_{i,c,c'}^m &\sim \mathcal{N}(0, 1) \end{aligned}$$

For computational expediency, to carry out sequential z-scores for the fixed and random effects, we rescale the random effects mean and the SD by dividing them with the fixed effect SD that  $\tilde{\mu}_{b,c,c'}^m(\omega, a_i, \cdot, b_i) = \frac{\mu_{b,c,c'}^m(\omega, a_i, \cdot, b_i)}{\sigma_{c,c'}^m(\omega, a_i, \cdot, \cdot)}$  and  $\tilde{\sigma}_{b,c,c'}^m(\omega, a_i, \cdot, b_i) = \frac{\sigma_{b,c,c'}^m(\omega, a_i, \cdot, b_i)}{\sigma_{c,c'}^m(\omega, a_i, \cdot, \cdot)}$ . The modified model now reads:

$$\begin{aligned} y_{i,c,c'}^m(\omega) &= \mu_{c,c'}^m(\omega, a_i, \cdot, \cdot) + \sigma_{c,c'}^m(\omega, a_i, \cdot, \cdot) \tilde{\mu}_{b,c,c'}^m(\omega, a_i, \cdot, b_i) \\ &\quad + \sigma_{c,c'}^m(\omega, a_i, \cdot, \cdot) \tilde{\sigma}_{b,c,c'}^m(\omega, a_i, \cdot, b_i) \varepsilon_{i,c,c'}^m(\omega) \\ \varepsilon_{i,c,c'}^m(\omega) &\sim \mathcal{N}(0, 1) \end{aligned} \quad (17)$$

The steps to obtain the z-scores for  $y_{i,c,c'}^m(\omega)$  are:  $\mu_{b,c,c'}^m(\omega, a_i, \cdot, b_i)$  and  $\sigma_{b,c,c'}^m(\omega, a_i, \cdot, b_i)$

- We first ignore the possible batch effects and fit global estimates for  $\hat{\mu}_{c,c'}^m(\omega, a_i, \cdot, \cdot)$  and  $\hat{\sigma}_{c,c'}^m(\omega, a_i, \cdot, \cdot)$
- We then calculate the "batch-free" z-score value as

$$z_{i,c,c'}^m(\omega) = \frac{y_{i,c,c'}^m(\omega) - \hat{\mu}_{c,c'}^m(\omega, a_i, \cdot, \cdot)}{\hat{\sigma}_{c,c'}^m(\omega, a_i, \cdot, \cdot)} \quad (18)$$

We obtain the batch-specific mean estimators  $\hat{\mu}_{b,c,c'}^m(\omega, a_i, \cdot, b_i)$  and SD estimators  $\hat{\sigma}_{b,c,c'}^m(\omega, a_i, \cdot, b_i)$ . The batch-harmonized z-score is:

$$z_{i,c,c'}^{m*}(\omega) = \frac{z_{i,c,c'}^m(\omega) - \hat{\mu}_{b,c,c'}^m(\omega, a_i, \cdot, b_i)}{\hat{\sigma}_{b,c,c'}^m(\omega, a_i, \cdot, b_i)} \quad (19)$$

The HarMNqEEG norms  $\mu_{c,c'}^{m*}(\omega, a)$  for  $y_{i,c,c'}^m(\omega)$  are obtained by smoothing the batch harmonized  $y_{i,c,c'}^m(\omega)$ ,  $y_{i,c,c'}^{m*}(\omega) = \hat{\sigma}_{c,c'}^m(\omega, a_i, \cdot, \cdot) \times z_{i,c,c'}^{m*}(\omega) + \hat{\mu}_{c,c'}^m(\omega, a_i, \cdot, \cdot)$

Note that since we removed all random effects, we can omit the "." symbols and use the notation  $\mu_{c,c'}^{m*}(\omega, a)$  for the mean functions.

### 3. Results

#### 3.1. Quality control

We implemented three distinct stages of quality control:

1. The first filter for quality control and correction or elimination of outliers was at each recording site. At each site, the batches submitted had to be part of a normative study or control group with explicit inclusion and exclusion criteria (Table C.1).
2. As mentioned before, the centralized processing team did not have access to the raw EEG data but rather only to the cross-spectra. Preliminary quality control for each sample consisted of visual inspection of a) the topographic map of  $y_i^\lambda(\omega)$  at representative frequencies and b) the  $y_i^\lambda(\omega)$  from 1.17 Hz to 19.14 Hz. At least two certified clinical neurophysiologists carried out independent evaluations to avoid subjectivity. The criterion for rejection of cases was overall extreme deformation from expected patterns. There was no attempt to enforce a "very typical pattern" such as the presence of an alpha peak since this may be absent in many normal subjects. Examples of accepted and rejected cross-spectra are shown in Fig. S.1, where (a) is an accepted sample (b) is a rejected sample, whose highest power was not at the occipital lobe. Additionally, the spectra are almost flat, indicating the prevalence of noise.
3. Once all batches were gathered, we conducted a machine-learning check for outliers. This centralized second stage quality control step is explained below in detail.

In qEEG research, as in all forms of data science, outliers are a problem that violates assumptions and can derail model estimation, comparison, and inference. Outliers are a common problem that can arise at any step in the whole qEEG pipeline due to: recording artifacts, mistakes in electrode ordering, missteps in data processing, and other factors.

In this study, we carry out outlier detection based on the distribution of DP z-scores  $z_{i,c,c'}^m(\omega)$ . We assumed that acceptable data conformed to a multivariate Gaussian distribution. We then leveraged the fact that the maximum likelihood covariance estimator (MLE) is sensitive to outliers and that effect spills over to the derived Mahalanobis Distance (MD). Iterative methods for robust MD (Leroy and Rousseeuw, 1987) calculate a corrected MD and make it easy to diagnose multivariate normality (Olive, 2004) and identify outliers samples. Specifically, before attempting the construction of harmonized norms, we detected and eliminated outlier subjects for  $y_{i,c,c'}^m(\omega)$ ,  $m = \{\lambda, \theta\}$  values separately. We first calculated each subject's  $z_{i,c,c'}^m(\omega)$  according to the model Eq. (8). We then create a data matrix where each subject is an observation ( $n = 1564$ ), measured on the  $\mathbf{z}_i^\lambda (P = N\omega Nc = 47 \times 18 = 846)$  and  $\mathbf{z}_i^\theta (P = N\omega Nc^2 = 47 \times 18^2 = 15288)$ .

Because of the small-n-large-P, we first carry out a nonlinear data mapping to a low dimensional component space using the t-distributed stochastic neighborhood embedding (t-SNE) (Van der Maaten and Hinton, 2008). This reduction allows us to compute both the Classical and Robust Mahalanobis distances (CMD, RMD) of each sample. We employ the robust estimates Minimum Covariance Determinant (FAST-MCD) method (Rousseeuw and Driessen, 1998) for the normative sample's mean and covariance matrix. It is then convenient to detect outliers from the D-D plot (Scatter plot of CMD versus RMD). In the absence of outliers, the data points cluster around the line  $y = x$ . By contrast, outliers deviate from this pattern with a practical threshold being  $\sqrt{\chi_{2,0.975}^2}$  the value of inverse chi-square cumulative distribution with two degrees of freedom for probability equal to 0.975

The results of this analysis are shown in Fig. 4 (dots indicate accepted samples, colored by study, and red crosses are outliers). We found that most data samples are closely grouped in the low dimensional space

for  $\mathbf{z}_i^\lambda$  and  $\mathbf{z}_i^\theta$  shown in Fig. 4-a and b separately, and the exceptions are some outlier points, as shown in Fig. 4-b. At the same time, we can numerically identify these outliers quickly by inspection of the D-D plot (Fig. 4-c and d). Non-outlier data points cluster tightly around the  $y = x$  line since their RMD and CMD should be similar. Outliers have a larger than expected RMD and CMD, as quantified by the Chi-square criteria (vertical and horizontal red lines of coordinate axes) (Fig. 4-c and d).

Centralized quality control was carried out iteratively, with feedback about each batch at each site. We detected mistakes in using the gatherer program or selecting the normative sample—evidenced by a complete batch consisting of outliers. An example of this type of error was a batch with the EEG channels ordered incorrectly—correction of this order eliminated the majority of outliers. With these types of errors corrected, the number of outliers diminished considerably.

As a consequence of this outlier detection step, we identified and eliminated 191 subjects from the samples used for the norm calculation of  $y_{i,c,c'}^\theta(\omega)$ , which reduced the final samples number to 1373. By contrast, there are no outliers for  $y_{i,c,c}^\lambda(\omega)$ .

#### 3.2. Choice of centering matrix

Fig. 5 presents the degrees of whitening achieved by different centering procedures, measured by half the Frobenius norm between the coherency matrices and the Identity matrix (Schott, 2005). Any type of centering is a highly significant improvement in spatial whitening. A frequency-specific centering, rather than an overall common one, performs better in delta, theta, and alpha bands, while a common centering operator has advantages in the beta band. These results are confirmed with a paired test ( $p = 0.05$ , with FDR to correct for multiple comparison correction with  $q = 0.05$  (Benjamini and Yekutieli, 2001)) with significant results shown as a black bar under the mean curves.

#### 3.3. Batch harmonization results

Section 2.4.3 suggests that qEEG norm models must include batch effects. It remains to see if this effect has practical consequences. A possible result of ignoring these batch effects is that  $z_{i,c,c'}^m(\omega)$  may not distribute as standard Gaussian variables. In this case, harmonizing samples of batch harmonized z-scores  $z_{i,c,c'}^{m*}(\omega)$  (obtained with Eq. (19)) should remedy this.

Indeed, Fig. 6-a compares the histograms of  $z_{i,Fp1,O2}^\theta(\omega)$  (Fig. 6-a) and  $z_{i,Fp1,O2}^{\theta*}(\omega)$  (Fig. 6-b) for the different batches. With the histogram of the  $z_{i,Fp1,O2}^\theta(\omega)$  for each batch, suggests they are not standard Gaussian. Note that this effect is not evident in the histogram of the aggregated global z scores pooling all batches (Fig. 6-c). The histograms for each batch are more closely gaussian for the harmonized  $z_{i,Fp1,O2}^{\theta*}(\omega)$  (Fig. 6-b), now in correspondence with the appearance of the aggregate for all batches Fig. 6-d.

The harmonization effect is also evident in the scatter plots of the  $z_{i,Fp1,O2}^\theta(\omega)$  as a function of frequency and age. There are slight but detectable deviations of the z-scores of each batch from a symmetric distribution around the zero plane (Fig. 6-e). However, for the  $z_{i,Fp1,O2}^{\theta*}(\omega)$ , these deviations are removed (Fig. 6-f). The corresponding results of  $z_{i,O2,O2}^\lambda(\omega)$  and  $z_{i,O2,O2}^{\lambda*}(\omega)$  are shown in Fig. S.2.

Additional insight about the effect of harmonization follows from the manifold learning method t-SNE. With all the subjects as observations, we project the  $\mathbf{z}_i^\theta$  to a common two-dimensional space and see that the data points form clusters, each corresponding to a different batch (Fig. 7-a). After harmonization, in the t-SNE plot for the  $\mathbf{z}_i^{\theta*}$ , these clusters disappear (Fig. 7-b). This batch correction effect also occurs for multivariate spectral measures. Clustering of  $\mathbf{z}_i^\lambda$  and their disappearance for  $\mathbf{z}_i^{\lambda*}$  are shown in Fig. S.3.

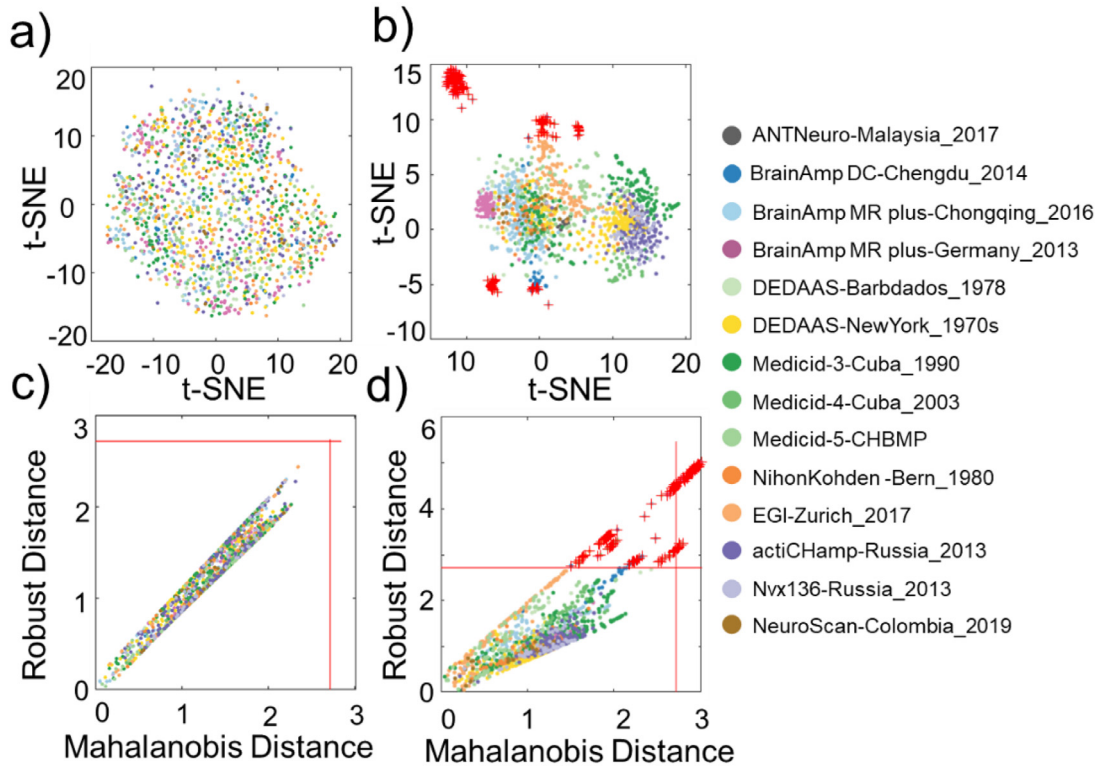


**Fig. 4.** Outlier detection for traditional log-spectrum and Riemannian z-scores. Each batch (study) is coded with a different color. Subplots (a) and (b) are two-dimensional representations of DPs via t-SNE, for traditional log-spectrum  $z_i^\lambda$  and Riemannian z-scores,  $z_i^0$ . Subplots (c) and (d) are the corresponding D-D (Robust-Mahalanobis distance versus Mahalanobis distance) plots with limits for outlier detection set at the conventional level, confirming the existence of outliers for Riemannian z-scores. Dots indicate accepted sample points and red crosses outliers. There are no outliers for  $z_i^\lambda$ .

**Table 6**

The effect of harmonization on the mean and SD of z-scores.

Metric	Null hypothesis rejected times for mean values (Proportion).		Null hypothesis rejected times for SD values (Proportion)	
	$p = 0.01$	$p = 0.05$	$p = 0.01$	$p = 0.05$
$z_{i,c,c}^\lambda(\omega)$	194(77%)	195(77%)	197(78%)	208(83%)
$z_{i,c,c}^{\lambda*}(\omega)$	0	0	0	0
$z_{i,c,c'}^0(\omega)$	3173(70%)	3232(71%)	3575(79%)	3614(80%)
$z_{i,c,c'}^{0*}(\omega)$	0	0	0	0

Furthermore, these graphical demonstrations of batch effect can also be confirmed by testing whether  $z_{i,c,c}^\lambda(\omega)$ ,  $z_{i,c,c}^{\lambda*}(\omega)$ ,  $z_{i,c,c'}^0(\omega)$ , and  $z_{i,c,c'}^{0*}(\omega)$  have mean 0, and variance 1—which would follow from these variables having a standard Gaussian distribution. We used MATLAB functions *ttest* for the mean and *vartest* for the variance, choosing significance levels of  $p = 0.01$  and  $p = 0.05$  for tests. Additionally, we used FDR correction for multiple comparisons with false discovery rate level  $q = 0.05$  (Benjamini and Hochberg, 1995). There are 252 ( $NbNc = 14 \times 18$ ,  $Nb$  is the number of batches) times test for  $z_{i,c,c}^\lambda(\omega)$ ,  $z_{i,c,c}^{\lambda*}(\omega)$  and 4536 ( $NbNc^2 = 14 \times 18^2$ ) times test for  $z_{i,c,c'}^0(\omega)$  and  $z_{i,c,c'}^{0*}(\omega)$  in total. Table 6 shows the null-hypotheses rejected proportion for four metrics. Before harmonization, there are batch effects that the z-scores of  $z_{i,c,c}^\lambda(\omega)$  and  $z_{i,c,c'}^0(\omega)$  are not standard Gaussian distribution for both  $p = 0.01$  and  $p = 0.05$ . After harmonization, the test statistic for  $z_{i,c,c}^{\lambda*}(\omega)$  and  $z_{i,c,c'}^{0*}(\omega)$  are never rejected, providing further assurance that batch effects are corrected.

### 3.4. The HarMNqEEG norms

To see how well the Riemannian norms approximate the classical norms, we first calculate the “surrogate” cross-spectral norms according

to Eq. (6) based on the norms in Section 2.4.3:

$$S_0(\omega, a) = \expm(\mathbf{C}^{-1/2}(\text{vech}^{-1}(\boldsymbol{\mu}^{\theta*}(\omega, a)))\mathbf{C}^{-1/2}) \quad (20)$$

We then obtain surrogates of the traditional norms from these cross-spectral norms,  $S_0(\omega, a)$ . The process is summarized in Table 7.

We first show in Fig. 8 examples of harmonized developmental surfaces for the diagonal elements Fp1, O1, and O2. Subplots a to c correspond to the measures  $\mu_{c,c}^{\lambda*}(\omega, a)$ ,  $\mu_{c,c}^{\theta*}(\omega, a)$ , and  $\mu_{0,c,c}^\lambda(\omega, a)$ . To be noted, Fig. 8-a (the detail in Fig. S.4) is similar to the developmental surfaces reported in Szava et al., (1994). Our current, more extensive, multinational dataset produces very similar results to the previous, smaller, single-country study (Szava et al., al.,1994). Fig. 8-b shows the surfaces of  $\mu_{c,c}^{\theta*}(\omega, a)$ (detailed in Fig. S.5), which are quite different from those in Fig. 8-a,  $\mu_{c,c}^{\lambda*}(\omega, a)$ . These differences are not surprising considering the highly nonlinear nature of the transformations involved in passing to the manifold tangent space—involving centering with the Riemannian geometric mean and a matrix-logarithmic transformation. Importantly, the consistency of the norm construction procedure is illustrated by the concordance between the traditional log-spectra  $\mu_{c,c}^{\lambda*}(\omega, a)$  (Fig. 8-a) and the surrogate log-spectra  $\mu_{0,c,c}^\lambda(\omega, a)$  (Fig. 8-c) confirming the results of Szava et al., (1994). Thus, when analyzing traditional log-spectral measures,  $\mu_{c,c}^{\lambda*}(\omega, a)$  we base our subsequent analyses on  $S_0(\omega, a)$ .

**Table 7**  
Surrogate traditional normative equations.

Variable	Name	Definition
$S_0(\omega, a)$	Surrogate cross-spectral norm	$\expm(C^{-1/2}(\text{vech}^{-1}(\mu^{\text{th}}(\omega, a)))C^{-1/2})$
$\mu_{0,c,c'}^{\lambda}(\omega, a)$	Surrogate log-spectral norm	$\log(S_{0,c,c'}(\omega, a))$
$\mu_{0,c,c'}^r(\omega, a)$	Surrogate coherence norm	$\left  \frac{s_{0,c,c'}(\omega, a)}{\sqrt{s_{0,c,c'}(\omega, a) \times s_{0,c',c'}(\omega, a)}} \right $
$\mu_{0,c,c'}^{\psi}(\omega, a)$	Surrogate phase norm	$\arctang\left[\frac{\text{Real}(s_{0,c,c'}(\omega, a))}{\text{Imag}(s_{0,c,c'}(\omega, a))}\right]$

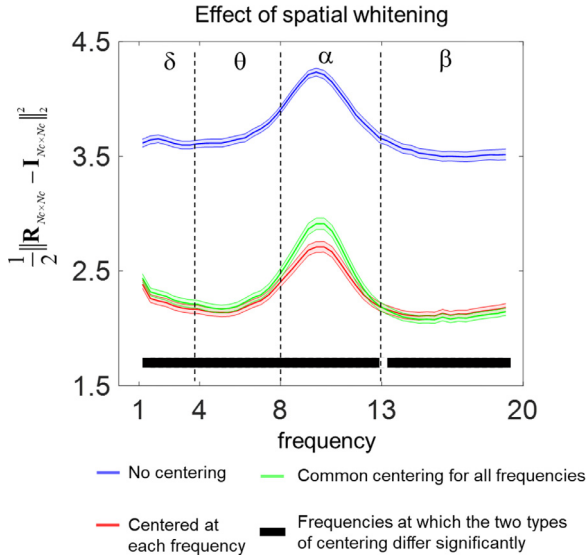


**Fig. 5.** Spatial whitening effect of several centering operations applied to the cross-spectral matrices. Solid thick lines represent the norms calculated across all subjects with the colored backgrounds delimiting the 0.01 confidence intervals). Shown are the means for no centering (blue), common centering for all frequencies (green), and centering separately at each frequency (red). The thick black bar below the curves marks the frequencies at which the two centering strategies are significantly different. A paired *t*-test determines these differences with a significance level  $p < 0.05$  corrected for multiple comparisons by an FDR with  $q = 0.05$ .

Fig. 9 provides a more detailed view of the surrogate log-spectral developmental surface already shown in Fig. 8-c. Fig. 9-a, shows the surface of  $\mu_{0,c,c'}^{\lambda}(\omega, a)$  for all frequencies at fixed younger ages (5, 15, 25, and 40). Fig. 9-b shows similar plots for older ages (45, 60, 80, and 95). Orthogonal view of  $\mu_{0,c,c'}^{\lambda}(\omega, a)$  are shown in Fig. 9-c, documenting changes with age at a few specific frequencies (2 Hz, 8 Hz, 10 Hz, 15 Hz)—the vertical lines on this figure mark 7, 16 and 50 years.

These plots of  $\mu_{0,c,c'}^{\lambda}(\omega, a)$  show that children have higher values than other ages at the lower frequency bands (delta and theta). By contrast, alpha activity increases in magnitude, and its peak moves towards higher frequencies. The alpha peak stabilizes around 25 years until around 40 years. After 40 years old, the alpha peak moves back towards lower magnitudes and frequencies, albeit slightly. For Fig. 9, detailed illustrations are in the supplement (Fig. S.6).

Next, we present the norms for the off-diagonal part  $c \neq c'$ , (Fp1,O1) or (O1,O2) with surrogate coherence and phase developmental surfaces. We show the same types of plots as in Figs. 8 and 9. The Figs. 10–12 show the developmental surface of surrogate coherence and surrogate phase. From Figs. 10-a and 11, we can see that the coherences  $\mu_{0,c,c'}^r(\omega, a)$  increase from early childhood to around 40 years and after 40 years slightly decrease until around 50, subsequently increasing again after 50. Coherences are maximal at around 10 Hz for all ages. Figs. 10-b and 12 show the surrogate phase's developmental surface and detailed information. With age, the phase increases from

childhood to age 20, later decreasing until 50, to increase afterward until 95 (Fig. 12-a to 12-b). The highest phases are at 10 Hz for all ages (Fig. 12-c). Here, to better express the range of phases, we show the results for channel pair (Fp1, O1),  $-\mu_{0,\text{Fp1},\text{O1}}^{\psi}(\omega, a) + \pi$  and  $-\mu_{0,\text{O1},\text{O2}}^{\psi}(\omega, a)$  for channel pair (O1, O2)

### 3.5. Validation of the HarMNqEEG norms for classification of schoolchildren who suffered malnutrition in the first year of life

To check the validity of our new harmonized qEEG norms, we revisited the problem of using the qEEG to classify school-children who suffered from Protein Energy Malnutrition (PEM) limited to the first year of life (BMal) and to distinguish them from healthy classmate controls (BCtrl), who were matched by age, sex, and handedness. Prior work is described in Bringas Vega et al. (2019), Taboada-Crispi et al. (2018). This work is part of the Barbados Nutrition Study— a project that is still ongoing for nearly half a century (Galler et al., 1983a, 1983b).

With the  $z_{i,c,c'}^{\lambda}(\omega)$ , we previously achieved excellent robust elastic-net discrimination between BCtrl and BMal. Those z-transforms were obtained using the CU1990 qEEG norms (Bosch-Bayard et al., 2020).

With the new tools developed in this paper, we gauge the effect on the discrimination between the two groups of three enhancements (a) Use of multinational instead of a national norm, (b) Use of  $y_{i,c,c'}^{\theta}(\omega)$  instead of  $y_{i,c,c'}^{\lambda}(\omega)$ , and c) Use harmonized multinational norms.

To answer these questions, we constructed several datasets as shown in the Venn diagram (Fig. 13-a):

- Barbados 1978 malnutrition (BMal) comprising  $N_i = 44$  samples;
- Barbados 1978 Control (BCtrl) comprising  $N_i = 62$  samples.
- In this case, the norms used to calculate z-scores were the complete HarMNqEEG dataset (MN) but excluding the Barbados controls (MN\BCtrl). This modification of the normative data set avoided validation bias.

After forming these sets and training tests, we processed two types of test DPs for the validation (Fig. 13-b). We carried out the following steps:

- Obtain the  $y_{i,c,c'}^{\theta}(\omega)$  of the groups BMal and BCtrl by using the geometric mean of MN\BCtrl when centering as in Eq. (4). Subsequently calculate  $y_{i,c,c'}^{\lambda}(\omega)$  of BMal and BCtrl.
- Estimate the normative mean  $\hat{\mu}_{c,c'}^m(\omega, a_i, \cdot, \cdot)$  and SD  $\hat{\sigma}_{c,c'}^m(\omega, a_i, \cdot, \cdot)$  with the dataset MN\BCtrl.
- Obtain the global z-scores  $z_{i,c,c'}^m(\omega)$  as in the formula (18).
- Obtain the batch harmonized z scores  $z_{i,c,c'}^{m*}(\omega)$  as in the formula (19).

To carry out the batch correction in the final step, and due to the lack of a larger sample of BCtrl, we plugged in the CU1990 random effect estimator. We base our choice of the CU1990 sample for the batch correction on the social, ethnic, and climatic similarity between Cuba and Barbados and prior studies that indicated that the Cuban norms describe the variability of the BCtrl group (Taboada-Crispi et al., 2018). Thus, we enter the statistical learning procedure with the following types of z-scores for BMal and BCtrl:

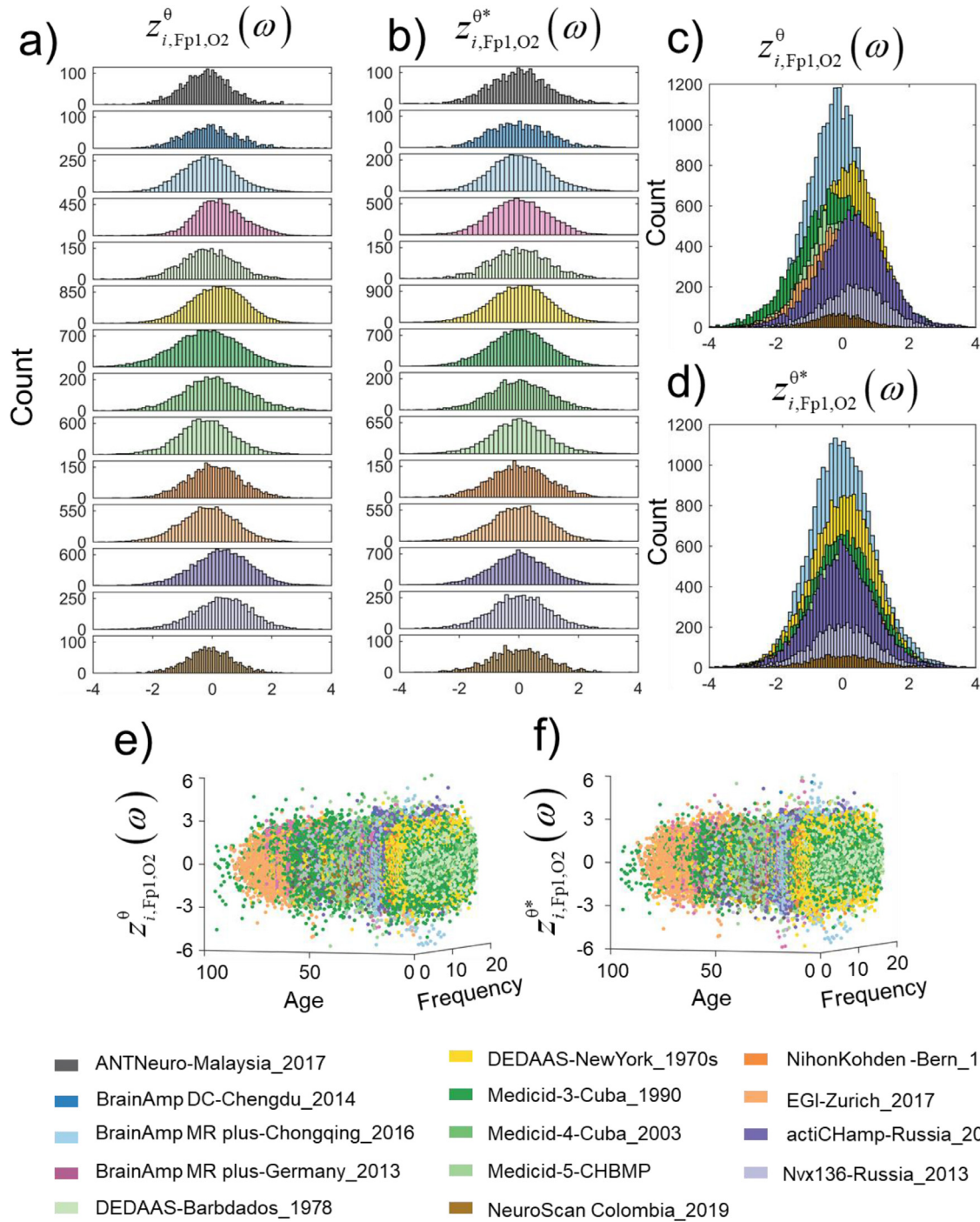


**Fig. 6.** Histograms and scatter plots for  $z_{i,Fp1,O2}^{\theta}(\omega)$  before and after harmonization. Each batch (study) is coded with a different color. (a) Histograms of z-score  $z_{i,Fp1,O2}^{\theta}(\omega)$  for each batch separately, and (c) for all batches superimposed; (b) Histograms of batch harmonized Riemannian DP z-score  $z_{i,Fp1,O2}^{\theta*}(\omega)$  for each batch separately, and (d) with all batches superimposed. (e) Scatter plot of  $z_{i,Fp1,O2}^{\theta}(\omega)$  as a function of frequency and age; (f) Scatter plot of  $z_{i,Fp1,O2}^{\theta*}(\omega)$  as a function of frequency and age, after harmonization.

Type of DPs	$y_{i,c,c'}^{\lambda}(\omega)$	$y_{i,c,c'}^{\theta}(\omega)$
qEEG norms	$z_{i,c,c'}^{\lambda}(\omega)$	$z_{i,c,c'}^{\theta}(\omega)$
HarMNqEEG norms	$z_{i,c,c'}^{\lambda*}(\omega)$	$z_{i,c,c'}^{\theta*}(\omega)$

We evaluate the discriminatory power of z-score types based on an elastic-net regression using the SSRC (Stable Sparse Robust Classifier) toolbox of Bosch-Bayard et al. (2018). The SSRC toolbox was previ-

ously used for this same dataset in Bringas Vega et al. (2019). SSRC uses multiple resampling to select a stable set of predictors and then (with additional independent resampling) to estimate the ROC curves for discrimination between both groups. We plot the ROC curve and report the Area under the ROC curve (AUC) for each type of z-score. Besides the AUC for the whole ROC curve, we also report the standardized partial AUC (spAUC) (McClish, 1989) for the discriminant scores

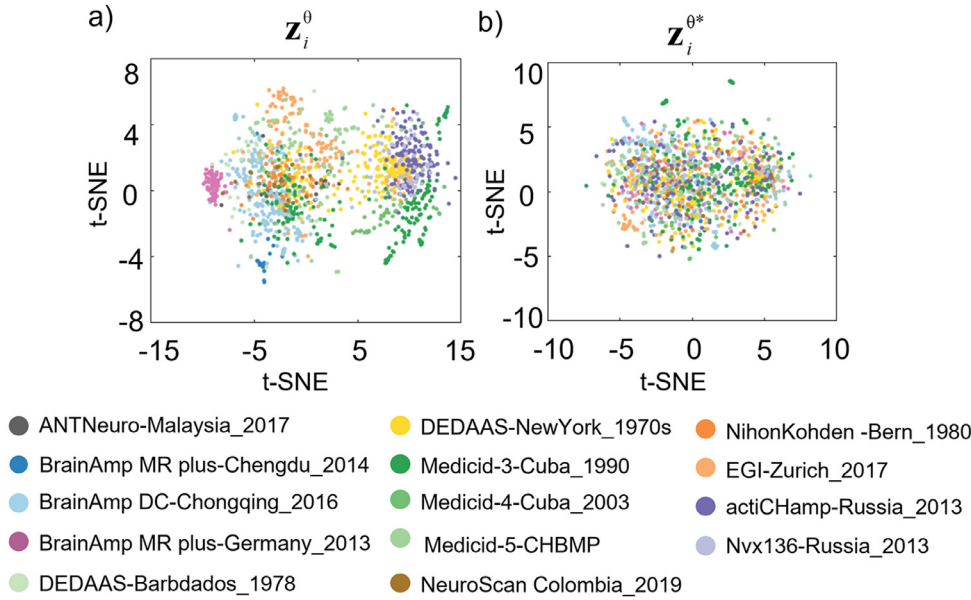


**Fig. 7.** Low dimensional scatter plots of Riemannian DP z-scores  $z_i^\theta$ , before and after harmonization. The low dimensional representation is a nonlinear mapping (via t-SNE) of z-scores of all Riemannian DPs onto two dimensions. Each axis is log-transformed. Points represent subjects, colored-coded by batch (study). (a) Low dimensional unharmonized  $z_i^\theta$  form clusters; (b) Low dimensional harmonized  $z_i^{\theta*}$  lack cluster structure.

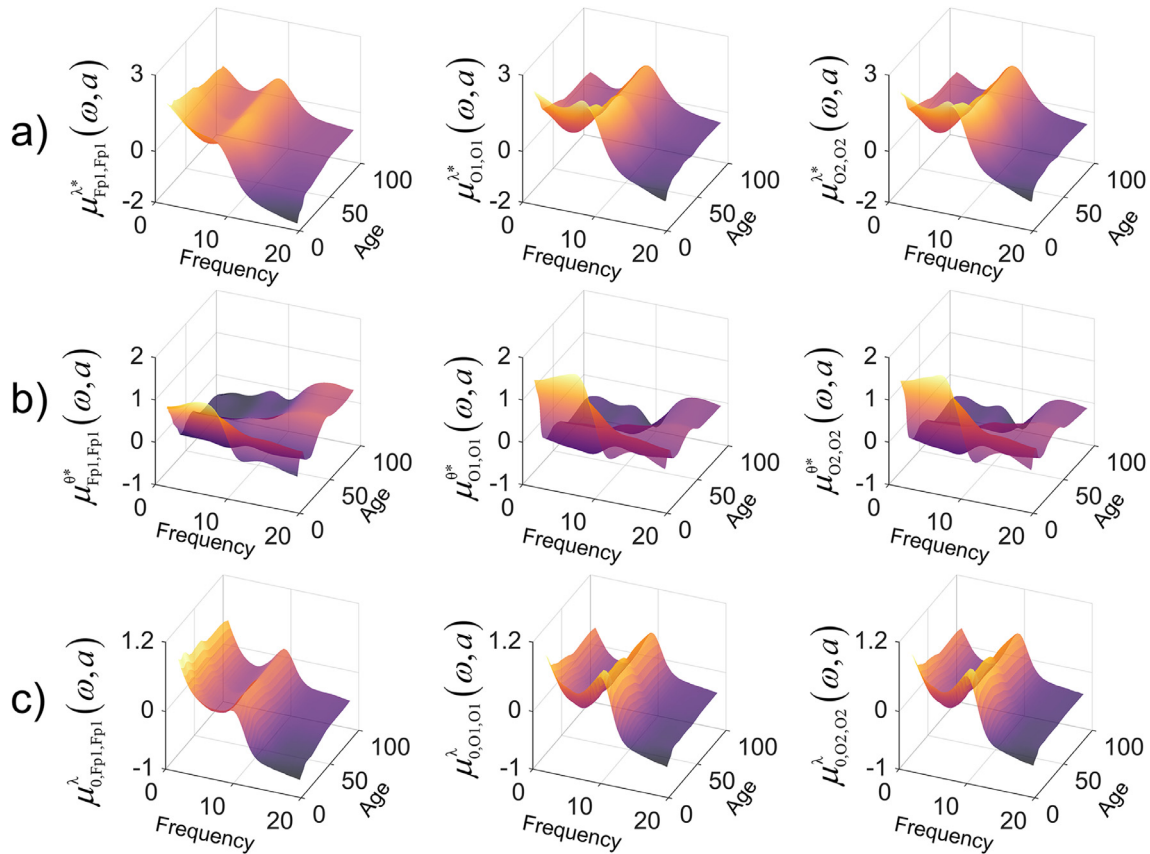


**Fig. 8.** Examples of harmonized normative means for channel pairs  $c = c'$  as a function of frequency and age. Normative means (Developmental surfaces) with examples  $c = c' = \text{Fp1}$  or  $\text{O1}$  or  $\text{O2}$ . (a) Traditional log-spectra  $\mu_{c,c}^{\lambda*}(\omega, a)$ ; (b) The Riemannian norm  $\mu_{c,c}^{\theta*}(\omega, a)$ ; (c) Surrogate log-spectrum norm  $\mu_{c,c}^{\lambda}(\omega, a)$ , reconstructed from the normative mean of  $\mathbf{S}_0(\omega, a)$ .

that produce 10% and 20% false positives rate (FPR). These partial AUC curves are of even greater interest in clinical settings, which usually require low false-positive rates. Accompanying these ROC curves are their probability distribution functions, also obtained via resampling with SSRC.

In Fig. 14, we first show the ROC curves of these four metrics (Fig. 14-a). Obviously,  $z_{i,c,c'}^\theta(\omega)$  and  $z_{i,c,c'}^{\theta*}(\omega)$  allow higher accuracy than  $z_{i,c,c}^\lambda(\omega)$  and  $z_{i,c,c}^{\lambda*}(\omega)$ . Harmonization boosts total accuracy from 0.829 to 0.870 when comparing  $z_{i,c,c}^\lambda(\omega)$  and  $z_{i,c,c}^{\lambda*}(\omega)$ . Likewise, there is an in-

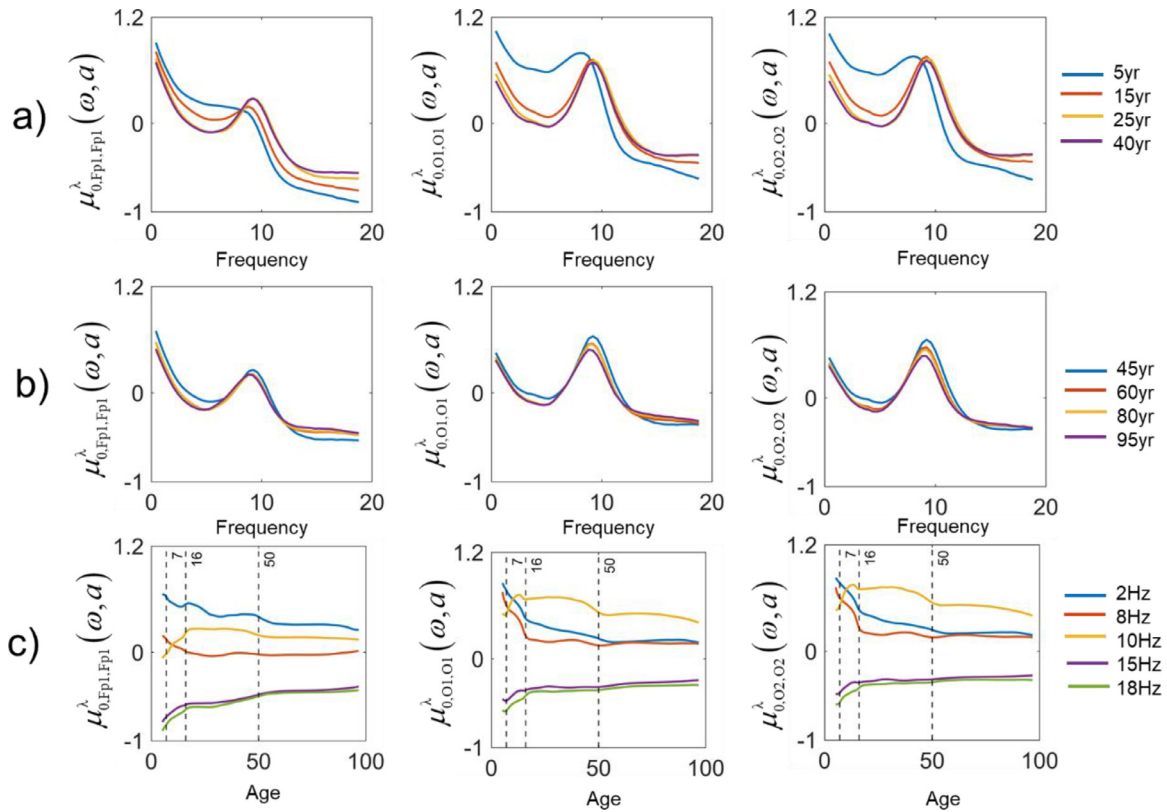


**Fig. 9.** Details of the surrogate log-spectral normative mean. The data in this figure are from the same normative means as in Fig. 8-c. The variation of the norm for fixed ages: (a) at younger ages (5 yr, 15 yr, 25 yr, and 40 yr), (b) at elder ages (45 yr, 60 yr, 80 yr, and 95 yr age). (c) Changes of the norm with age at specific frequencies (2 Hz, 8 Hz, 10 Hz, 15 Hz, with vertical lines at 7 yr, 16 yr, and 50 yr).

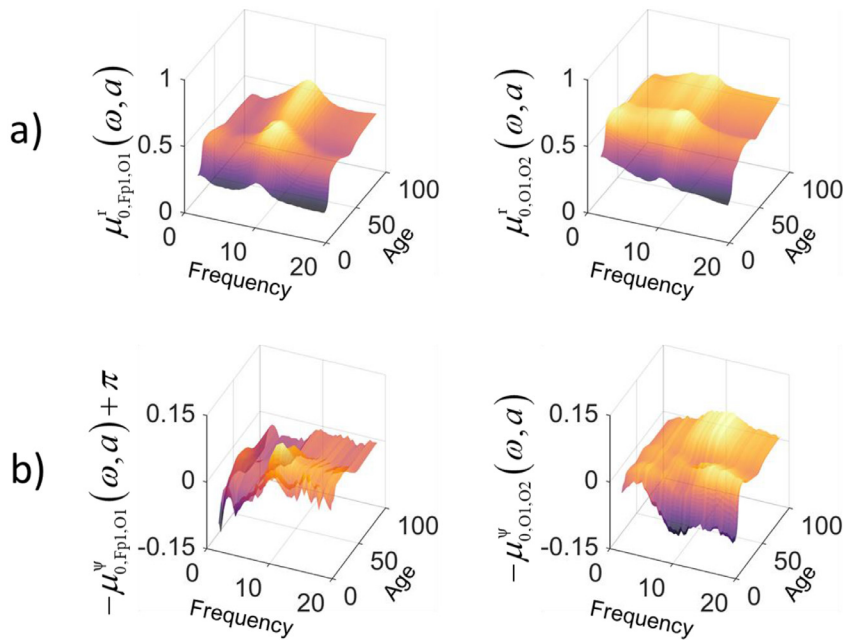


**Fig. 10.** Examples of surrogate coherence and phase normative means for (Fp1-O1) and (O1-O2). (a) Surrogate coherence normative mean for  $\mu_{0,c,c}^r(\omega, a)$ ; (b) Surrogate phase normative mean of  $-\mu_{0,c,c}^p(\omega, a) + \pi$  for (Fp1-O1) and  $-\mu_{0,c,c}^p(\omega, a)$  for (O1-O2).

crease from 0.943 to 0.952 when comparing  $z_{i,c,c'}^{\theta}(\omega)$  and  $z_{i,c,c'}^{\theta*}(\omega)$ . A valuable output of the SSRC toolbox is the probability density functions of the AUC and spAUC for the different measures. From Fig. 14-B, we see that the AUC of  $z_{i,c,c'}^{\theta*}(\omega)$  is significantly larger than that of  $z_{i,c,c'}^{\theta}(\omega)$ ,

indicating that harmonization is beneficial for accuracy. However, the ROC curves become very close for lower False Positive Rates (FPR). The spAUC at 20% FPR still shows a modest edge for harmonization. However, the situation reverses for even lower FPR (10%), with harmoniza-

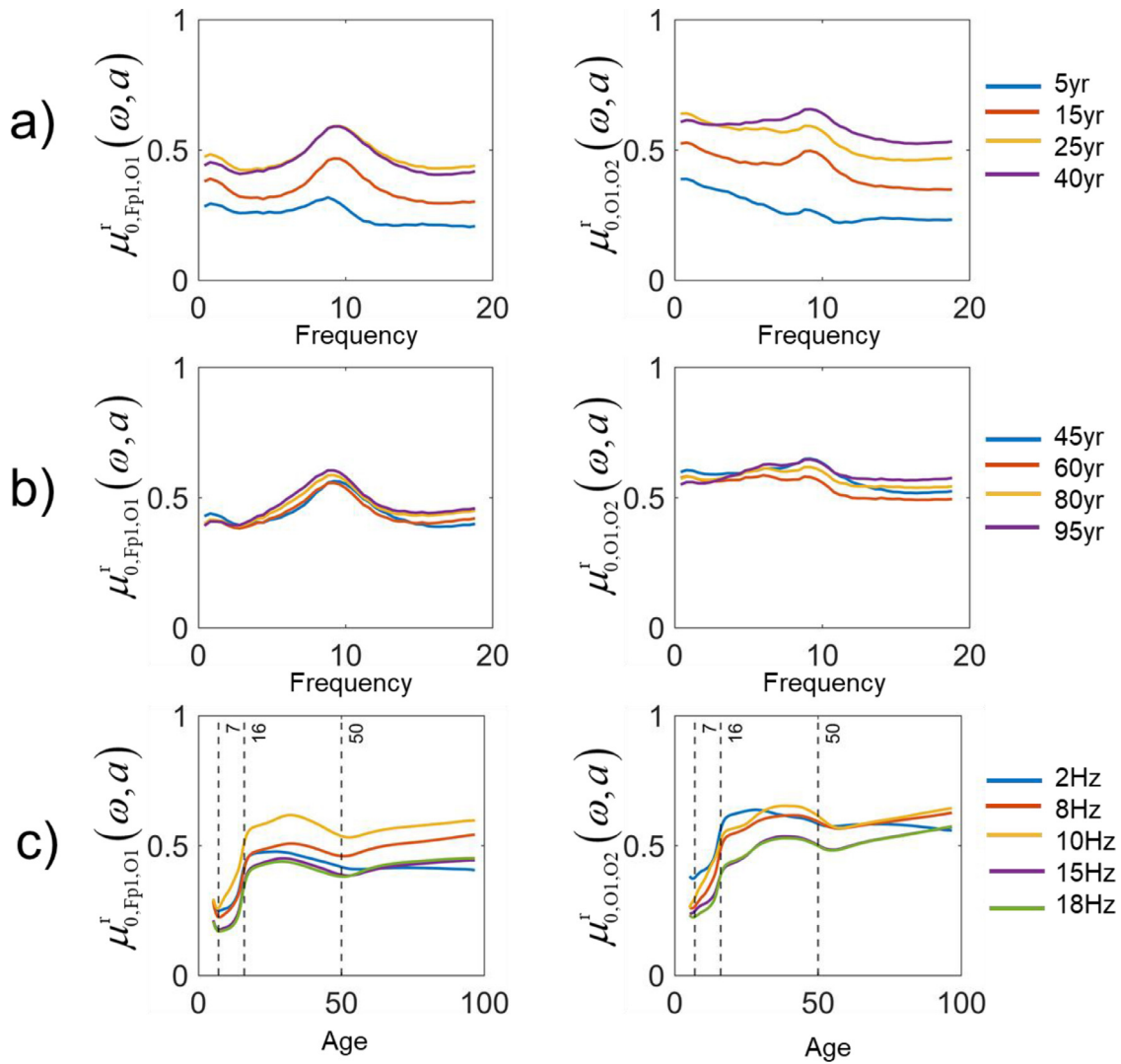


**Fig. 11.** Details of surrogate coherence  $\mu_{0,c,c'}^r(\omega, a)$  normative mean. The data in this figure are from the same normative means as in Fig. 10-a. The variation of the norm for fixed ages: (a) at younger ages (5 yr, 15 yr, 25 yr, and 40 yr), (b) at elder ages (45 yr, 60 yr, 80 yr, and 95 yr age). (c) Changes of the norm with age at specific frequencies (2 Hz, 8 Hz, 10 Hz, 15 Hz), with vertical lines at 7 yr, 16 yr, and 50 yr.

**Table 8**  
Standardized sparse AUC (spAUC) values of model validation.

Metric	$z_{i,c,c'}^\lambda(\omega)$	$z_{i,c,c'}^{\lambda*}(\omega)$	$z_{i,c,c'}^0(\omega)$	$z_{i,c,c'}^{0*}(\omega)$
FPR 10%	0.628	0.669	0.828	0.818
FPR 20%	0.704	0.750	0.877	0.884
FPR 100%	0.829	0.870	0.943	0.952

tion lowering the spAUC. Table 8 summarizes the AUC for the different measures compared under different FPRs.

Moreover, the higher accuracy for  $z_{i,c,c'}^0(\omega)$  and  $z_{i,c,c'}^{\lambda*}(\omega)$  are achieved with a much smaller number of features. As shown in Fig. 15, a and b the selected features of  $z_{i,c,c'}^\lambda(\omega)$  and  $z_{i,c,c'}^{\lambda*}(\omega)$  are grouped in four frequency bands (1–4 Hz, 4–8 Hz, 8–13 Hz, 13–20 Hz). There are more frontal and occipital electrodes involved in the classification, specifically F8 and O2. Fig. 14-c and 14-d show the selected features of  $z_{i,c,c'}^0(\omega)$  and  $z_{i,c,c'}^{0*}(\omega)$ , where the predominance of connections between frontal and occipital derivations is also evident, e.g., F8-O1. This type of combined

activity/connectivity figure might be useful for ulterior interpretation of the differences between groups.

### 3.6. Validation of the HarMNqEEG norms for classification of qEEG alternations in Covid induced brain dysfunctions

COVID-19 may cause long-term symptoms or conditions in people who either have been identified as potential carriers or have recovered from the infection. Valdés-Sosa et al. (2021) have coined the term “COVID Induced Brain Dysfunction” (CIBD) to refer to the

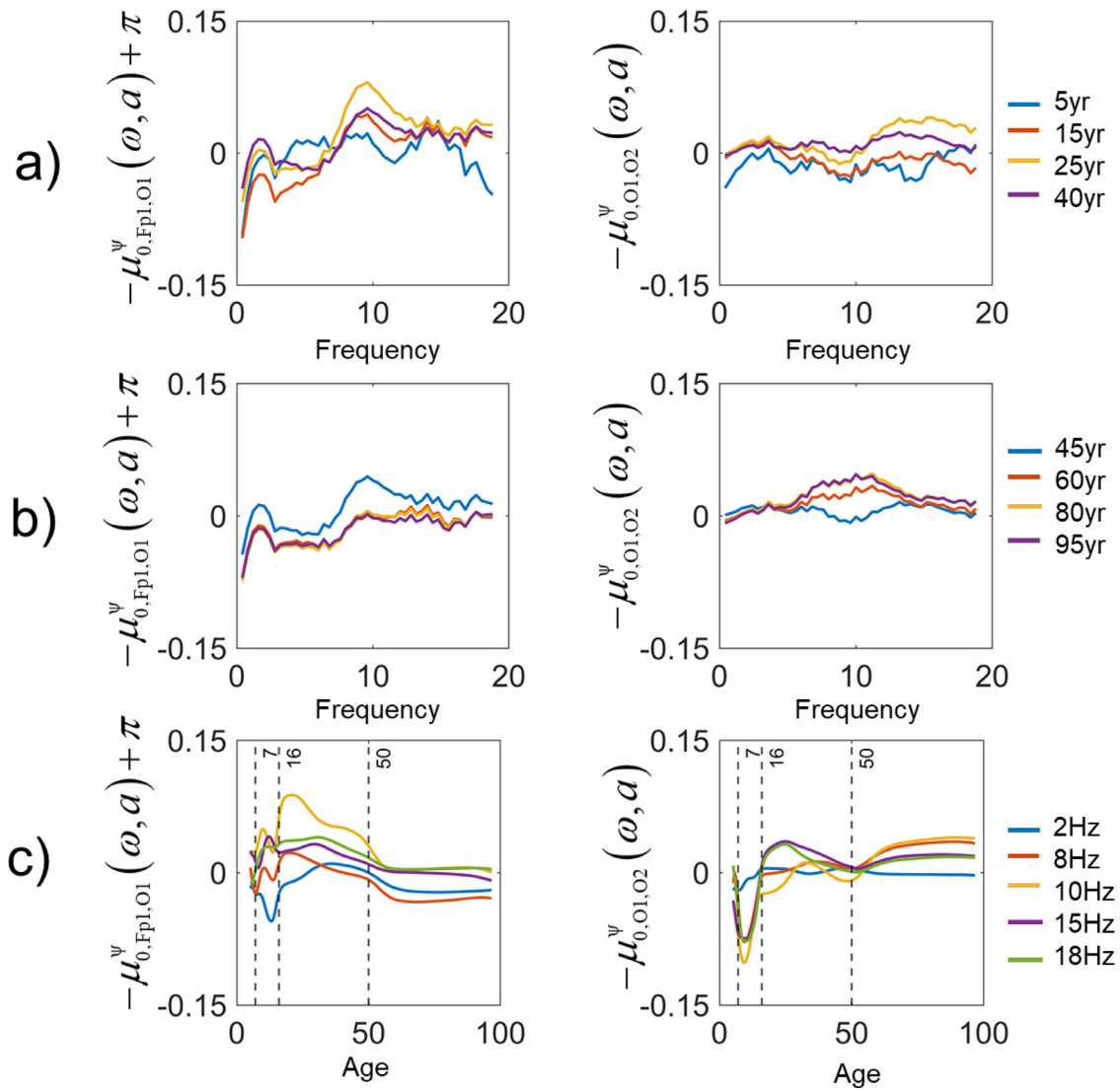


**Fig. 12.** Details of surrogate phase  $\mu_{0,c,c'}^{\psi}(\omega, a)$  normative mean. The data in this figure are from the same normative means as in Fig. 10-b. The variation of the norm for fixed ages: (a) at younger ages (5 yr, 15 yr, 25 yr, and 40 yr). (b) at elder ages (45 yr, 60 yr, 80 yr, and 95 yr age). (c) Changes of the norm with age at specific frequencies (2 Hz, 8 Hz, 10 Hz, 15 Hz), with vertical lines at 7 yr, 16 yr, and 50 yr.

processes due to social, psychological, or biological causes. In that paper, the need for objective evaluation of brain states for subjects with CIBD was called for. The search for such biomarkers in COVID-Induced Brain Dysfunction is another project of the Global Brain Consortium (<https://3design.github.io/GlobalBrainConsortium.org/projects.html#>).

We report the preliminary results of this project here. For this purpose, we take advantage of the Havana CIBD longitudinal project, which gathered the EEG after several months of PCR tests of two groups of participants: PCR positive patients and negative controls. The latter were recruited among the contacts confirmed for each patients. These two samples were relatively balanced for social and psychological factors, including stress and other social aspects, since during the first year of

the pandemic, all possible patients were provided free medical attention and isolation until a definitive diagnosis.

We apply the HarMNqEEG classification methods as described in the previous section. In this case instead of two groups we now have three groups: COVID positive patients, COVID negative subjects, recruited among the contacts of the patient and a sample of the EEG normative 1990 Cuban dataset. We present the Standardized sparse AUC (spAUC) values in Table 9.

The standardized sparse AUC values for the different groups are relatively large and improve for the Riemannian DPs. These classification results are quite high and are further confirmation of the validity of the norms. A complete description of this COVID study will be presented elsewhere.

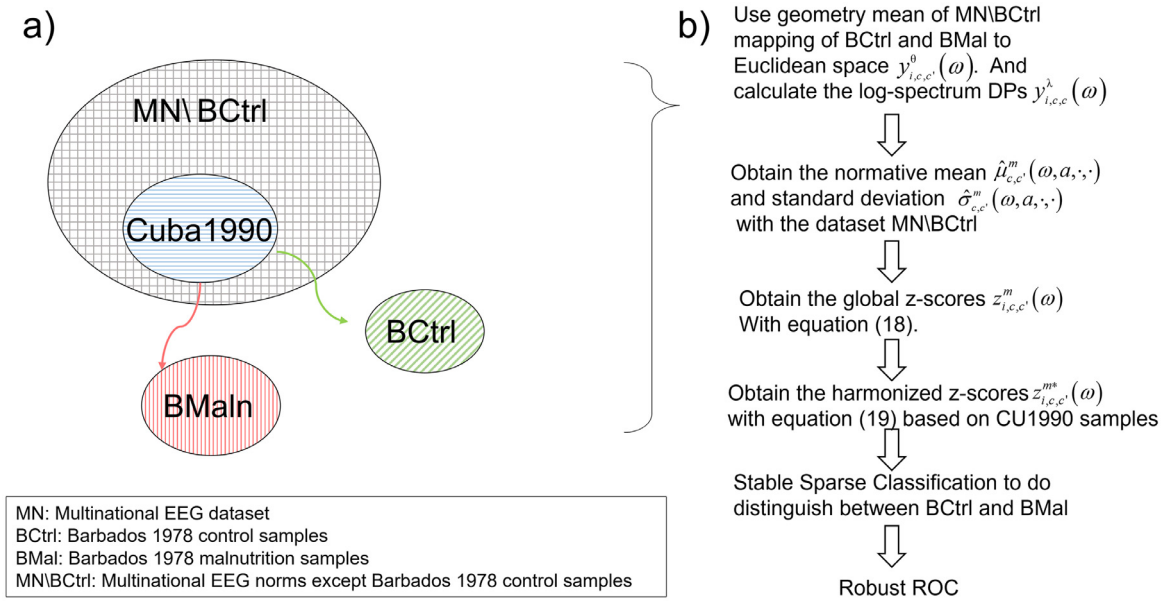


**Fig. 13.** Structure of training and test sets for evaluating the accuracy of different qEEG DPs to detect early protein-energy malnutrition. The different datasets are shown in a Venn diagram in (a). The normative dataset used to calculate the  $z_{i,c,c'}^m(\omega)$  is the complete Multinational Normative dataset, excluding the Barbados Controls (MN\BCtrl). Batch corrected  $z_{i,c,c'}^{ms}(\omega)$  are obtained using the batch information in the Cuba1990 study. The steps for the evaluation of diagnostic accuracy are outlined in (b).

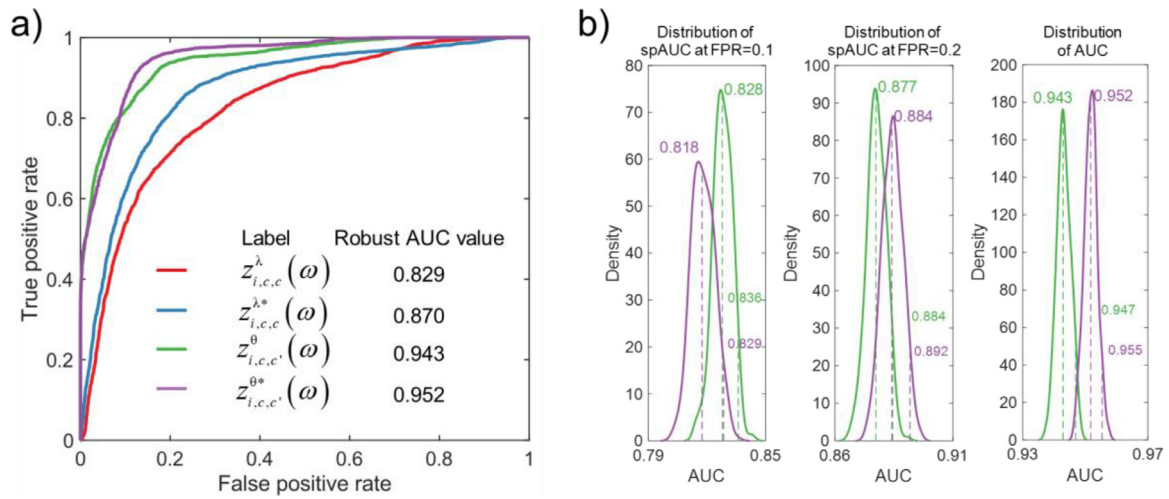


**Fig. 14.** Diagnosis accuracy in detecting early protein-energy malnutrition based on different types of qEEG DPs. Shown in subplot (a) Receiver Operator Curves (ROC) for discriminant functions to distinguish children with protein-energy malnutrition, based on four types of DPs: red  $z_{i,c,c'}^\lambda(\omega)$ , blue  $z_{i,c,c'}^{\lambda*}(\omega)$ , green  $z_{i,c,c'}^0(\omega)$ , and purple  $z_{i,c,c'}^{0*}(\omega)$ . The inset shows the robust Area under the ROC curve (AUC) for these types of DPs. In subplot (b), the distribution of spAUCs for Riemannian DPs, before and after harmonization. These are spAUC values for  $z_{i,c,c'}^\lambda(\omega)$  and  $z_{i,c,c'}^{0*}(\omega)$  at 10%, 20%, and 100% (full).

**Table 9**  
 Standardized sparse AUC (spAUC) values for multiple group classification.

Metric		$z_{i,c,c'}^\lambda(\omega)$	$z_{i,c,c'}^{\lambda*}(\omega)$	$z_{i,c,c'}^0(\omega)$	$z_{i,c,c'}^{0*}(\omega)$
Total	FPR 10%	0.85	0.85	0.92	0.95
	FPR 20%	0.61	0.64	0.75	0.79
	FPR 100%	0.68	0.69	0.80	0.87
Marginal (1-2)		0.82	0.84	0.96	0.95
Marginal (1-3)		0.90	0.90	1	0.99
Marginal (2-3)		0.63	0.64	0.77	0.81

1: group of normal samples (COVID-19\_B); 2: group of negative COVID-19 PCR test samples (COVID-19\_N); 3: group of positive COVID-19 PCR test samples (COVID-19\_P).

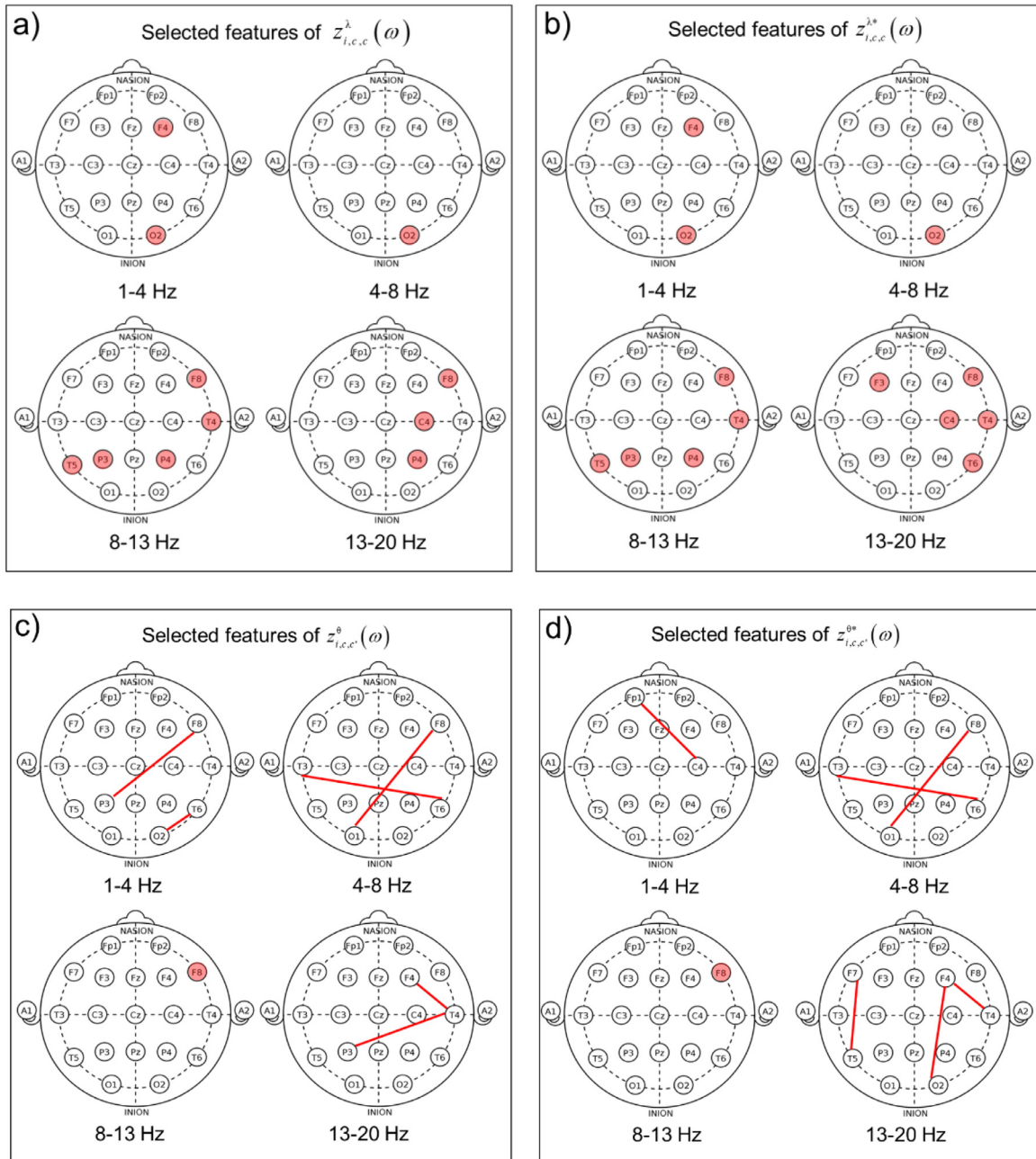


**Fig. 15.** Topography of features selected for detection of malnutrition based on different types of qEEG DPs. The features selected by the robust classifier are indicated in a plot of the 10/20 channel system. They are classified into the four traditional EEG frequency broad bands (though narrow bands). A red electrode indicates features related to a single channel. A red link between two electrodes indicates a feature selected for those two channels. a) Selected features for  $z_{i,c,c}^{\lambda}(\omega)$ ; b) Selected features for  $z_{i,c,c}^{\lambda*}(\omega)$ ; c) Selected features for  $z_{i,c,c}^{\theta}(\omega)$ ; d) Selected features for  $z_{i,c,c}^{\theta*}(\omega)$ .

#### 4. Discussion

This paper presents the HarMNqEEG project, an international qEEG normative collaboration intended to avoid racial and socioeconomic bias. It is one of the main projects of the Global Brain Consortium (<https://3design.github.io/GlobalBrainConsortium.org/project-norms.html>). The construction of unbiased qEEG norms and methods to quantify Brain Developmental Dysfunctions (BDD) is essential for providing easily accessible neuroimaging tools for use in public health settings worldwide. The model chosen for collecting data was offline processing at each site using the MATLAB program “data\_gatherer,” which produced batches of samples, each sample consisting of an EEG

cross-spectral tensor and anonymized meta-data. Thus, samples from different sites were guaranteed to be fully compatible, save for possible recording device and site variables. This compatibility was further enhanced by imposing a minimalistic set of recording requirements based on the IFCN 10/20 EEG recording montage and a limited range of EEG frequencies to analyze.

We decided to avoid sharing raw EEG data from recording sites. This choice facilitated the incorporation of diverse groups with varying ethical and administrative constraints. Data collection took less than 3 months to complete. It did, however, require intensive visual and numerical quality control at different stages of the processing pipeline. Other initiatives such as COINSTAC (Gazula et al., 2020) go to wholly

and fully decentralize processing, a vision that is the next logical step for our project. One of the thorniest problem of distributed processing is quality control. We are currently studying the outliers detected (in Section 3.1) in this sample to propose methods to avoid future occurrences.

Central processing of the cross-spectral tensors produced two sets of qEEG DPs. The traditional NB log-spectra was included for backward compatibility and comparison purposes. Importantly we introduce in this paper a new type of qEEG DPs based on Riemannian geometry. This development is essential since cross-spectral tensors occupy a highly nonlinear manifold. To this end, we define a Riemannian vectorization operator that transforms the cross-spectral tensor to a vector that closely follows a multivariate gaussian distribution in Euclidean space. An essential ingredient of the Riemannian vectorization is the matrix-logarithmic transform of the cross-spectral matrices. Leonard and Hsu (Leonard and Hsu, 2001) proposed this transformation to obtain an unconstrained multivariate gaussian vector from covariance matrices.

Recently, in a seminal series of papers, (Sabbagh et al., 2020; Engemann et al., 2021) showed the superiority of Riemannian DPs to predict brain age with MEEG/EEG. Our work differs from these previous applications in two essential aspects. The first is the use of Hermitian (not Real) Riemannian Geometry since the frontal faces of the cross-spectral tensor are cross-spectral matrices. A second difference is that rather than predicting age by the Riemannian DPs, we consider age as an independent variable to predict Riemannian DPs.

There has been no previous attempt to create developmental surfaces for the complete cross-spectral tensor. The added conceptual and computational machinery of Riemannian geometry seems to be beneficial. With this framework, we can now norm not only the frequency-resolved EEG activities at each channel (via the spectra) but also the functional connectivity between electrodes (reflected in the cross-spectra).

The multinational character of the datasets collected in the project allowed us a first look at qEEG harmonization. We believe the HarM-NqEEG project is one of the first efforts to check for “batch effects” in qEEG multisite datasets and propose computing subject z-scores from batch-free qEEG norms. This is the first attempt to create a statistically valid qEEG norm for cross-spectral tensors and their derived measures (coherence and phase).

Our work confirmed that a large part of the variance of traditional and Riemannian DPs depends on frequency and age, underscoring the need for frequency and age-dependent norms to detect BDD. This fixed-effect dependency has been reported many times for traditional log-spectra, including several papers from PAVS lab (Taboada-Crispi et al., 2018; Bosch-Bayard et al., 2001; Bringas Vega et al., 2019). Indeed, the shape of the norms or “developmental surfaces” for traditional measures hold up with the larger multinational sample. Based on Riemannian geometry, we confirm this frequency and age dependency for the full cross-spectrum. The reconstruction of traditional log-spectral norms from the Riemannian norms (surrogate norms) shows the consistency of the two procedures for the traditional DP set.

Regarding batch differences, note that using a global geometric mean to center cross-spectral tensors forces all data onto a unique normative tangent space. We studied whether batch or sex effects should be retained in the normative equations (Ko et al., 2021; Simeon et al., 2021). These models were compared using the Extended Bayesian Information Criterion. The recent study of Ko et al. (2021) describe sex difference in qEEG normative database, contrary to our study in which sex was pruned from the independent variables for fixed and random effects. This lack of sex-dependency requires further study, given the numerous neuroimaging studies for other modalities that also find such an effect.

On the other hand, batch effects, specifically site random effects, were evident. The modeling framework allowed the definition of batch-free z-scores. The need for this correction is particularly evident for Rie-

mannian DPs and easily observable in the t-SNE plots where harmonization eliminates batch differences.

The readers familiar with the construction of norms may be acquainted with COMBAT (Johnson et al., 2007) and generalized additive model for local scale and shape (GAMLSS) (Rigby and Stasinopoulos, 2005)—harmonization methods widespread to eliminate batch effects. Our model includes and generalizes both COMBAT and GAMLSS when the latter is restricted to Gaussian noise—which is our case. HarM-NqEEG allows multivariate nonparametric functional forms for the biological variables and the random additive effect (sex or batch) for mean and SD. Due to the Gaussianity of our DPs, we did not include models of higher-order statistics as in GAMLSS, but our models are more general for Gaussian data since our open source fkgreg code allows the mean and SD functions to be both complex-valued and multivariate, and the variance function can be log additive. Finally, compared with the generalized additive mixed-mode (GAMM) (Lin and Zhang, 1999), though the latter does allow multivariate functions, these are only for the mean. We emphasize that both COMBAT and GAMLSS models were tested in model selection and not retained due to having a higher nBIC/nEBIC.

We additionally provide evidence that Riemannian qEEG can provide higher diagnostic accuracy than traditional qEEG by evaluating the previously well studied Barbados Nutritional Study data set (Taboada-Crispi et al., 2018; Bringas Vega et al., 2019; Rutherford et al., 2021) and a COVID related EEG data set. We are currently exploring other clinical datasets with this approach.

The present study has several limitations:

It is essential to reduce the sources of heterogeneity in the EEG sample. However, we implemented their standard procedure to deal with heterogeneity by using a linear mixed model for DP sparameters.

An additional problem is that despite the substantial increase in sample size (compared to previous studies), it still may be underpowered to detect the effect of some biological variables such as gender. More importantly, the lack of combinations of types of equipment and country precludes separating the effect of these two variables. This issue needs to be the focus of further studies. Additionally, and as mentioned above, the age distribution of the sample is skewed towards younger ages. It is essential to remedy the lack of balance of the age distributions to improve the analysis of cognitive aging.

A normative study with denser electrode montages would also be desirable to improve localization accuracy, though the present study helps evaluate less intensive EEG examinations.

Artifact including eye blinks, movements, and scalp-muscle are strongly expressed in EEG, potentially influencing further analysis, especially for pathology diagnosis. In this project, we provide the instruction of each site for the artificial cleaning work. Additionally, the EEG preprocessing protocol also is a type of “batch effect” (can be grouped to “study”) which are non-biological variables. In the future, we will apply a standard EEG preprocessing pipeline supported by the GBC project.

There are several future directions of this work already being developed.

- We must extend the multinational Riemannian norms to source space as was already done for traditional qEEG (Bosch-Bayard et al., 2001; Bringas Vega et al., 2019)
- This source analysis would help resolve better different spatial patterns, which increase the heterogeneity of the normal patterns (Paz-Linares et al., 2018).
- We must also promote the creation of multinational norms for other sets of qEEG DPs such as microstates (Koenig et al., 2002)
- We must create and validate norms for multivariate Xi-Alpha models of the EEG cross-spectrum (Pascual-marqui et al., 1988; Hu and Valdes-Sosa, 2019; Tröndle et al., 2022).

The results presented in this paper contribute to developing bias-free low-cost neuroimaging technologies applicable in various health settings, especially those in low resource areas that are at the greatest risk for neurodevelopmental disabilities and other brain disorders (Galler et al., 2021).

All the code and data are openly available to calculate different individual z-scores from the HarMNqEEG dataset.

### Ethics statement

The studies involving human participants were reviewed and approved by the Ethics Committees of all involved institutions. In all cases, the participants and/or their legal guardians/next of kin provided written informed consent to participate in this study. All data were de-identified, and participants gave permission for their data to be shared as part of the informed consent process.

### Author contribution

The central processing team comprised: ML, who integrated methodological and software developments directed quality control and data Curation. Together with PAVS, she carried out the main contribution to paper writing. YW contributed to theoretical and software development methods for creating norms with kernel regression. He was also involved in data curation and contributed to writing, reviewing, and editing. PAVS conceived this line of research, stated the main methodological strategies, organized the Global Brain Consortium project, and carried out its administration (with ACE). He oversaw statistical analyses and conceived the paper's structure and all stages of writing. JFBB created, with PAVS, the traditional qEEG methods, wrote the gatherer program and supervised the curation of data supplied from all sites. He supervised theoretical developments and was responsible for statistical learning methods to check diagnostic accuracy. MLB was responsible for the conceptualization and organization of normative projects, the supervision of data collection, guarantee of essential resources. She also did writing and editing. CLN was responsible with ML and PAVS for developing the essential toolbox for Riemannian geometry. SH helped on the dataset collection. RCGR provided support on the Riemannian DPs part and helped to check the whole paper. DPL gave the support on paper reviewing. TK carried out the initial collation of datasets and continued involvement in the project. The following co-authors (in alphabetical order) contributed data, essential discussions, and paper editing: AIAH, ACE, ANS, ACR, AAG, AV, CATQ, DGA, DY, LD, EAV, FR, HO, JMA, JRG, JFOG, LSP, LGG, LMC, MJVS, MT, MFBMZ, MRBAR, NSM, NL, PR, TAVA, XL.

### Declaration of Competing Interest

The authors declare that they have no competing interests.

**Table A1**  
Summary of indices.

$i$	Index of individual $i \in \{1, 2, \dots, Ni\}$ .
$c$	Index of the channel $c \in \{1, 2, \dots, Nc\}$ , $Nc = 19$ including Fp1, Fp2, F3, F4, C3, C4, P3, P4, O1, O2, F7, F8, T3, T4, T5, T6, Fz, Cz, Pz electrodes.
$e$	Index of EEG epochs $e \in \{1, 2, \dots, Ne\}$ , the disjoint segments selected from the continuous EEG.
$\omega$	Discrete frequency $\omega = 1, \dots, N\omega$ . When multiplied by $\Delta\omega$ gives the physical frequency.
$a$	Age, which takes value from the subset of $\{a \in \mathbb{R}_+, \cdot\}$ . Then $a_i$ denotes the individual's age $i$ . The symbol " $\cdot$ " indicates all ages.
$s$	Sex, which takes value from the subset of $\{\text{Male, Female,}\cdot\}$ . Then $s_i$ indicates the sex of the individual $i$ . The symbol " $\cdot$ " indicates all sex.
$b$	Batch, where $b_i$ means batch of individual $i$ , the symbol " $\cdot$ " indicates all batches and $Nb$ is the number of batches.
$t$	Time $t = 1, \dots, Nt$ . Physical time is obtained by multiplication with $\Delta t$

### Acknowledgement

The research was funded by grants (to PAVS) from the National Project for Neurotechnology of the Ministry of Science Technology and Environment of Cuba, the National Nature Science Foundation of China NSFC Grant No. 61871105, CNS Program of UESTC (No. Y0301902610100201) and (to MLBV and PAVS) from the Nestlé Foundation (Validation of a long-life neural fingerprint of early malnutrition, 2017). The National Science Foundation of China (to SH) Grant with No. 62101003. ACE and JBB were supported by: Brain Canada (243030 and 256327); CANARIE Inc (252749); Ludmer Funding (249926); Canada First Research Excellence Fund (CFREF)/HBHL Intl.Collab.Plat (252427); the (CFREF)/HBHL Big Brain Analytics, and Learning Laboratory (HIBALL), and Helmholtz (252428); and the Fonds de Recherche du Québec FRQ/Canada-Cuba-China Axis (246117). The team of Malaysia was funded from the Translational Research Grant Scheme, Ministry of Higher Education (TRGS/1/2015/USM/01/6/3) and the Research University Grant (RUI), Universiti Sains Malaysia (1001/PPSP/8012307). The dataset from Russia was collected with the support of the Russian Foundation of Basic Research, grant No. 18–29–13027. The Barbados dataset was funded by the Grants R01 HD060986 (JRG).

### Data and code available

The shared raw cross-spectra with encrypted ID is hosted at Synapse.org (10.7303/syn26712693) and complete access is possible after login in the system. The multinational harmonized norms (HarMNqEEG norms) of traditional log-spectra and Riemannian cross-spectra are hosted at Synapse.org (10.7303/syn26712979). Additionally, the corresponding HarMNqEEG code for calculating the z-scores based on the HarMNqEEG norm opened in GitHub, see: <https://github.com/LMNonlinear/HarMNqEEG>.

### Supplementary materials

Supplementary material associated with this article can be found, in the online version, at doi:10.1016/j.neuroimage.2022.119190.

### Appendix A. Description of cross-spectrum as a tensor

#### A.1. Summary of indices

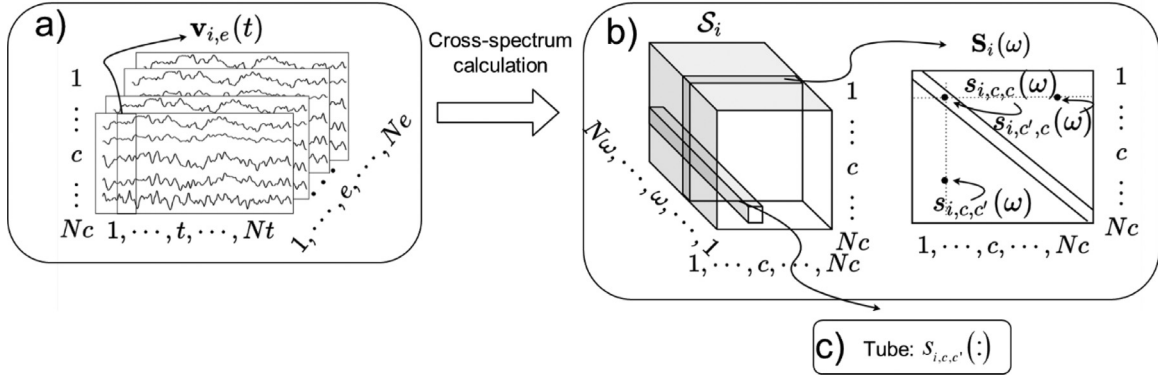


**Fig. A1.** The construction of cross-spectrum. (a) Frequency domain DPs result from processing multi-channel EEG data  $\mathbf{v}_{i,e}(t)$  epochs (individual  $i$ , time  $t$ ,  $e$ -th epoch). (b) The cross-spectral matrices  $\mathbf{S}_i(\omega)$  are the covariance matrices of the Fourier transform of the  $\mathbf{v}_{i,e}(t)$ . These  $\mathbf{S}_i(\omega)$  are the frontal slices of the tensor  $\mathbf{S}_i$ ; (c) Besides columns and rows, the tensor has tubes  $s_{i,c,c'}(\omega)$  which are the set of elements for two fixed channels and all frequencies.

## A.2. Technical notes about the EEG Cross-spectrum and its tensor representation

The multi-channel EEG  $\mathbf{v}_{i,e}(t)$  (Figure A1-a) is a vector time series recorded for the participant  $i$ , at the time  $t$ , for the  $e$ -th epoch, where,  $i = 1, \dots, Ni$  ( $Ni$  is the number of subjects),  $e = 1, \dots, Ne$  ( $Ne$  is the number of epochs which is an uninterrupted fixed-length sequence of time points).  $t = 1, \dots, Nt$  ( $Nt$  is the number of time points in each epoch). Note that  $t$  is an integer index. When referring to actual time (in seconds or milliseconds),  $t$  is multiplied by  $\Delta t$ , and this conversion ( $\Delta t \cdot t$ ) allows physiological interpretation.

The vector  $\mathbf{v}_{i,e}(t)$  has, as components, the set of scalar potentials  $v_{i,e,c}(t)$ , measured with the same (unipolar) reference, for each channel  $c$ , where  $c = 1, \dots, Nc$  ( $Nc$  is the number of channels). To streamline our presentation, we indistinctively use the channel number of a particular montage or its channel label.

Each EEG segment  $v_{i,e,c}(t)$  is transformed to the frequency domain via the (discrete) Fourier transform to yield the complex-valued coefficients  $v_{i,e,c}(\omega)$ , where the symbol  $\omega$  denotes frequency. The multiplication with frequency resolution  $\Delta\omega$  refers to actual frequency  $\omega = \Delta\omega, \dots, N\omega\Delta\omega$  (in Hz) ( $N\omega$  is the number of the frequencies sampled). Careful selection of epochs ensures that a) they are approximately stationary and b) lack long-range memory correlations in time. The Fourier coefficients are then asymptotically (as  $Nt \rightarrow \infty$ ) independent for each frequency and sampled from a Circular Multivariate Complex distribution  $N_{Nc}^{(C)}(\mathbf{0}, \mathbf{\Sigma}_i(\omega))$  with mean 0 and population covariance  $\mathbf{\Sigma}_i(\omega)$  (different for each participant  $i$ ). (Chapter. 4.3, Brillinger, 1981). The set  $\{\mathbf{\Sigma}_i(\omega)\}, \omega = 1, \dots, N\omega$  is the “cross-spectrum,” which is the basis for our frequency domain DPs. The cross-spectra encodes the linear and stationary properties of the EEG. It is important to note that the  $\mathbf{\Sigma}_i(\omega)$  are not symmetric as in the real case but Hermitian.

Since the  $\mathbf{\Sigma}_i(\omega)$  are unobservable population quantities, we must use the maximum-likelihood estimate, the covariance matrix  $\mathbf{S}_i(\omega)$  of the complex-valued coefficients of the Fourier transform, pooled over all epochs. We assemble these sample covariances  $\mathbf{S}_i(\omega), \omega = 1, \dots, N\omega$  into a cross-spectral tensor  $\mathbf{S}_i$ <sup>6</sup> 3-mode dimensional array with dimensions  $Nc \times Nc \times N\omega$ . The language of tensor has been used to great advantage in our prior work (Karahan et al., 2015; Martínez-Montes et al., 2004; Miwakeichi et al., 2004), and this section provides a bridge that line of work that includes source localization.

In the parlance of tensors, fixing two of the dimensions and varying over the others produces “fibers”. Channels correspond to “column”

and “row” fibers and frequencies to “tube” fibers. Also, in tensor terminology, “frontal slices” are just the usual cross-spectral matrices  $\mathbf{S}_i(\omega)$ . The tube fibers correspond to the “spectra” of time-series analysis. Let  $s_{i,c,c'}(\omega)$  denote the individual elements of  $\mathbf{S}_i(\omega)$  (Fig. A1-b), where  $c$  and  $c'$  denote channels  $c, c' = 1, \dots, Nc$ . Then we have two types of fibers  $s_{i,c,c'}(\omega) = \{s_{i,c,c'}(\omega), \omega = 1, \dots, N\omega\}$  (Figure A1-c):

- When  $c = c'$  the fiber  $s_{i,c,c}(\omega)$  sits on a diagonal element of the cross-spectral matrices over all frequencies, it is a real scalar tube known as the power-spectrum for the channel  $c$ . We shall refer to this type of tube or its element as “diagonal”.
- When  $c \neq c'$  the fiber  $s_{i,c,c'}(\omega)$  sits on an off-diagonal element of the cross-spectral matrices over all frequencies, this complex-valued tube is the cross-spectrum between channels  $c$  and  $c'$ . We refer to this type of tube or its elements as “off-diagonal”.
- Instead of the usual property  $s_{i,c,c'}(\omega) = s_{i,c',c}(\omega)$  (valid only for real covariance matrices), we now have for the Hermitian case  $s_{i,c,c'}(\omega) = \text{conj}(s_{i,c',c}(\omega))$ : symmetric elements are complex conjugates of each other

## Appendix B. Notes of Riemannian vectorization

### B.1. The technical notes of Riemannian geometric mean

The Riemannian metric is defined locally as the inner product on tangent space,

$$\langle \mathbf{Q}_1, \mathbf{Q}_2 \rangle_{\mathbf{A}} = \text{Tr}(\mathbf{Q}_1 \mathbf{A}^{-1} \mathbf{Q}_2 \mathbf{A}^{-1})$$

Where,  $\mathbf{Q}_1, \mathbf{Q}_2$  are vectors at tangent space at  $\mathbf{A}$ . The manifold  $\mathbb{P}_n$  is a complete Riemannian manifold with negative curvature with a metric. The geodesic between two PD matrices points is unique, and its length (distance) has an analytic expression,

$$\delta(\mathbf{A}, \mathbf{B}) := \|\text{Log}_{\mathbf{B}}(\mathbf{A})\|_F = \|\log(\mathbf{B}^{-1/2} \mathbf{A} \mathbf{B}^{-1/2})\|_F$$

This expression defines the affine-invariant metric, which gives the most reasonable geodesic distance on PD (Yger et al., 2017) based on differential geometric information-theoretical arguments. Thus, the geometric mean of the set of PD matrices  $\mathbf{A}_k, k = 1, \dots, K$  can be defined as the center of mass, which is the unique solution of,

$$G(\mathbf{C}) = \sum_{k=1}^K \delta^2(\mathbf{A}_k, \mathbf{C}) \quad (\text{B1})$$

It has been proved by Moakher (2005) that the center mass is the unique PD solution of the nonlinear function,

$$\sum_{k=1}^K \log(\mathbf{A}_k^{-1} \mathbf{C}) = \sum_{k=1}^K \log(\mathbf{C} \mathbf{A}_k^{-1}) = \sum_{k=1}^K \log(\mathbf{C}^{1/2} \mathbf{A}_k^{-1} \mathbf{C}^{1/2}) = 0 \quad (\text{B2})$$

<sup>6</sup> The rank of the tensor is usually based on the canonical polyadic decomposition or PARAFAC (Miwakeichi et al., 2004). The rank of the cross-spectral tensors in this study depended on the data, ranging from 5 to 16 for our sample.

When  $K = 2$  the solution of (B1) is  $\mathbf{C} = \mathbf{A}_1(\mathbf{A}_1^{-1}\mathbf{A}_2)^{1/2}$ , for  $K \geq 3$ , the explicit expression is unknown, and an iterative estimation algorithm is available (Karcher, 1977; Bhatia, 2013; Congedo et al., 2017). Here use the method based on the paper of Bini and Iannazzo (2013), the gradient descent algorithm of Eq. (B2) is written as,

$$\mathbf{C}_{i+1} = \mathbf{C}_i \exp\left(-\vartheta_i \sum_{k=1}^K \log(\mathbf{A}_k^{-1} \mathbf{C}_i)\right), \mathbf{C}_0 \in (\mathbb{P})_n \quad (\text{B3})$$

With  $\mathbf{C}_0 = \mathbf{A}_1$ , or  $\mathbf{C}_0 = \mathbf{I}$ . The iteration with choice  $\vartheta_i = 1/K$  has been discussed (Manton, 2004; Pennec et al., 2006). Bini and Iannazzo (2013) provide an optimal value for  $\vartheta$  and linearize Eq. (B3) which is Richardson iteration, denoted as

$$\mathbf{C}_{i+1} = \mathbf{C}_i - \vartheta \mathbf{C}_i \sum_{k=1}^K \log(\mathbf{A}_k^{-1} \mathbf{C}_i) \quad (\text{B4})$$

The Eq. (B2) solution is the fixed point of Eq. (B4). Thus, the Eq. (B4) could be written as,

$$\mathbf{C}_{i+1} = \mathbf{C}_i - \vartheta \mathbf{C}_i^{1/2} \sum_{k=1}^K \log(\mathbf{C}_i^{1/2} \mathbf{A}_k^{-1} \mathbf{C}_i^{1/2}) \mathbf{C}_i^{1/2}$$

That all iterations are positive. It proved that the small enough  $\vartheta$  guarantee the local convergence and when  $\vartheta_i = 1/K$ , the pairwise com-

mute matrices  $\mathbf{C}_0, \mathbf{A}_1, \dots, \mathbf{A}_K$  at least globally quadratic convergence (Bini and Iannazzo, 2013).

## B.2. Centering is a linear operator

It is well known (Chapter 3, Brillinger, 1981) that transforming a multivariate autocovariance matrix to the frequency domain produces a block-diagonal covariance matrix with the cross-spectra for each frequency on the main diagonal. That is:

$$\text{Cov}(\mathbf{x}(\omega_1), \mathbf{x}(\omega_2)) = \begin{cases} \boldsymbol{\Sigma}_{\mathbf{xx}}(\omega) & \omega_1 = \omega_2 \\ \mathbf{0} & \omega_1 \neq \omega_2 \end{cases}$$

This property induces an isomorphism between the tensors  $\mathcal{S}$  and the cross-frequency block-diagonal covariance matrix  $\text{diag}(\boldsymbol{\Sigma}_{\mathbf{xx}}(\Delta\omega), \dots, \boldsymbol{\Sigma}_{\mathbf{xx}}(N\omega\Delta\omega)) = \boldsymbol{\Sigma}^B$ . Given this isomorphism between the two manifolds  $\mathcal{S}$  and  $\boldsymbol{\Sigma}^B$ , the centering operation applied separately to each frequency can also be defined in the space of block-diagonal matrices as  $\mathbf{C}^B = \text{diag}(\mathbf{C}(\Delta\omega), \dots, \mathbf{C}(N\omega\Delta\omega))$ . Thus, the centering operation in the block diagonal space is  $(\mathbf{C}^B)^{-1/2} \boldsymbol{\Sigma}^B (\mathbf{C}^B)^{-1/2}$ . It can be easily seen the centering operation in both representations is invertible and linear.

## Appendix C. Multinational EEG norms dataset

**Table C1**

Multi-national EEG norms dataset: including 9 countries, 12 devices and 14 batches.

Country	Dataset sites	N individuals (Female; Male)	Age range	Device	Reference	Year recorded	Citation
Barbados 62 (F28; M34)	Barbados_1978	62 (F28; M34)	5.5–11.4	DEDAAS	Linked Ears	1978	(Bringas Vega et al., 2019; Taboada-Crispi et al., 2018)
China 268 (F141; M127)	Chengdu_2014	33 (F7; M26)	21–28	BrainAmp DC	REST	2014	(Li et al., 2015)
	Chongqing_2016	235 (F134; M101)	15–26	BrainAmp MR plus	common	2016–2019	(Duan et al., 2021)
Colombia 21 (F13; M8)	Colombia_2019	21 (F13; M8)	22–45	Neuro scan	average	2019	<a href="https://alz.confex.com/alz/20amsterdam/meetingapp.cgi/Paper/47837">https://alz.confex.com/alz/20amsterdam/meetingapp.cgi/Paper/47837</a>
Cuba 367 (F153; M214)	Cuba_1990	195 (F98; M97)	5.5–97	Medicid-3M	common	1990	(Bosch-Bayard et al., 2020)
	Cuba_2003	48 (F28; M20)	5–69	Medicid-4	common	2003	(Hernandez-Gonzalez et al., 2011)
	CHBMP	124 (F27; M97)	17–62	Medicid-5	Linked Ears	2004–2008	(Valdes-Sosa et al., 2021)
Germany 178 (F113; M65)	Germany_2013	178 (F113; M65)	22.5–77.5	BrainAmp MR plus	common	2013	(Babayan et al., 2019)
Malaysia 26 (F24; M2)	Malaysia_2017	26 (F24; M2)	19–60	ANT Neuro	average	2017/2020	–
Russia203 (F104; M99))	Russia_2013	58 (F34; M24)	18–49	nvx136	Cz	2013/2019	(Ivanov et al., 2022)
		145 (F70; M75)	16–57	actiCHamp	Cz	2013/2019	
Switzerland209 (F98; M111)	Bern_1980	44 (F18;26)	10–16	Nihon Kohden	common	1980	(Koenig et al., 2002);
	Zurich_2017	165 (F80; M85)	18–90	EGI-256 HCGSN	average	2012/2017–2019	(Langer et al., 2013)
USA230 (F109; M121)	New York_1970s	230 (F109; M121)	6–80.5	DEDAAS	common	1970s-1980s	(Ahn et al., 1980)
Total		1564 (F783; M781)					

**Appendix D. Batch definition**

**Table D1**

Batch is defined by country, device and the recording year of data (study).

Device Country	BrainAmp MR plus	BrainAmp DC	actiCHamp	DEDAAS	EGI-256 HCGSN	Medicid-3M	Medicid-4	Medicid-5	Nihon Kohden	nvx136	ANT Neuro	Neuro scan
Barbados				DEDAAS- Barbdados_ 1978								
China	BrainAmp MR plus- Chongqing_ 2016	BrainAmp DC- Chengdu_ 2014										
Cuba						Medicid-3M- Cuba_1990	Medicid-4- Cuba_2003	Medicid-5- 5-CHBMP				
Colombia												NeuroScan- Colombia_ 2019
Malaysia												ANTNeuro- Malaysia_ 2017
Germany	BrainAmp MR plus- Germany_ 2013											
Russia			actiCHamp- Russia_ 2013							nvx136- Russia_ 2013		
Switzerland					EGI- Zurich_2017				NihonKohden - Bern_1980			
USA				DEDAAS- NewYork_ 1970s								

Appendix E. nBIC/nEBIC values for all possible models

**Table E1**  
nBIC/nEBIC values for all possible modes.

Metric Model component type	Model	nBIC values of $y_{i,c,c'}^\lambda(\omega)$			nEBIC values $y_{i,c,c'}^\beta(\omega)$		
		"Batch" definition			"Batch" definition		
		country	device	study	country	device	study
I: Fixed effects	0-A	1.000			0.995		
	1-A	0.995			0.715		
	2-A	0.321			1.000		
	3-A	0.164			0.711		
II: Constant random effects	4-A	0.156	0.157	0.154	0.326	0.349	0.285
	5-A	0.164	0.164	0.164	0.710	0.710	0.710
	6-A	0.156	0.157	0.155	0.327	0.350	0.287
III: Functional random effects	7-A	0.117	0.119	0.111	0.347	0.372	0.315
	8-A	0.154	0.154	0.153	0.250	0.250	0.211
	9-A	0.121	0.125	0.127	0.510	0.595	0.631
IV: Heteroscedasticity	3-C	0.064	0.064	0.064	0.562	0.562	0.562
	8-B	0.112	0.113	0.104	0.107	0.096	0.041
	8-C	0.019	0.022	0.014	0.151	0.154	0.107
	8-D	0.014	0.018	0.008	0.060	0.072	0.008
	8-E	0.006	0.011	0.000	0.044	0.050	0.000

For the fixed effect, the nBIC/nEBIC values for three batch definition are the same.

References

Ahn, H., Prichep, L., John, E., Baird, H., Trepetin, M., Kaye, H., 1980. Developmental equations reflect brain dysfunctions. *Science* 210, 1259–1262. doi:10.1126/science.7434027.

Akaike, H., 1973. Maximum likelihood identification of Gaussian autoregressive moving average models. *Biometrika* 60, 255–265. doi:10.1093/biomet/60.2.255.

Arsigny, V., Fillard, P., Pennec, X., Ayache, N., 2005. Fast and simple calculus on tensors in the log-euclidean framework. In: Duncan, J.S., Gerig, G. (Eds.), *Medical Image Computing and Computer-Assisted Intervention – MICCAI 2005. Lecture Notes in Computer Science*. Springer Berlin Heidelberg, Berlin, Heidelberg, pp. 115–122. doi:10.1007/11566465\_15.

Babayán, A., Erbey, M., Kumral, D., Reinelt, J.D., Reiter, A.M.F., Röbbig, J., Schaare, Lina, H., Uhligh, M., Anwander, A., Bazin, P.L., Horstmann, A., Lampe, L., Nikulin, V., Okon-Singer, H., Preusser, S., Pampel, A., Rohr, C.S., Sacher, J., Thöne-Otto, A., Trapp, S., Nierhaus, T., Altmann, D., Arelin, K., Blöchl, M., Bongartz, E., Breig, P., Cesnaite, E., Chen, S., Cozatl, R., Czerwonatis, S., Dambrauskaite, G., Dreyer, M., Enders, J., Engelhardt, M., Fischer, M.M., Forschack, N., Golchert, J., Golz, L., Guran, C.A., Hedrich, S., Hentschel, N., Hoffmann, D.I., Huntenburg, J.M., Jost, R., Kosatschek, A., Kunzendorf, S., Lammers, H., Lauckner, M.E., Mahjoory, K., Kanaan, A.S., Mendes, N., Menger, R., Morino, E., Nätke, K., Neubauer, J., Noyan, H., Oligschläger, S., Panczyszyn-Trzewik, P., Poehlchen, D., Putzke, N., Roski, S., Schaller, M.C., Schieferbein, A., Schlaak, B., Schmidt, R., Gorgolewski, K.J., Schmidt, H.M., Schrimpf, A., Stasch, S., Voss, M., Wiedemann, A., Margulies, D.S., Gaebler, M., Villringer, A., 2019. Data descriptor: a mind-brain-body dataset of MRI, EEG, cognition, emotion, and peripheral physiology in young and old adults. *Sci. Data* 6, 1–21. doi:10.1038/sdata.2018.308.

Barachant, A., Bonnet, S., Congedo, M., Jutten, C., 2013. Classification of covariance matrices using a Riemannian-based kernel for BCI applications. *Neurocomputing* 112, 172–178. doi:10.1016/j.neucom.2012.12.039, advances in artificial neural networks, machine learning, and computational intelligence.

Barachant, A., Bonnet, S., Congedo, M., Jutten, C., 2012. Multiclass brain-computer interface classification by riemannian geometry. *IEEE Trans. Biomed. Eng.* 59, 920–928. doi:10.1109/TBME.2011.2172210.

Benjamini, Y., Hochberg, Y., 1995. Controlling the false discovery rate: a practical and powerful approach to multiple testing. *J. R. Stat. Soc. Ser. B (Methodol.)* 57, 289–300.

Benjamini, Y., Yekutieli, D., 2001. The control of the false discovery rate in multiple testing under dependency. *Ann. Statist.* 29. doi:10.1214/aos/1013699998.

Bhatia, R., 2013. The riemannian mean of positive matrices. In: Nielsen, F., Bhatia, R. (Eds.), *Matrix Information Geometry*. Springer Berlin Heidelberg, Berlin, Heidelberg, pp. 35–51. doi:10.1007/978-3-642-30232-9\_2.

Bethlehem, R. a. I., Seidlitz, J., White, S.R., Vogel, J.W., Anderson, K.M., Adamson, C., Adler, S., Alexopoulos, G.S., Anagnostou, E., Areces-Gonzalez, A., Astle, D.E., Auyeung, B., Ayub, M., Bae, J., Ball, G., Baron-Cohen, S., Beare, R., Bedford, S.A., Benegal, V., Beyer, F., Blangero, J., Blesa Cábez, M., Boardman, J.P., Borzage, M., Bosch-Bayard, J.F., Bourke, N., Calhoun, V.D., Chakravarty, M.M., Chen, C., Chertavian, C., Chetelat, G., Chong, Y.S., Cole, J.H., Corvin, A., Costantino, M., Courchesne, E., Crivello, F., Cropley, V.L., Crosbie, J., Crossley, N., Delarue, M., Delorme, R., Desrivieres, S., Devenyi, G.A., Di Biase, M.A., Dolan, R., Donald, K.A., Donohoe, G., Dunclop, K., Edwards, A.D., Elison, J.T., Ellis, C.T., Elman, J.A., Eyler, L., Fair, D.A., Feczko, E., Fletcher, P.C., Fonagy, P., Franz, C.E., Galan-Garcia, L., Gholipour, A., Giedd, J., Gilmore, J.H., Glahn, D.C., Goodyer, I.M., Grant, P.E., Groenewold, N.A., Gunning, F.M., Gur, R.E., Gur, R.C., Hammill, C.F., Hansson, O., Hedden, T., Heinz, A., Henson, R.N., Heuer, K., Hoare, J., Holla, B., Holmes, A.J., Holt, R., Huang, H., Im, K., Ipser, J., Jack, C.R., Jackowski, A.P., Jia, T., Johnson, K.A., Jones, P.B., Jones, D.T., Kahn, R.S., Karlsson, H., Karlsson, L., Kawashima, R., Kelley, E.A., Kern, S., Kim, K.W., Kitzbichler, M.G., Kremen, W.S., Lalonde, F., Landeau, B., Lee, S., Lerch, J., Lewis, J.D., Li, J., Liao, W., Liston, C., Lombardo, M.V., Lv, J., Lynch, C., Mallard, T.T., Marcelis, M., Markello, R.D., Mathias, S.R., Mazoyer, B., McGuire, P., Meaney, M.J., Mechelli, A., Medic, N., Mistic, B., Morgan, S.E., Mothersill, D., Nigg, J., Ong, M.Q.W., Ortinau, C., Ossenkoppele, R., Ouyang, M., Palaniyappan, L., Paly, L., Pan, P.M., Pantelis, C., Park, M.M., Paus, T., Pausova, Z., Paz-Linares, D., Pichet Binette, A., Pierce, K., Qian, X., Qiu, J., Qiu, A., Raznaahan, A., Rittman, T., Rodrigue, A., Rollins, C.K., Romero-Garcia, R., Roman, L., Rosenberg, M.D., Rowitch, D.H., Salum, G.A., Satterthwaite, T.D., Schaare, H.L., Schachar, R.J., Schultz, A.P., Schumann, G., Schöll, M., Sharp, D., Shinohara, R.T., Skoog, I., Smyser, C.D., Sperling, R.A., Stein, D.J., Stolicyn, A., Suckling, J., Sullivan, G., Taki, Y., Thyreau, B., Toro, R., Traut, N., Tsvetanov, K.A., Turk-Browne, N.B., Tuulari, J.J., Tzourio, C., Vachon-Presseau, É., Valdes-Sosa, M.J., Valdes-Sosa, P.A., Valk, S.L., van Amelsvoort, T., Vandekar, S.N., Vasung, L., Victoria, L.W., Villeneuve, S., Villringer, A., Vértes, P.E., Wagstyl, K., Wang, Y.S., Warfield, S.K., Warrier, V., Westman, E., Westwater, M.L., Whalley, H.C., Witte, A.V., Yang, N., Yeo, B., Yun, H., Zalesky, A., Zar, H.J., Zettergren, A., Zhou, J.H., Ziauddeen, H., Zugman, A., Zuo, X.N., Bullmore, E.T., Alexander-Bloch, A.F., 2022. Brain charts for the human lifespan. *Nature* 1–11. doi:10.1038/s41586-022-04554-y.

Bhatia, R., 2007. *Positive Definite matrices, Princeton Series in Applied Mathematics*. Princeton University Press, Princeton, N.J.

Bhatia, R., Holbrook, J., 2006. Riemannian geometry and matrix geometric means. *Linear Algebr. Appl.* 413, 594–618. doi:10.1016/j.laa.2005.08.025.

Billings, S.A., Tsang, K.M., 1989a. Spectral analysis for non-linear systems, Part I: parametric non-linear spectral analysis. *Mech. Syst. Signal Process.* 3, 319–339. doi:10.1016/0888-3270(89)90041-1.

- Billings, S.A., Tsang, K.M., 1989b. Spectral analysis for non-linear systems, Part II: interpretation of non-linear frequency response functions. *Mech. Syst. Signal Process.* 3, 341–359. doi:10.1016/0888-3270(89)90042-3.
- Bini, D.A., Iannazzo, B., 2013. Computing the Karcher mean of symmetric positive definite matrices. *Linear Algebr. Appl.* 438, 1700–1710. doi:10.1016/j.laa.2011.08.052.
- Biscay Lirio, R., Valdés Sosa, P.A., Pascual Marqui, R.D., Jiménez-Sobrino, J.C., Alvarez Amador, A., Galán García, L., 1989. Multivariate box-cox transformations with applications to neurometric data. *Comput. Biol. Med.* 19, 263–267. doi:10.1016/0010-4825(89)90013-9.
- Bosch-Bayard, J., Galan, L., Aubert Vazquez, E., Virues Alba, T., Valdes-Sosa, P.A., 2020. Resting State Healthy EEG: the first wave of the cuban normative database. *Front. Neurosci.* 14. doi:10.3389/fnins.2020.555119.
- Bosch-Bayard, J., Galán-García, L., Fernandez, T., Lirio, R.B., Bringas-Vega, M.L., Roca-Stappung, M., Ricardo-Garcell, J., Harmony, T., Valdes-Sosa, P.A., 2018. Stable sparse classifiers identify qEEG signatures that predict learning disabilities (NOS) severity. *Front. Neurosci.* 11, 749. doi:10.3389/fnins.2017.00749.
- Bosch-Bayard, J., Razaq, F.A., Lopez-Naranjo, C., Wang, Y., Li, M., Galan-Garcia, L., Calzada-Reyes, A., Virues-Alba, T., Rabinowitz, A.G., Suarez-Murias, C., Guo, Y., Sanchez-Castillo, M., Rogers, K., Gallagher, A., Prichep, L., Anderson, S.G., Michel, C.M., Evans, A.C., Bringas-Vega, M.L., Galler, J.R., Valdes-Sosa, P.A., 2022. Early protein energy malnutrition impacts life-long developmental trajectories of the sources of EEG rhythmic activity. *NeuroImage* 254, 119144. doi:10.1016/j.neuroimage.2022.119144.
- Bosch-Bayard, J., Valdés-Sosa, P., Virues-Alba, T., Aubert-Vázquez, E., John, E.R., Harmony, T., Riera-Díaz, J., Trujillo-Barreto, N., 2001. 3D statistical parametric mapping of EEG source spectra by means of variable resolution electromagnetic tomography (VARETA). *Clin. Electroencephalogr.* 32, 47–61. doi:10.1177/155005940103200203.
- Braman, K., 2010. Third-order tensors as linear operators on a space of matrices. *Linear Algebr. Appl.* 433, 1241–1253. doi:10.1016/j.laa.2010.05.025.
- Brillinger, D.R., 1981. *Time Series: Data Analysis and Theory*. SIAM.
- Bringas Vega, M.L., Guo, Y., Tang, Q., Razaq, F.A., Calzada Reyes, A., Ren, P., Paz Linares, D., Galan Garcia, L., Rabinowitz, A.G., Galler, J.R., Bosch-Bayard, J., Valdes Sosa, P.A., 2019. An age-adjusted EEG source classifier accurately detects school-aged barbadian children that had protein energy malnutrition in the first year of life. *Front. Neurosci.* 13, 1222. doi:10.3389/fnins.2019.01222.
- Chen, J., Chen, Z., 2012. Extended BIC for small-n-large-P sparse GLM. *Stat. Sin.* 22. doi:10.5705/ss.2010.216.
- Chen, J., Chen, Z., 2008. Extended Bayesian information criteria for model selection with large model spaces. *Biometrika* 95, 759–771. doi:10.1093/biomet/asn034.
- Chen, L.H., Cheng, M.Y., Peng, L., 2009. Conditional variance estimation in heteroscedastic regression models. *J. Stat. Plan Inference* 139, 236–245. doi:10.1016/j.jspi.2008.04.020.
- Congedo, M., Barachant, A., Bhatia, R., 2017. Riemannian geometry for EEG-based brain-computer interfaces: a primer and a review. *Brain Comput. Interfaces* 4, 155–174. doi:10.1080/2326263X.2017.1297192.
- Craven, P., Wahba, G., 1978. Smoothing noisy data with spline functions. *Numer. Math.* 31, 377–403. doi:10.1007/BF01404567.
- Duan, W., Chen, X., Wang, Y.-J., Zhao, W., Yuan, H., Lei, X., 2021. Reproducibility of power spectrum, functional connectivity and network construction in resting-state EEG. *Journal of Neuroscience Methods* 348, 108985. doi:10.1016/j.jneumeth.2020.108985.
- Engemann, D.A., Mellot, A., Höchenberger, R., Banville, H., Sabbagh, D., Gemein, L., Ball, T., Gramfort, A., 2021. A reusable benchmark of brain-age prediction from M/EEG resting-state signals (preprint). *Neuroscience* doi:10.1101/2021.12.14.472691.
- Fisher, R.A., 1922. On the interpretation of  $\chi^2$  from contingency tables, and the calculation of P. *J. R. Stat. Soc.* 85, 87. doi:10.2307/2340521.
- Fortin, J.P., Cullen, N., Sheline, Y.I., Taylor, W.D., Aselcioglu, I., Cook, P.A., Adams, P., Cooper, C., Fava, M., McGrath, P.J., McInnis, M., Phillips, M.L., Trivedi, M.H., Weissman, M.M., Shinohara, R.T., 2018. Harmonization of cortical thickness measurements across scanners and sites. *Neuroimage* 167, 104–120. doi:10.1016/j.neuroimage.2017.11.024.
- Galler, J.R., Bringas-Vega, M.L., Tang, Q., Rabinowitz, A.G., Musa, K.I., Chai, W.J., Omar, H., Abdul Rahman, M.R., Abd Hamid, A.I., Abdullah, J.M., Valdés-Sosa, P.A., 2021. Neurodevelopmental effects of childhood malnutrition: a neuroimaging perspective. *Neuroimage* 231, 117828. doi:10.1016/j.neuroimage.2021.117828.
- Galler, J.R., Ramsey, F., Solimano, G., Lowell, W.E., 1983a. The influence of early malnutrition on subsequent behavioral development: II. Classroom behavior. *J. Am. Acad. Child Psychiatry* 22, 16–22. doi:10.1097/00004583-198301000-00003.
- Galler, J.R., Ramsey, F., Solimano, G., Lowell, W.E., Mason, E., 1983b. The influence of early malnutrition on subsequent behavioral development: I. Degree of impairment in intellectual performance. *J. Am. Acad. Child Psychiatry* 22, 8–15. doi:10.1097/00004583-198301000-00002.
- Gazula, H., Kelly, R., Romero, J., Verner, E., Baker, B., Silva, R., Imtiaz, H., Saha, D., Raja, R., Turner, J., Sarwate, A., Plis, S., Calhoun, V., 2020. COINSTAC: collaborative Informatics and neuroimaging suite toolkit for anonymous computation. *JOSS* 5, 2166. doi:10.21105/joss.02166.
- Girard, A., 1989. A fast “monte-carlo cross-validation” procedure for large least squares problems with noisy data. *Numer. Math.* 56, 1–23. doi:10.1007/BF01395775.
- Gordon, E., Cooper, N., Rennie, C., Hermens, D., Williams, L.M., 2005. Integrative neuroscience: the role of a standardized database. *Clin. EEG Neurosci.* 36, 64–75. doi:10.1177/155005940503600205.
- Harmony, T., 1984. *Neurometric Assessment of Brain Dysfunction in Neurological Patients*. Lawrence Erlbaum Associates.
- Harmony, T., Alvarez, A., Pascual, R., Ramos, A., Marosi, E., Díaz De León, A.E., Valdés, P., Becker, J., 1988. EEG maturation on children with different economic and psychosocial characteristics. *Int. J. Neurosci.* 41, 103–113. doi:10.3109/00207458808985747.
- Hauberg, S., Lauze, F., Pedersen, K.S., 2013. Unscented kalman filtering on riemannian manifolds. *J. Math. Imaging Vis.* 46, 103–120. doi:10.1007/s10851-012-0372-9.
- Hernández, J.L., Valdés, P., Biscay, R., Virues, T., Szava, S., Bosch, J., Riquenes, A., Clark, I., 1994. A global scale factor in brain topography. *Int. J. Neurosci.* 76, 267–278. doi:10.3109/00207459408986009.
- Hernandez-Gonzalez, G., Bringas-Vega, M.L., Galán-García, L., Bosch-Bayard, J., Lorenzo-Ceballos, Y., Melie-García, L., Valdes-Urrutia, L., Cobas-Ruiz, M., Valdes-Sosa, P.A. Cuban Human Brain Mapping Project (CHBMP), 2011. Multimodal quantitative neuroimaging databases and methods: the cuban human brain mapping project. *Clin. EEG Neurosci.* 42, 149–159. doi:10.1177/155005941104200303.
- Paz-Linares, D., Gonzalez-Moreira, E., Martinez-Montes, E., Valdes-Hernandez, P.A., Bosch-Bayard, J., Bringas-Vega, M.L., Valdes-Sosa, P.A., 2018. Caulking the leakage effect in MEEG source connectivity analysis. arXiv preprint arXiv:1810.00786.
- Hu, S., Valdes-Sosa, P.A., Xi rhythms: decoding neural oscillations to create full-brain high-resolution spectra parametric mapping.
- Hu, S., Yao, D., Bringas-Vega, M.L., Qin, Y., Valdes-Sosa, P.A., 2019. The statistics of EEG unipolar references: derivations and properties. *Brain Topogr.* 32, 696–703. doi:10.1007/s10548-019-00706-y.
- Ivanov, R., Kazantsev, F., Zavarzin, E., Klimenko, A., Milakhina, N., Matushkin, Y.G., Savostyanov, A., Lashin, S., 2022. ICBrainDB: An Integrated Database for Finding Associations between Genetic Factors and EEG Markers of Depressive Disorders. *Journal of Personalized Medicine* 12. doi:10.3390/jpm12010053.
- John, E.R., Karmel, B.Z., Corning, W.C., Easton, P., Brown, D., Ahn, H., John, M., Harmony, T., Prichep, L., Toro, A., 1977. Neurometrics: Numerical taxonomy identifies different profiles of brain functions within groups of behaviorally similar people. *Science* 196, 1393–1410.
- John, E.R., Prichep, L.S., Fridman, J., Easton, P., 1988. Neurometrics: Computer-Assisted Differential Diagnosis of Brain Dysfunctions. *Science* 239, 162–169. doi:10.1126/science.3336779.
- Johnson, W.E., Li, C., Rabinovic, A., 2007. Adjusting batch effects in microarray expression data using empirical Bayes methods. *Biostatistics* 8, 118–127. doi:10.1093/biostatistics/kxj037.
- Karahan, E., Rojas-Lopez, P.A., Bringas-Vega, M.L., Valdes-Hernandez, P.A., Valdes-Sosa, P.A., 2015. Tensor Analysis and Fusion of Multimodal Brain Images. *Proceedings of the IEEE* 103, 1531–1559. doi:10.1109/JPROC.2015.2455028.
- Karcher, H., 1977. Riemannian center of mass and mollifier smoothing. *Commun. Pure Appl. Math.* 30, 509–541.
- Kilmer, M.E., Braman, K., Hao, N., Hoover, R.C., 2013. Third-order tensors as operators on matrices: a theoretical and computational framework with applications in imaging. *SIAM J. Matrix Anal. Appl.* 34, 148–172. doi:10.1137/110837711.
- Ko, J., Park, U., Kim, D., Kang, S.W., 2021. Quantitative electroencephalogram standardization: a sex- and age-differentiated normative database. *Front. Neurosci.* 15, 766781. doi:10.3389/fnins.2021.766781.
- Koenig, T., Prichep, L., Lehmann, D., Sosa, P.V., Braeker, E., Kleinlogel, H., Isenhardt, R., John, E.R., 2002. Millisecond by millisecond, year by year: normative EEG microstates and developmental stages. *Neuroimage* 16, 41–48. doi:10.1006/nimg.2002.1070.
- Langer, N., von Bastian, C.C., Wirz, H., Oberauer, K., Jäncke, L., 2013. The effects of working memory training on functional brain network efficiency. *Cortex* 49, 2424–2438. doi:10.1016/j.cortex.2013.01.008.
- Leonard, T., Hsu, J.S., 1992. Bayesian inference for a covariance matrix. *Ann. Stat.* 20, 1669–1696.
- Leonard, T., Hsu, J.S.J., 2001. *Bayesian Methods: An Analysis For Statisticians and Interdisciplinary Researchers*. Cambridge University Press.
- Leroy, A.M., Rousseeuw, P.J., 1987. *Robust Regression and Outlier Detection*. Wiley Series in Probability and Mathematical Statistics.
- Li, F., Liu, T., Wang, F., Li, H., Gong, D., Zhang, R., Jiang, Y., Tian, Y., Guo, D., Yao, D., Xu, P., 2015. Relationships between the resting-state network and the P3: evidence from a scalp EEG study. *Sci. Rep.* 5, 15129. doi:10.1038/srep15129.
- Lin, X., Zhang, D., 1999. Inference in generalized additive mixed models by using smoothing splines. *J. R. Stat. Soc. B* 61, 381–400. doi:10.1111/1467-9868.00183.
- Lorensen, T.D., Dickson, P., 2003. Quantitative EEG normative databases: a comparative investigation. *J. Neurother.* 7, 53–68. doi:10.1300/J184v07n03\_03.
- Lund, K., 2020. The tensor t-function: a definition for functions of third-order tensors. *Numer. Linear Algebr. Appl.* 27. doi:10.1002/nla.2288.
- Makeig, S., Debener, S., Onton, J., Delorme, A., 2004. Mining event-related brain dynamics. *Trends Cogn. Sci.* 8, 204–210. doi:10.1016/j.tics.2004.03.008.
- Manton, J.H., 2004. A globally convergent numerical algorithm for computing the centre of mass on compact Lie groups. In: *Proceedings of the ICARCV 2004 8th Control, Automation, Robotics and Vision Conference, 2004*. Presented at the 2004 8th International Conference on Control, Automation, Robotics and Vision (ICARCV). IEEE, Kunming, China, pp. 2211–2216. doi:10.1109/ICARCV.2004.1469774.
- Martínez-Montes, E., Valdés-Sosa, P.A., Miwakeichi, F., Goldman, R.I., Cohen, M.S., 2004. Concurrent EEG/fMRI analysis by multiway partial least squares. *Neuroimage* 22, 1023–1034. doi:10.1016/j.neuroimage.2004.03.038.
- Matoušek, M., Petersén, I., 1973. Automatic evaluation of EEG background activity by means of age-dependent EEG quotients. *Electroencephalography and Clinical Neurophysiology* 35, 603–612. doi:10.1016/0013-4694(73)90213-7.
- McClish, D.K., 1989. Analyzing a Portion of the ROC Curve. *Med. Decis. Mak.* 9, 190–195. doi:10.1177/0272989X8900900307.
- Miwakeichi, F., Martínez-Montes, E., Valdés-Sosa, P.A., Nishiyama, N., Mizuhara, H., Yamaguchi, Y., 2004. Decomposing EEG data into space-time-frequency components using parallel factor analysis. *Neuroimage* 22, 1035–1045. doi:10.1016/j.neuroimage.2004.03.039.

- Moakher, M., 2005. A differential geometric approach to the geometric mean of symmetric positive-definite matrices. *SIAM J. Matrix Anal. Appl.* 26, 735–747. doi:10.1137/S0895479803436937.
- Møller, J., 1986. Bartlett adjustments for structured covariances. *Scandinavian journal of statistics* 1–15.
- Nadaraya, E.A., 1964. On estimating regression. *Theory Probab. Appl.* 9, 141–142. doi:10.1137/1109020.
- Ng, B., Varoquaux, G., Poline, J.B., Greicius, M., Thirion, B., 2016a. Transport on riemannian manifold for connectivity-based brain decoding. *IEEE Trans. Med. Imaging* 35, 208–216. doi:10.1109/TMI.2015.2463723.
- Ng, B., Varoquaux, G., Poline, J.B., Greicius, M., Thirion, B., 2016b. Transport on riemannian manifold for connectivity-based brain decoding. *IEEE Trans. Med. Imaging* 35, 208–216. doi:10.1109/TMI.2015.2463723.
- Olive, D.J., 2004. A resistant estimator of multivariate location and dispersion. *Comput. Stat. Data Anal.* 46, 93–102. doi:10.1016/S0167-9473(03)00119-1.
- Pascual-marqui, R.D., Valdes-sosa, P.A., Alvarez-amador, A., 1988. A parametric model for multichannel EEG spectra. *Int. J. Neurosci.* 40, 89–99.
- Pavlov, Y.G., Adamian, N., Appelhoff, S., Arvaneh, M., Benwell, C.S.Y., Beste, C., Bland, A.R., Bradford, D.E., Bublitzky, F., Busch, N.A., Clayson, P.E., Cruse, D., Czeszumski, A., Dreber, A., Dumas, G., Ehinger, B., Ganis, G., He, X., Hinojosa, J.A., Huber-Huber, C., Inzlicht, M., Jack, B.N., Johannesson, M., Jones, R., Kalenkovich, E., Kaltwasser, L., Karimi-Rouzabani, H., Keil, A., König, P., Kouara, L., Kulke, L., Ladouceur, C.D., Langer, N., Liesefeld, H.R., Luque, D., MacNamara, A., Mudrik, L., Muthuraman, M., Neal, L.B., Nilsson, G., Niso, G., Ocklenburg, S., Oostenveld, R., Pernet, C.R., Pourtois, G., Ruggioni, M., Sass, S.M., Schaefer, A., Senderecka, M., Snyder, J.S., Tamnes, C., Tognoli, E., van Vugt, M.K., Verona, E., Vloeberghs, R., Welke, D., Wessel, J.R., Zakharov, I., Mushtaq, F., 2021. #EEG-ManyLabs: investigating the replicability of influential EEG experiments. *Cortex* doi:10.1016/j.cortex.2021.03.013, S0010945221001106.
- Penneec, X., 1999. Probabilities and statistics on Riemannian manifolds: Basic tools for geometric measurements. *NSIP, Citeseer*, pp. 194–198.
- Penneec, X., Fillard, P., Ayache, N., 2006. A riemannian framework for tensor computing. *Int. J. Comput. Vision.* 66, 41–66. doi:10.1007/s11263-005-3222-z.
- Pomponio, R., Erus, G., Habes, M., Doshi, J., Srinivasan, D., Mamourian, E., Bashyam, V., Nasrallah, I.M., Satterthwaite, T.D., Fan, Y., Launer, L.J., Masters, C.L., Maruff, P., Zhuo, C., Völzke, H., Johnson, S.C., Fripp, J., Koutsouleris, N., Wolf, D.H., Gur, Raquel, Gur, Ruben, Morris, J., Albert, M.S., Grabe, H.J., Resnick, S.M., Bryan, R.N., Walk, D.A., Shinohara, R.T., Shou, H., Davatzikos, C., 2020. Harmonization of large MRI datasets for the analysis of brain imaging patterns throughout the lifespan. *Neuroimage* 208, 116450. doi:10.1016/j.neuroimage.2019.116450.
- Rigby, R.A., Stasinopoulos, D.M., 2005. Generalized additive models for location, scale and shape. *J. R. Stat. Soc. Ser. C (Appl. Stat.)* 54, 507–554. doi:10.1111/j.1467-9876.2005.00510.x.
- Rousseeuw, P.J., Driessens, K.V., 1998. A fast algorithm for the minimum covariance determinant estimator. *Technometrics* 41, 212–223.
- Rutherford, S., Kia, S.M., Wolfers, T., Frazza, C., Zabihi, M., Dinga, R., Berthet, P., Worker, A., Verdi, S., Ruhe, H.G., Beckmann, C.F., Marquand, A.F., 2021. The Normative modeling framework for computational psychiatry (preprint). *Neuroscience* doi:10.1101/2021.08.08.455583.
- Sabbagh, D., Ablin, P., Varoquaux, G., Gramfort, A., Engemann, D.A., 2020. Predictive regression modeling with MEG/EEG: from source power to signals and cognitive states. *Neuroimage* 222, 116893. doi:10.1016/j.neuroimage.2020.116893.
- Schneider-Luftman, D., Walden, A.T., 2016. Partial coherence estimation via spectral matrix shrinkage under quadratic loss. *IEEE Trans. Signal Process.* 64, 5767–5777. doi:10.1109/TSP.2016.2582464.
- Schott, J.R., 2005. Testing for complete independence in high dimensions. *Biometrika* 92, 951–956. doi:10.1093/biomet/92.4.951.
- Schwarz, G., 1978. Estimating the Dimension of a Model. *Ann. Stat.* 6, 461–464.
- Simeon, G., Piella, G., Camara, O., Pareto, D., 2021. Riemannian geometry of functional connectivity matrices for multi-site attention-deficit/hyperactivity disorder data harmonization (preprint). *Neuroscience* doi:10.1101/2021.09.01.458579.
- Stone, M., 1974. Cross-validation and multinomial prediction. *Biometrika* 61, 509–515. doi:10.1093/biomet/61.3.509.
- Szava, S., Valdes, P., Biscay, R., Galan, L., Bosch, J., Clark, I., Jimenez, J.C., 1994. High resolution quantitative EEG analysis. *Brain Topogr.* 6, 211–219. doi:10.1007/BF01187711.
- Taboada-Crispi, A., Bringas-Vega, M.L., Bosch-Bayard, J., Galán-García, L., Bryce, C., Rabinowitz, A.G., Pritchep, L.S., Isenhardt, R., Calzada-Reyes, A., Virues-Alba, T., Guo, Y., Galler, J.R., Valdés-Sosa, P.A., 2018. Quantitative EEG tomography of early childhood malnutrition. *Front. Neurosci.* 12. doi:10.3389/fnins.2018.00595.
- Thatcher, R.W., Walker, R.A., Biver, C.J., North, D.N., Curtin, R., 2003. Quantitative EEG normative databases: validation and clinical correlation. *J. Neurother.* 7, 87–121. doi:10.1300/J184v07n03\_05.
- Thompson, P.M., Stein, J.L., Medland, S.E., Hibar, D.P., Vasquez, A.A., Renteria, M.E., Toro, R., Jahanshad, N., Schumann, G., Franke, B., Wright, M.J., Martin, N.G., Agartz, I., Alda, M., Alhusaini, S., Almsay, L., Almeida, J., Alpert, K., Andreassen, N.C., Andreassen, O.A., Apostolova, L.G., Appel, K., Armstrong, N.J., Aribisala, B., Bastin, M.E., Bauer, M., Bearden, C.E., Bergmann, Ø., Binder, E.B., Blangero, J., Bockholt, H.J., Bøen, E., Bois, C., Boomsma, D.I., Booth, T., Bowman, I.J., Bralten, J., Brouwer, R.M., Brunner, H.G., Brohawn, D.G., Buckner, R.L., Buitelaar, J., Bulayeva, K., Bustillo, J.R., Calhoun, V.D., Cannon, D.M., Cantor, R.M., Carless, M.A., Caseras, X., Cavalleri, G.L., Chakravarty, M.M., Chang, K.D., Ching, C.R.K., Christoforou, A., Cichon, S., Clark, V.P., Conrod, P., Coppola, G., Crespo-Facorro, B., Curran, J.E., Czisch, M., Deary, I.J., de Geus, E.J.C., den Braber, A., Delvecchio, G., Depondt, C., de Haan, L., de Zubicarary, G.I., Dima, D., Dimitrova, R., Djurovic, S., Dong, H., Donohoe, G., Duggirala, R., Dyer, T.D., Ehrlich, S., Ekman, C.J., Elvsåshagen, T., Emsell, L., Erk, S., Espeseth, T., Fagerness, J., Fears, S., Fedko, I., Fernández, G., Fisher, S.E., Foroud, T., Fox, P.T., Francks, C., Frangou, S., Frey, E.M., Frodl, T., Frouin, V., Garavan, H., Giddaluru, S., Glahn, D.C., Godlewska, B., Goldstein, R.Z., Gollub, R.L., Grabe, H.J., Grimm, O., Gruber, O., Guadalupe, T., Gur, R.E., Gur, R.C., Göring, H.H.H., Hagenaars, S., Hajek, T., Hall, G.B., Hall, J., Hardy, J., Hartman, C.A., Hass, J., Hatton, S.N., Haukvik, U.K., Hegenscheid, K., Heinz, A., Hickie, I.B., Ho, B.-C., Hoehn, D., Hoekstra, P.J., Hollinshead, M., Holmes, A.J., Homuth, G., Hoogman, M., Hong, L.E., Hosten, N., Hottenga, J.-J., Hulshoff Pol, H.E., Hwang, K.S., Jack, C.R., Jenkinson, M., Johnston, C., Jönsson, E.G., Kahn, R.S., Kasperaviciute, D., Kelly, S., Kim, S., Kochunov, P., Koenders, L., Krämer, B., Kwok, J.B.J., Lagopoulos, J., Laje, G., Landen, M., Landman, B.A., Lauriello, J., Lawrie, M., Lee, P.H., Le Hellard, S., Lemaître, H., Leonardo, C.D., Li, C., Liberg, B., Liewald, D.C., Liu, X., Lopez, L.M., Loth, E., Lourdasamy, A., Luciano, M., Macciardi, F., Machielsen, M.W.J., MacQueen, G.M., Malt, U.F., Mandl, R., Manoach, D.S., Martinot, J.-L., Matarin, M., Mather, K.A., Mattheisen, M., Mattingdal, M., Meyer-Lindenberg, A., McDonald, C., McIntosh, A.M., McMahon, F.J., McMahon, K.L., Meisenzahl, E., Melle, I., Milanese, Y., Mohnke, S., Montgomery, G.W., Morris, D.W., Moses, E.K., Mueller, B.A., Muñoz Maniega, S., Mühleisen, T.W., Müller-Myhsok, B., Mwangi, B., Nauck, M., Nho, K., Nichols, T.E., Nilsson, L.-G., Nugent, A.C., Nyberg, L., Olvera, R.L., Oosterlaan, J., Ophoff, R.A., Pandolfo, M., Papalamproulou-Tsirikidou, M., Pappmeyer, M., Paus, T., Pausova, S., Pearlson, G.D., Penninx, B.W., Peterson, C.P., Pfenning, A., Phillips, M., Pike, G.B., Poline, J.-B., Potkin, S.G., Pütz, B., Ramasamy, A., Rasmussen, J., Rietschel, M., Rijpkema, M., Risacher, S.L., Roffman, J.L., Roiz-Santiañez, R., Romanczuk-Seiferth, N., Rose, E.J., Royle, N.A., Rujescu, D., Ryten, M., Sachdev, P.S., Salami, A., Satterthwaite, T.D., Savitz, J., Saykin, A.J., Scanlon, C., Schmaal, L., Schnack, H.G., Schork, A.J., Schulz, S.C., Schür, R., Seidman, L., Shen, L., Shoemaker, J.M., Simmons, A., Sisodiya, S.M., Smith, C., Smoller, J.W., Soares, J.C., Sponheim, S.R., Sprooten, E., Starr, J.M., Steen, V.M., Strakowski, S., Strike, L., Sussmann, J., Sämann, P.G., Teumer, A., Toga, A.W., Tordesillas-Gutierrez, D., Trabzuni, D., Trost, S., Turner, J., Van den Heuvel, M., van der Wee, N.J., van Eijk, K., van Erp, T.G.M., van Haren, N.E.M., van 't Ent, D., van Tol, M.-J., Valdés Hernández, M.C., Veltman, D.J., Versace, A., Völzke, H., Walker, R., Walter, H., Wang, L., Wardlaw, J.M., Weale, M.E., Weiner, M.W., Wen, W., Westlye, L.T., Whalley, H.C., Whelan, C.D., White, T., Winkler, A.M., Wittfeld, K., Woldehariat, G., Wolf, C., Zilles, D., Zwiers, M.P., Thalamuthu, A., Schofield, P.R., Freimer, N.B., Lawrence, N.S., Drevets, W., the Alzheimer's Disease Neuroimaging Initiative, EPiGen Consortium, IMAGEN Consortium, Saguenay Youth Study (SYS) Group, 2014. The ENIGMA consortium: large-scale collaborative analyses of neuroimaging and genetic data. *Brain Imaging Behav.* 8, 153–182. doi:10.1007/s11682-013-9269-5.
- Tröndle, M., Popov, T., Dziemian, S., Langer, N., 2021. Decomposing the role of alpha oscillations during brain maturation.
- Turlach, B.A., Wand, M.P., 1996. Fast computation of auxiliary quantities in local polynomial regression. *J. Comput. Graph. Stat.* 5, 337–350.
- Tuzel, O., Porikli, F., Meer, P., 2008. Pedestrian detection via classification on riemannian manifolds. *IEEE Trans. Pattern Anal. Mach. Intell.* 30, 1713–1727. doi:10.1109/TPAMI.2008.75.
- Valdés, P., Bosch, J., Grave, R., Hernandez, J., Riera, J., Pascual, R., Biscay, R., 1992. Frequency domain models of the EEG. *Brain Topogr.* 4, 309–319.
- Valdés-Sosa, P.A., Evans, A.C., Valdés-Sosa, M., Mu-ming, P., 2021. A call for international research on COVID induced brain disorders. *Natl. Sci. Rev.* doi:10.1093/nsr/nwab190.
- Valdes-Sosa, P.A., Galan-Garcia, L., Bosch-Bayard, J., Bringas-Vega, M.L., Aubert-Vazquez, E., Rodriguez-Gil, I., Das, S., Madjar, C., Virues-Alba, T., Mohades, Z., MacIntyre, L.C., Rogers, C., Brown, S., Valdes-Urrutia, L., Evans, A.C., Valdes-Sosa, M.J., 2021. The cuban human brain mapping project, a young and middle age population-based EEG, MRI, and cognition dataset. *Sci. Data* 8, 45. doi:10.1038/s41597-021-00829-7.
- Van der Maaten, L., Hinton, G., 2008. Visualizing data using t-SNE. *J. Mach. Learn. Res.* 9, 2579–2605.
- Verdi, S., Marquand, A.F., Schott, J.M., Cole, J.H., 2021. Beyond the average patient: how neuroimaging models can address heterogeneity in dementia. *Brain* 165. doi:10.1093/brain/awab165, Awab.
- Walden, A.T., Schneider-Luftman, D., 2015. Random matrix derived shrinkage of spectral precision matrices. *IEEE Trans. Signal Process.* 63, 4689–4699.
- Wand, M.P., 1994. Fast computation of multivariate kernel estimators. *Null* 3, 433–445. doi:10.1080/10618600.1994.10474656.
- Yger, F., Berar, M., Lotte, F., 2017. Riemannian approaches in brain-computer interfaces: a review. *IEEE Trans. Neural Syst. Rehabil. Eng.* 25, 1753–1762. doi:10.1109/TNSRE.2016.2627016.